

High rate electrochemical dissolution of iron-based alloys in NaCl and NaNO₃ electrolytes

Von der Fakultät Chemie der Universität Stuttgart
zur Erlangung der Würde eines Doktors der
Naturwissenschaften (Dr. rer. nat.) genehmigte Abhandlung

Vorgelegt von

Thomas Wagner (geb. Haisch)

aus Waiblingen

Hauptberichter: Prof. Dr. Ir. E.J. Mittemeijer

Mitberichter: Prof. Dr. J.W. Schultze

Mitprüfer: Prof. Dr. F. Aldinger

Tag der Einreichung: 19.07.02

Tag der mündlichen Prüfung: 22.10.02

Institut für Metallforschung der Universität Stuttgart
Max-Planck-Institut für Metallforschung Stuttgart

2002

Table of contents

1 Introduction	1
1.1 Actual knowledge of high rate electrochemical metal dissolution	2
1.2 Aim of this work	3
1.3 Industrial applications of Electrochemical Machining	4
2 Fluid dynamics	7
2.1 The viscosity of the electrolyte	8
2.2 The Navier-Stokes equations	9
2.3 Simulation of electrolyte flow; geometrical problems	10
2.4 Comparison of 2D-simulation with experimental results	12
3 Influences of material inhomogeneities in 100Cr6 steel on the electrochemical metal dissolution process	14
3.1 Introduction	15
3.2 Experimental	15
3.3 Results and discussion	17
3.4 Conclusions	26
4 Electrochemical Machining of the steel 100Cr6 in aqueous NaCl and NaNO₃ solutions: Microstructure of surface films formed by carbides	28
4.1 Introduction	29
4.2 Experimental	30
4.3 Results	32
4.4 Discussion	39
4.5 Conclusions	41
5 On the influence of microstructure and carbide content of steels on the electrochemical dissolution process in aqueous NaCl-electrolytes	43
5.1 Introduction	44
5.2 Experimental procedure	45
5.3 Results and discussion	49
5.4 Steel substrate dissolution mechanisms	68
5.5 Conclusions	74
5.6 Appendix	76

6 High rate anodic dissolution of steel 100Cr6 in aqueous NaNO₃ solution	77
6.1 Introduction	78
6.2 Experimental	78
6.3 Electrode reactions	80
6.4 Results and interpretation	83
6.5 General discussion	96
6.6 Conclusions	101
7 Kurzfassung der Dissertation in deutscher Sprache	103
References	119
Curriculum vitae	123

Chapter

1

Introduction

1.1 Actual knowledge of high rate electrochemical metal dissolution

All traditional methods of mechanical workpiece machining, like hole drilling or mechanical polishing are usually carried out according to the typical pattern that a tool of very hard material (i.e. diamond) is used for scraping out the softer material of the workpiece (typically metal alloys or steel substrates). An important disadvantage of these mechanical machining methods is the continuous wear of the tool leading to its complete destruction upon intensive usage. As the physical properties of new, technologically important materials have reached higher degrees of hardness and heat resistance, the demands placed on the properties of the tool material have become nearly impossible to fulfil. As a consequence, other improved methods for fast, non-mechanical metal removal had to be investigated and developed during the last decades [1-3].

One group of the new developed, unconventional machining processes is based on the atom-by-atom removal of the metal substrate by controlled anodic dissolution processes. Typical examples for these electrochemical machining processes are electropolishing as a substitute for mechanical polishing [4-9], electrochemical jet machining for precise microstructuring [10-12], electrochemical hole drilling with no mechanical contact of the tool and the workpiece (also known as shaped tube electrolytic machining (STEM) [13-15]) and the high rate Electrochemical Machining (ECM) with (and without) mask techniques [16,17]. The goal of using mask techniques is very similar to electrochemical jet machining: with the help of a well defined, electrochemically inert mask (i.e. a photoresist) on the substrate (the workpiece), the creation of „negative-structures” on the surface of metals and alloys becomes possible without any dependence on the hardness of the substrate.

Because of its very important role in the metal-manufacturing industry, many studies on ECM (with flow channel cells or rotating cylinder setups) have been carried out and presented in literature with the goal of understanding

- the basic electrochemical reactions occurring at the anode and the cathode in dependence on the properties of the electrolyte [18-22],
- the influence of the electrolyte composition on the polarization behaviour of the substrate [23-27],

- the effect of varying electrolyte flow rates and concentrations on the surface morphology resulting from high rate anodic dissolution [28-30],
- and the role of material-dependant anodic surface films in ECM, which have been observed for various electrolyte/anode material combinations [31-33].

In these investigations, pure metals like aluminium, chromium, copper, iron, nickel and titanium have been chosen as anode materials in combination with adjusted electrolyte systems. To keep the Ohmic resistance of the electrolyte in the ECM-cell as small as possible, very small electrode distances ($\leq 100 \mu\text{m}$) have been used and details concerning the cell and gap geometry have been published by many workers [34,35]. In these studies, the well known problem of sparking during the ECM process at high current densities has been reported frequently [36].

According to Faraday's law, the metal removal rate of the metal substrate used for ECM depends on the dissolution valence of the element [16,37]. In order to calculate the theoretical removal rate of a pure metal it is necessary to define the most likely dissolution valence, n . On the basis of a given definition for n , typical metal removal rates at various current densities, i , have been given in tables [38]. If a substrate with multiple phases and varying microstructure is used as anode material for the ECM process, the calculation of the theoretical removal rate becomes complex, because in many cases it is impossible to predict which phase of the substrate dissolves faster than the other. This is one important reason why model descriptions for the high rate anodic dissolution process of steels (as typical multiphase systems) are very rare.

1.2 Aim of this work

Against the background given in Section 1.1, this work deals with the high rate metal removal process of selected steel substrates of varying carbon content and microstructure. With the investigations presented in this work, the complex reaction mechanisms and principles of steels upon the high rate electrochemical dissolution in activating NaCl electrolytes (see chapters 3 and 5) and passivating NaNO_3 electrolytes (see chapter 6) should be revealed and the role of anodic surface films developing at the substrate surface should be included in schematic dissolution models (see chapters 4 and 5). For the development of the accurate dissolution

models, mask-less Electrochemical Machining (ECM) experiments with the flow channel cell at very high electrolyte flow rates (average flow velocities: up to 7 m/s) and current densities up to 70 A/cm^2 had to be carried out in combination with following ex situ surface analysis. With the help of these experiments a satisfactory dissolution model for heterogeneous steel substrates should be developed, with special respect to the influence of local turbulences in the flowing electrolyte (see chapter 3). To specify and characterize the electrochemical behaviour of the examined electrolyte / substrate combination, polarization measurements with the rotating cylinder electrode (RCE) had to be carried out. With a view to the measured polarization curves, one should be able to understand the dependence of the electrode processes occurring at the anode on current density and hydrodynamic conditions (see chapters 4 and 5). For completion, the processes of anodic passive film growth and cathodic film reduction on steel substrates in NaNO_3 electrolyte (see chapter 6) should elucidate the role of iron oxides in surface film development upon ECM.

1.3 Industrial applications of Electrochemical Machining

As already mentioned, the high rate anodic metal dissolution plays an important role in diverse industrial metal-manufacturing applications. To get a brief overview on the basic working principles of typical anodic metal dissolution processes in industry, three common techniques will be presented here:

- a) the high speed metal dissolution process with the aid of a nozzle-shaped cathode (Shaped Tube Electrolytic Machining, STEM)
- b) the electrochemical jet machining process and
- c) the through-mask Electrochemical Micromachining process (EMM) with the help of photoresist masks.

The typical principle of the STEM process is illustrated in Fig. 1.1. The ECM-electrolyte (usually an aqueous solution of NaCl , NaNO_3 , NaClO_3 or NaOH) is pumped through a well defined metal tube (the cathode) with a diameter of 0.1 - 1 mm. The lateral area of the cathode is covered completely with an insulator (e. g. epoxy or polyurethane) to avoid stray currents. After applying a very high cell voltage of 20 - 100V the cathode is moved with the open side of the tube towards the

workpiece (the anode). If the metal removal rate of the workpiece (typically a steel substrate) is well known, a constant cathode feed rate according to the speed of metal removal can be selected. The anodic reaction products (within the electrolyte solution or as solid particles) are carried away by the turbulent electrolyte flow. With this technologically important process the fabrication of „microhole” structures of very precise geometry becomes possible without any mechanical influence on the workpiece [13].

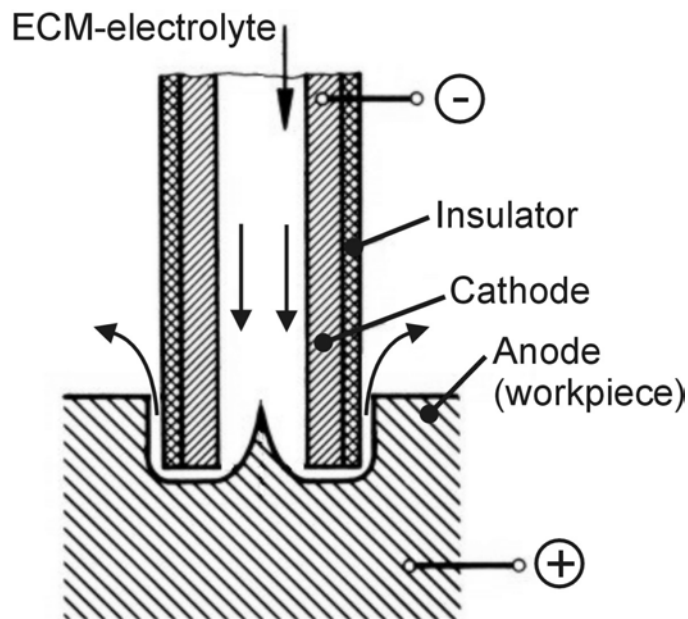


Fig. 1.1: Basic working principle of the Shaped Tube Electrolytic Machining (STEM) process. The black arrows indicate the main electrolyte flow direction.

The electrochemical jet machining process is very similar to STEM. As shown in Fig. 1.2, a tube cathode is used and the electrolyte is pumped through it (see also the working principle of STEM presented in Fig. 1.1). In contrast to STEM the cathode is not moved towards the workpiece; usually its position is fixed.

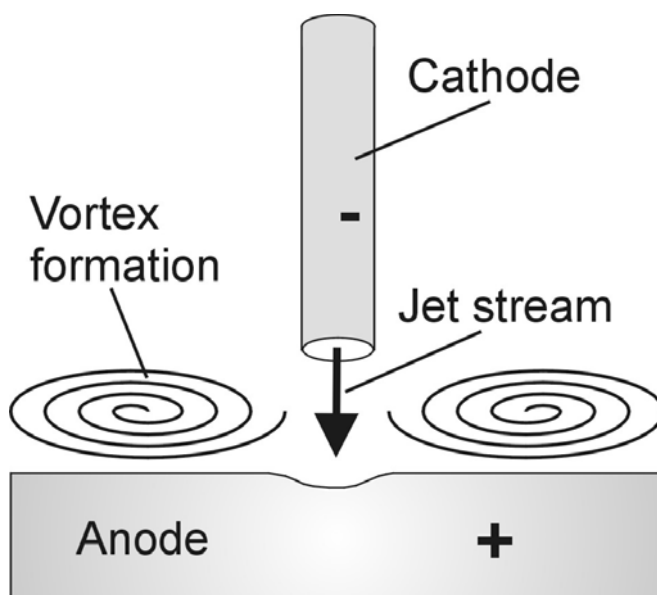


Fig. 1.2: Schematic representation of the electrochemical jet machining process. The electrolyte jet stream bounces locally against the anode (workpiece). Vortex formations occur outside of the metal removal area.

The most important advantage of electrochemical jet machining is its extremely high degree of localization (note that metal removal occurs exclusively at regions on the anode where the electrolyte jet stream realizes direct electrical contact with the cathode).

Electrochemical Micromachining (EMM) in conjunction with a photoresist mask is of considerable interest in microelectronic fabrication. Through-mask EMM involves selective metal dissolution from unprotected areas of a photoresist-patterned workpiece. The typical two-electrode arrangement of the EMM process is illustrated in Fig. 1.3:

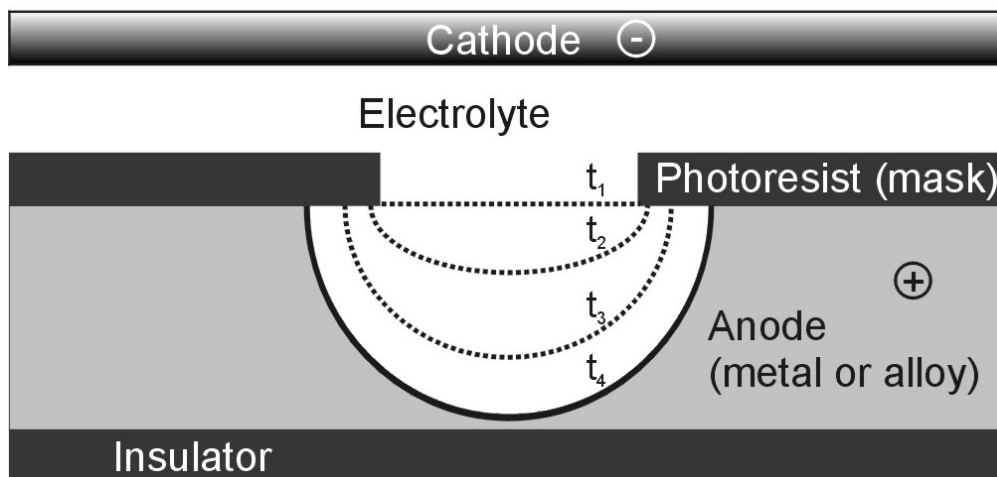


Fig. 1.3: Typical electrode arrangement in EMM at different reaction times t_x . The electrolyte fills the space between the cathode and the photoresist-patterned metal substrate.

Microstructuring of the metal in EMM is carried out by the selective anodic dissolution of unprotected (open) areas at the substrate surface (white gap in the photoresist layer in Fig. 1.3). Through-mask metal removal by simple electroless chemical etching is usually accompanied by undercutting of the photoresist [17]. In EMM, however, the metal-removal rate in the lateral direction can be significantly reduced through proper consideration of mass transport and current distribution [39]. In Fig. 1.3, the effect of undercutting is indicated with the profile of the substrate at different dissolution times ($t_1 = 0$ s). With the help of a suitable electrolyte / metal combination the negative undercutting effect may be further minimized and the geometry of the „negative-structure” developing during EMM becomes very accurate [40].

Chapter

2

Fluid dynamics

2.1 The viscosity of the electrolyte

Since all ECM-experiments are carried out exclusively with flowing aqueous electrolytes, it is important to get detailed knowledge about the hydrodynamic properties of the fluid.

A very important property which is frequently required for electrochemical calculations is the viscosity of the fluid, μ . For the determination of μ , a simple experimental setup can be used, which is based on two very long parallel plates with the distance h between them. One of the plates is at rest, the other moves with the constant velocity U . The experiment teaches that the fluid, which is located between the plates, adheres to both walls, so that its velocity is zero at the plate at rest and equal to U at the plate in motion. Furthermore, the velocity distribution in the fluid is linear, so that the fluid velocity is proportional to the distance, y , from the plate at rest [41]:

$$u(y) = \frac{y}{h} U \quad (2.1)$$

In order to support the motion of the fluid it is necessary to apply a tangential force to the moving plate. That force (taken per unit area of the plate) is proportional to the velocity U and inversely proportional to the distance h . The frictional force per unit area, τ (shearing stress), is proportional to U/h , which can be substituted by $du(y)/dy$. The proportionality factor between τ and $du(y)/dy$ is the viscosity of the electrolyte, μ :

$$\tau = \mu \frac{du(y)}{dy} \quad (2.2)$$

The law given by equation (2.2) is known as Newton's law of friction.

Usually, the density of the electrolyte is of interest as well for ECM investigations. Therefore, the ratio of the viscosity, μ , and the density of the fluid, ρ , is defined as the kinematic viscosity, ν :

$$\nu = \frac{\mu}{\rho} \quad (2.3)$$

Typical values of the kinematic viscosity, ν , at 20°C are $1.004 \times 10^{-6} \text{ m}^2/\text{s}$ for pure water and $32.43 \times 10^{-6} \text{ m}^2/\text{s}$ for oil (Shell) [41].

2.2 The Navier-Stokes equations

The flow of a viscous fluid like an ECM-electrolyte can be specified by the three orthogonal components (u, v, w) of its velocity U , the electrolyte pressure $p(x, y, z, t)$, and the density $\rho(x, y, z, t)$, where x, y, z are the usual orthogonal co-ordinates of position and t is the time. Five equations are available for the determination of u, v, w, p , and ρ . They are

- a) the three equations of motion for the conservation of momentum,
- b) the continuity equation for the conservation of mass, and
- c) the thermodynamic equation of state.

The equations of motion are obtained from Newton's second law [41]. In the application of this law to a fluid in motion, two types of forces must be considered: (a) body (e.g. gravitational) forces, which act throughout the mass of the body, and (b) pressure and friction forces, which act on its boundary. The equations of motion can then be expressed in the form:

$$\rho \frac{dU}{dt} = \mathbf{F} + \mathbf{P} \quad (2.4)$$

where \mathbf{F} is the gravitational force per unit and \mathbf{P} is the boundary force. As usual, \mathbf{F} and \mathbf{P} can be written in component form:

$$\mathbf{F} = iF_x + jF_y + kF_z \quad (2.5)$$

$$\mathbf{P} = iP_x + jP_y + kP_z \quad (2.6)$$

where i, j , and k are unit vectors along the x, y , and z axes. It should be noted that these are the only types of forces considered in this analysis. The thermodynamic equation of state can be written in the form:

$$F(\rho, p, T) = 0 \quad (2.7)$$

For the simple case of perfect gases, the usual equation of state is

$$\rho = \rho RT \quad (2.8)$$

where ρ is the gas density, R is the gas constant, and T the gas temperature. Since all ECM-experiments are carried out with liquid electrolytes (usually aqueous salt solutions), it is sufficient to write down the fundamental equations of motion for incompressible flow [41]:

$$\rho \left(\frac{\partial u}{\partial t} + u \frac{\partial u}{\partial x} + v \frac{\partial u}{\partial y} + w \frac{\partial u}{\partial z} \right) = F_x - \frac{\partial p}{\partial x} + \mu \left(\frac{\partial^2 u}{\partial x^2} + \frac{\partial^2 u}{\partial y^2} + \frac{\partial^2 u}{\partial z^2} \right) \quad (2.9)$$

$$\rho \left(\frac{\partial v}{\partial t} + u \frac{\partial v}{\partial x} + v \frac{\partial v}{\partial y} + w \frac{\partial v}{\partial z} \right) = F_y - \frac{\partial p}{\partial y} + \mu \left(\frac{\partial^2 v}{\partial x^2} + \frac{\partial^2 v}{\partial y^2} + \frac{\partial^2 v}{\partial z^2} \right) \quad (2.10)$$

$$\rho \left(\frac{\partial w}{\partial t} + u \frac{\partial w}{\partial x} + v \frac{\partial w}{\partial y} + w \frac{\partial w}{\partial z} \right) = F_z - \frac{\partial p}{\partial z} + \mu \left(\frac{\partial^2 w}{\partial x^2} + \frac{\partial^2 w}{\partial y^2} + \frac{\partial^2 w}{\partial z^2} \right) \quad (2.11)$$

$$\frac{\partial u}{\partial x} + \frac{\partial v}{\partial y} + \frac{\partial w}{\partial z} = 0 \quad (2.12)$$

The first three equations are the Navier-Stokes equations and the fourth is the equation of continuity (μ is the absolute viscosity of the electrolyte). The numerical solution of these equations has been carried out within the simulation of flow profiles with the computer program Ansys Flotran (see Section 2.3).

2.3 Simulation of electrolyte flow; geometrical problems

For the „simple” case of a turbulent electrolyte flow through an ECM flow channel with perfect, smooth walls and an inserted flat metal substrate, which is subjected to the electrolyte, the velocity distribution of the turbulent flow can be described by an empirical expression of the form

$$\frac{u}{u_{\max}} = \left(\frac{y}{R} \right)^{\frac{1}{n}} \quad (2.13)$$

where u is the local flow velocity at the distance y from the wall, and R is the radius of the pipe (the flow channel). The exponent n varies with the Reynolds-number [41].

For the real case of Electrochemical Machining, local geometrical heterogeneities (microscopic troughs or hills) located at the substrate surface or at the walls of the flow channel have to be taken into account. It is expected, that at the location of a single heterogeneity a significant distortion of the electrolyte flow profile occurs. To demonstrate the distortion of the originally uniform turbulent flow profile by local heterogeneities in the flow channel (in this case: two artificial quadratic hindrances with dimensions 1mm x 1mm x 1mm) a 2D simulation with the program Ansys Flotran 5.6 has been carried out (see Fig. 2.1).

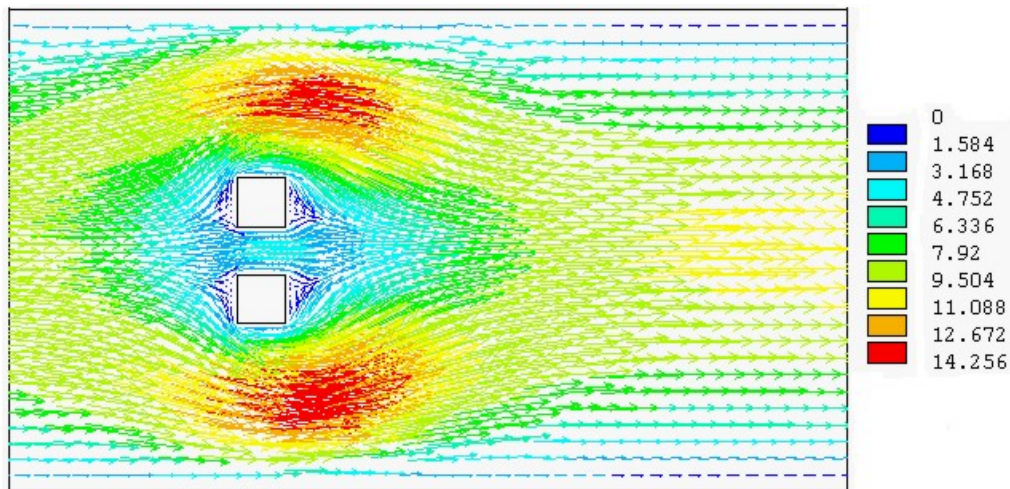


Fig. 2.1a: Computer simulation (2D simulation using Ansys Flotran 5.6) of the electrolyte flow near to two quadratic hindrances (white regions). The resulting local flow velocities are indicated by arrows, with the colour representing the value of the velocity according to the scale given at the right side of the Figure (numbers indicate „m/s“-values).

Simulation parameters: kinematic viscosity of fluid at 40°C: $1.357 \times 10^{-6} \text{ m}^2/\text{s}$, flow velocity at channel inlet: 7 m/s, flow velocity at walls: 0 m/s. Dimensions of artificial, quadratic hindrances: 1mm x 1mm x 1mm.

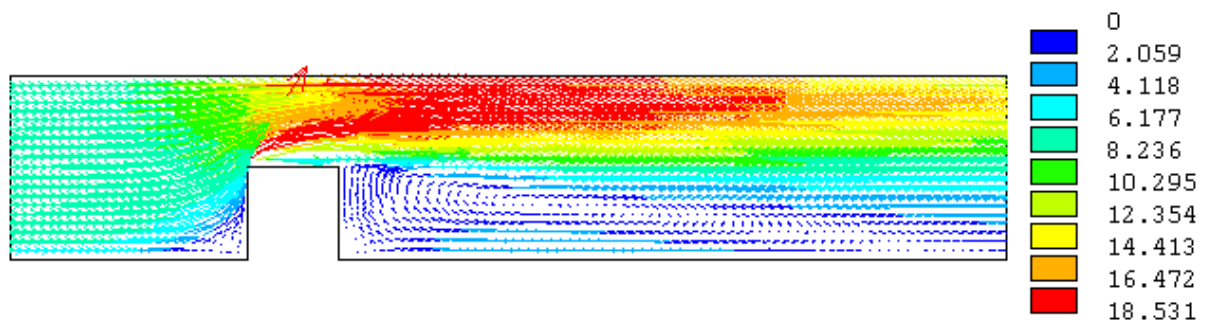


Fig. 2.1b: Side view of a quadratic hindrance disturbing the electrolyte flow within the flow channel cell (same simulation parameters as for Fig. 2.1a).

With the 2D simulation results given here, it becomes obvious that directly in front of and behind the hindrances, localized permanent eddies develop (see the blue zones in Figs. 2.1a and 2.1b) which play an important role in the high rate anodic dissolution process of inhomogeneous steel substrates. The absolute flow velocity within the eddies is significantly decreased (≤ 2 m/s) in comparison with the average flow velocity at the channel inlet (7 m/s).

2.4 Comparison of 2D-simulation with experimental results

As a result of the 2D-simulations shown in Section 2.3, localized permanent eddies develop in front of and behind the quadratic hindrances in the electrolyte flow. To investigate the influence of these eddies on the high rate metal dissolution process, an ECM-experiment with the flow channel cell has been carried out with the same geometrical parameters as given in Section 2.3. The surface morphology (top view) of the steel 100Cr6 after ECM is shown in Fig. 2.2:

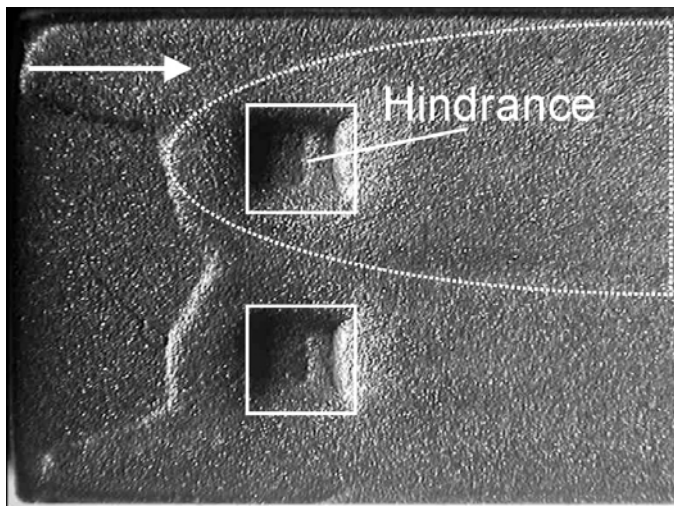


Fig. 2.2: Topography of a 100Cr6 steel substrate after ECM (top view). Electrolyte: NaCl (40 wt.%), 40°C, 7 m/s, 20 A/cm², 90 s. The electrolyte flow direction is indicated by the white arrow in the upper left. Dimensions of artificial, quadratic hindrances: 1mm x 1mm x 1mm.

Considering the topography presented in Fig. 2.2, the influence of the electrolyte flow becomes obvious. It is clearly visible that, in comparison with the region at the left

side of Fig. 2.2, directly in front of the artificial hindrances much higher metal removal rates have occurred (note the sharp contrast lines in Fig. 2.2). This means, that localized turbulences within an NaCl electrolyte increase the local metal removal rate. In chapter 3, this effect will be discussed in detail.

Chapter 3

Influences of material inhomogeneities in 100Cr6 steel on the electrochemical metal dissolution process

Thomas Haisch, Eric Jan Mittemeijer and Joachim Walter Schultze

Abstract

The electrochemical metal dissolution of 100Cr6 steel in sodium chloride solution, applying high electrolyte flow rates and high current densities, has been studied with a view to the influence of material heterogeneities such as carbide segregation lines in the steel matrix. It was shown that the presence of such segregations is responsible for the formation of troughs on the specimen surface during electrochemical dissolution. A mechanism for trough formation was proposed. A dedicated heat treatment applied to the 100Cr6 steel eliminated the carbide segregation lines and established a soft annealed, fine-grained microstructure containing globular carbides. Subsequent electrochemical dissolution did not show any development of surface irregularities as troughs.

3.1 Introduction

The anodic dissolution of metallic materials under high electrolyte flow rates and high current densities is of great interest for industrial applications to create specific workpiece geometries like holes or rounded edges. This process is called electrochemical machining. The process can be applied to metals like iron, nickel or aluminium, with variable results regarding the resulting surface quality [42]. Especially inclusions of nonmetallic compounds and element segregations affect the results of this surface treatment. The overall surface finish strongly depends on the amount of such inclusions within the specimen. Sulphides as inclusions in working steels usually have small dimensions ($< 20 \mu\text{m}$) and thus the pitting effect around a single inclusion decreases with increasing metal removal. However, in some commercially available carbon steels the segregation lines of the alloying elements can be of much larger extent (length $> 500 \mu\text{m}$) [43].

This paper describes the effect of element segregation in 100Cr6 steel on the electrochemical dissolution process in concentrated NaCl electrolytes. It will be shown that a dedicated heat treatment applied to 100Cr6 eliminates the segregation and, thereby, the undesirable surface morphology upon electrochemical dissolution.

3.2 Experimental

3.2.1 Specimen preparation

100Cr6 steel rods (cold rolled and soft annealed, diameter 4 cm) were commercially acquired; for composition, see Table 3.1. For the electrochemical dissolution experiments, specimens of dimensions 2 cm x 1 cm x 1.5 cm were cut out of the centre of the rod. The surfaces of the specimens were ground on SAPHIR 330 machines (250 rpm) using SiC-papers with, successively, the grain sizes of 46, 35, 18 and 15 μm . Thereafter, the specimen surfaces were polished mechanically on STRUERS DAP-7 machines (250 rpm) using SOMMER diamondpastes with, successively, 6, 3 and 1 μm grain size.

Table 3.1: Chemical composition of the 100Cr6 steel in weight percent.

Element	C	Cr	Si	Mn	Ni	P	S	Fe
wt. %	0.97	1.43	0.28	0.28	0.11	0.006	0.002	96.91

3.2.2 Electrochemical dissolution

The electrochemical dissolution experiments were carried out in a rectangular flow channel, often called parallel plate reactor (Fig. 3.1). The average electrolyte flow velocity was set at 7 m/s, implying turbulent flow conditions within the reactor. A platinized copper / tungsten alloy was used as cathode material. The 100Cr6 specimens served as anode. The distance between cathode and anode (often called working gap) was set at 2 mm at the start of the experiment. An aqueous NaCl solution (20 wt. %) at 40°C served as electrolyte. All experiments were done under galvanostatic conditions with an average current density of 20 A/cm². Direct current was selected using a rectifier with 40 V maximum voltage. The specimens were subjected to the electrochemical dissolution for 40 s. Then they were removed quickly from the reactor and washed with distilled water. The time between the electrochemical dissolution and the washing procedure was about 20 s.

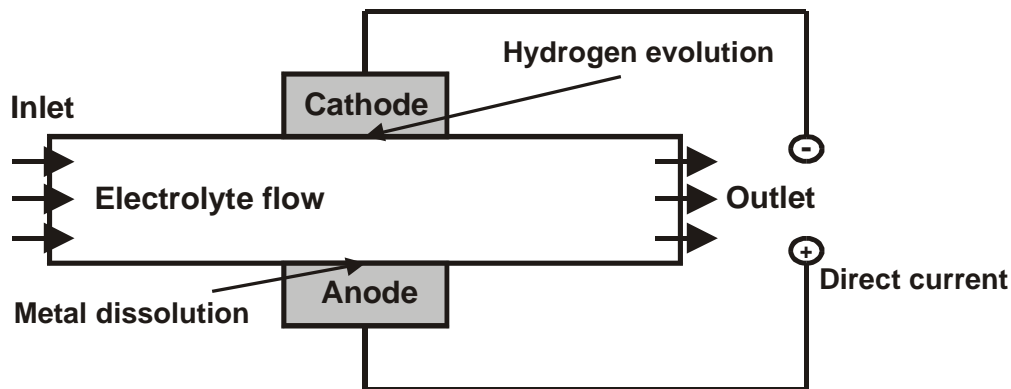


Fig. 3.1: Schematic presentation of the anodic metal dissolution in the flow channel (often called parallel plate reactor).

3.2.3 Metallography

The preparation of microsections for light microscopic investigation was done by grinding and polishing as described in Section 3.2.1. Thereafter etching was performed using either a 2% solution of nitric acid in amyl alcohol (nital) or the Oberhoffer solution, prepared from: 500 cm³ H₂O, 500 cm³ ethanol, 50 cm³ HCl, 30g FeCl₃, 1g CuCl₂, 0.5 g SnCl₂ [44]. The Oberhoffer etching solution is normally used

for revealing segregations of phosphorus and sulphur in steels. In this investigation it will be shown that metal carbide segregations in 100Cr6 can be clearly detected using Oberhoffer's reagent.

EPMA measurements were performed with a Cameca SX100 EPMA system equipped with 5 wavelength dispersive spectrometers and a PGT energy dispersive spectrometer. A focussed electron beam of 15 kV and 100 nA was used to generate characteristic X-rays. The element concentration values were calculated from the intensity ratios applying the $\Phi[\rho z]$ approach of Pouchou and Pichoir [45].

Scanning electron microscopy (SEM) and energy-dispersive X-ray microanalysis (EDX) were carried out using a RJ Lee Instruments Ltd. PSMART 75 B/AFA with a Premium Si (Li) detector and an acceleration voltage of 20 kV.

3.2.4 Heat treatment

For all annealing experiments performed in this work the specimens were put in capsules of silica glass containing pure argon at 50 kPa (at room temperature) as protective gas. A muffle furnace was used to carry out the heat treatment (see Section 3.3.4).

3.3 Results and discussion

3.3.1 As prepared condition

The microstructure of the 100Cr6 steel is shown in Fig. 3.2 (nital etched). The grain size, determined from such sections, was classified as 6 according to DIN 50601 (i.e. $\sim 45 \mu\text{m}$ diameter). Segregation „lines“, ascribed to aggregation of carbide particles, appear as dark lines in the micrograph. The lines are oriented parallel to the rolling direction of the steel rod. Microsections etched by Oberhoffer (Fig. 3.3) show the same segregation „lines“ as white lines and thus appear to be optical negatives of those etched by nital.

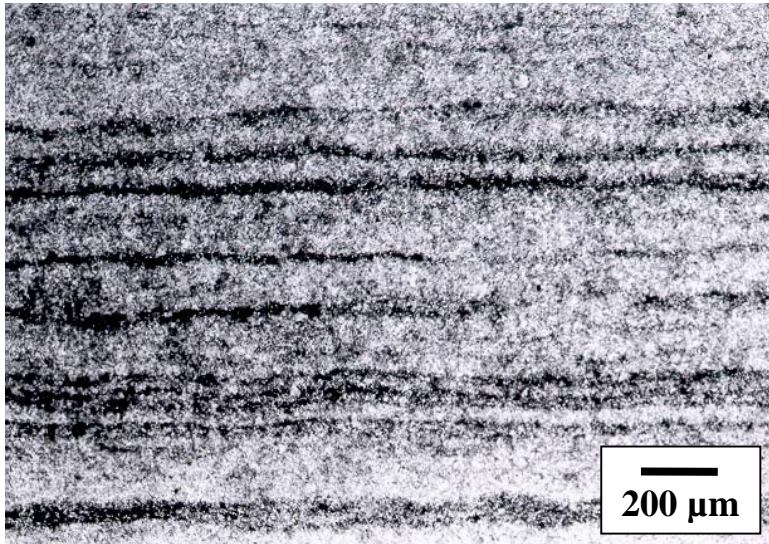


Fig. 3.2: Optical micrograph (bright field) of a cross-section (nital etched) of steel 100Cr6. The carbide segregation lines (dark) in the direction of rolling (horizontal in the micrograph) can be observed.

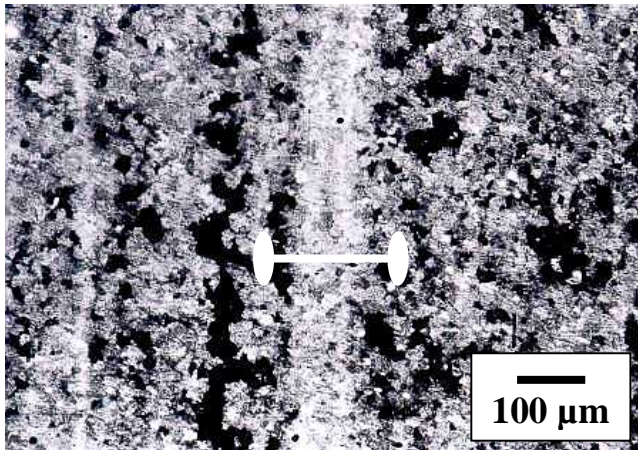


Fig. 3.3: Optical micrograph (bright field) of a cross-section of steel 100Cr6, after etching with Oberhoffer's reagent. The white line represents the EPMA scan given in Fig. 4. Note the contrast reversal for the carbide segregation lines: white after Oberhoffer etching; black after nital etching (see Fig. 3.2).

It is well known that the soft annealed working steel 100Cr6 contains globular carbides of the composition M_3C , which can include up to 20 wt. % chromium [46]. An EPMA analysis was performed on the cross-section (Fig. 3.3) to exhibit the compositional variation. The element distribution along the line (Fig. 3.3) is shown in Fig. 3.4a. At the location of a segregation line the carbon and chromium

concentrations are much higher than the corresponding average values (C: 0.97 wt. %, Cr: 1.43 wt. %; cf. Table 3.1).

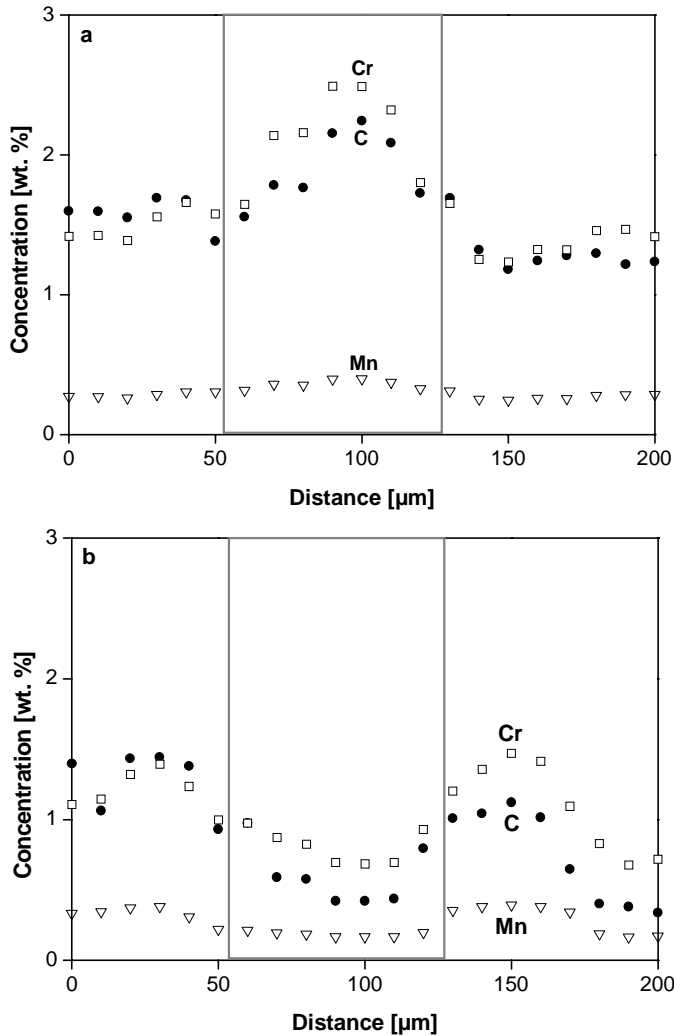


Fig. 3.4:

The element distribution as determined by EPMA analysis along the line in the cross-section shown in Fig. 3.3.

(a) High concentrations of carbon and chromium occur within the segregation line indicated by the rectangular box. The results were plotted using the moving average of 4 points.

(b) After the heat treatments indicated in Figs. 3.10 and 3.11.

3.3.2 Results of anodic metal dissolution

During the electrochemical treatment of the 100Cr6 specimens a solid black surface film was formed on the specimen surface. This surface layer was not strongly attached to the substrate surface and could be washed off with distilled water. To determine the chemical composition of this surface film, after the washing treatment the film was picked up on a nylon filter. To remove remains of the NaCl electrolyte the picked-up film was washed further with 250 ml distilled water. SEM and qualitative EDX results are shown in Fig. 3.5. It follows that the surface film is basically constituted of iron, chromium and carbon.

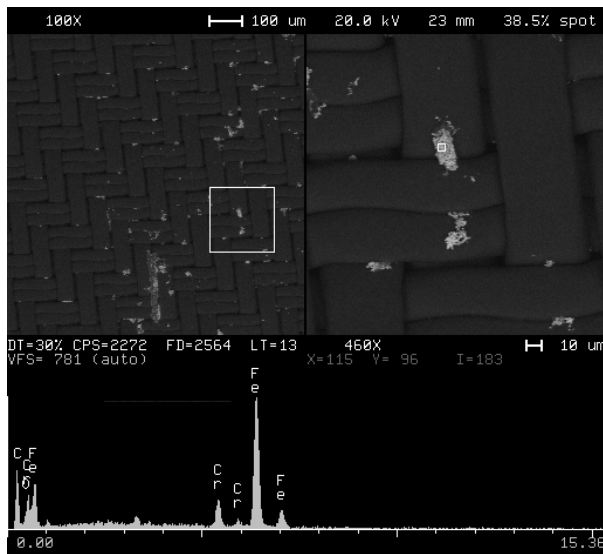


Fig. 3.5: Scanning electron micrographs of particles originating from the surface film formed on 100Cr6 upon electrochemical metal dissolution, and as picked up on a nylon filter (dark pattern in the background of the images). The composition of the particles (bright) has been examined by EDX, see the bottom of the figure (the horizontal axis indicates the eV values).

The surface morphology of the substrate after the electrochemical treatment is illustrated with Figs. 3.6a - c.

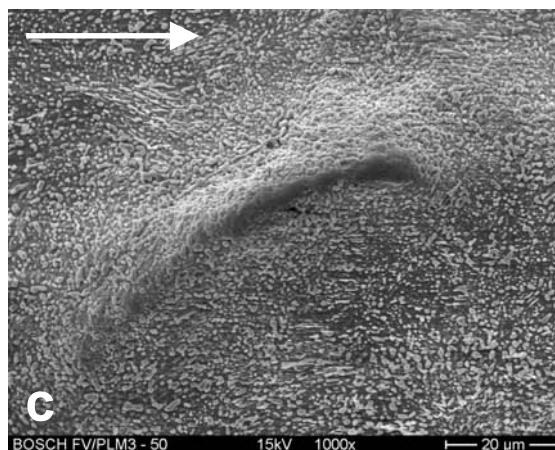
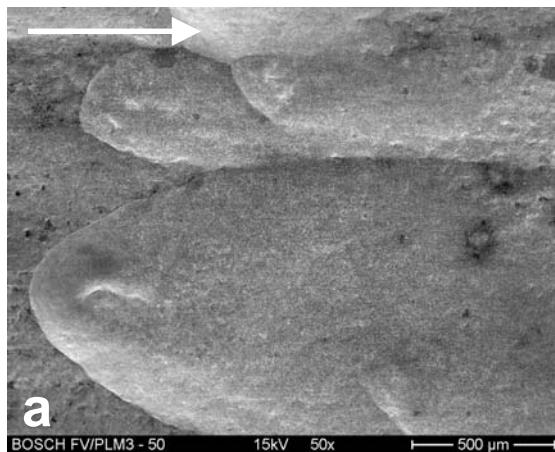


Fig. 3.6: Scanning electron micrographs: (a) trough formations on the 100Cr6 surface, (b) single trough on the 100Cr6 surface, and (c) centre of the trough shown in (b): carbide segregation.

The electrolyte flow direction is shown by the arrow in the upper left corner of the SEM micrographs. Massive formation of streaks (elongated depressions; troughs) has occurred. In the centre of a streak carbide segregation is evident: a significant difference in chromium concentration exists between the centre of a trough and the steel matrix outside the trough (see Figs. 3.7a and b).

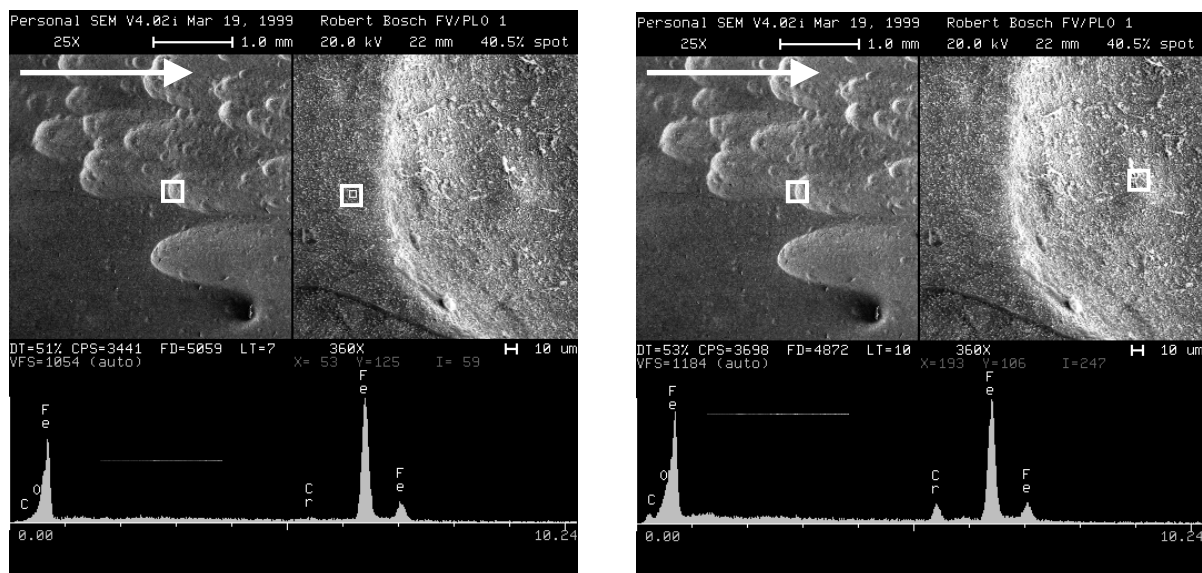


Fig. 3.7: Scanning electron micrographs of the 100Cr6 surface after electrochemical metal dissolution. The arrow in the upper left corner indicates the electrolyte flow direction. Qualitative EDX analysis at a region outside of a trough **(a)** and in the centre of a trough **(b)**. As compared to the results shown in **(a)**, significantly higher C and Cr concentrations are observed.

The specimen orientation in the experiment, corresponding to Figs. 3.6 and 3.7, was such that the rolling direction, and thus the direction of the carbide segregation lines, was perpendicular to the electrolyte flow direction. The local topography of flow streaks strongly depends on the electrolyte flow direction within the parallel plate reactor: „comet shaped pits“ are formed with significant, elongated depressions in the direction of the electrolyte flow (cf. Fig. 3.6).

3.3.3 Mechanism of streak formation; simulation

Surface structures with a morphological appearance similar to those observed here have been reported [46] as the result of „erosion-corrosion“ experiments concerning copper in NaCl solutions [47]. In that case it was supposed that a solid surface film formed by corrosion products like CuO can be „broken up“ by localized turbulences in the flow adjacent to the surface. Against this background the following erosion-corrosion mechanism for the present anodic metal dissolution processes of carbon containing steels may be proposed: see Fig. 3.8.

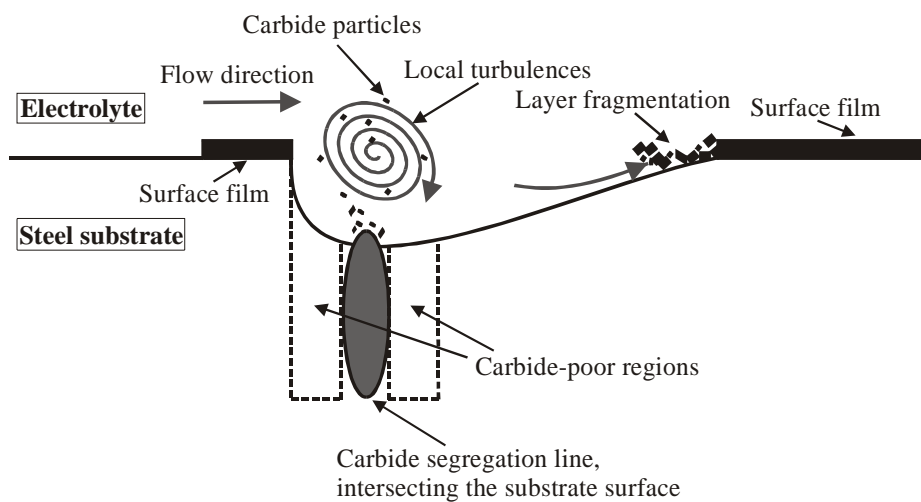


Fig. 3.8: Schematic presentation of the proposed mechanism of the local erosion, leading to the formation of depressions (troughs) in the steel substrate surface upon electrochemical metal dissolution applying high electrolyte flow rates and high current densities.

A surface film forms on the specimen surface upon electrochemical metal dissolution (see Section 3.3.2). This surface film is loosely bound to the substrate. The thickness and the chemical composition of the surface film may vary distinctly on a local scale because of the compositional heterogeneity of the substrate (see Section 3.3.1). For example, the carbide poor regions adjacent to a carbide segregation line can be considered as regions where relatively strong metal dissolution can take place. Break-throughs of the correspondingly relatively thin, loosely bound to the substrate, films may occur enhancing the formation of the depressions (troughs) in the substrate surface. The formation of these troughs in combination with the high flow rate of the

electrolyte can lead to the development of strong turbulences at the location of the troughs. Carbide particles in the liquid, which were originally part of the film or stem from the carbide segregation line in the substrate, may then actually „hammer“ on the solid: erosion-corrosion.

A 2-dimensional simulation of the flow velocity distribution of the electrolyte within and close to a trough on the specimen surface was performed. A standard turbulence model was adopted for the simulation [48], which was carried out using the program Ansys Flotran 5.6 [49]. The properties of the flowing liquid were assumed to be constant: local variations in the electrolyte density, viscosity or temperature were not allowed. The electrolyte flow velocity adjacent to all walls of the flow channel was set to 0 m/s. The overall flow velocity at the channel inlet was set to 7 m/s. The geometry of the trough was taken as a circle with 100 μm diameter. All parameters used for the calculation (geometry of the flow channel, average flow velocity, viscosity and density of the electrolyte) were set to values corresponding to the metal dissolution experiments. The result of the calculation is visualised in Fig. 3.9.

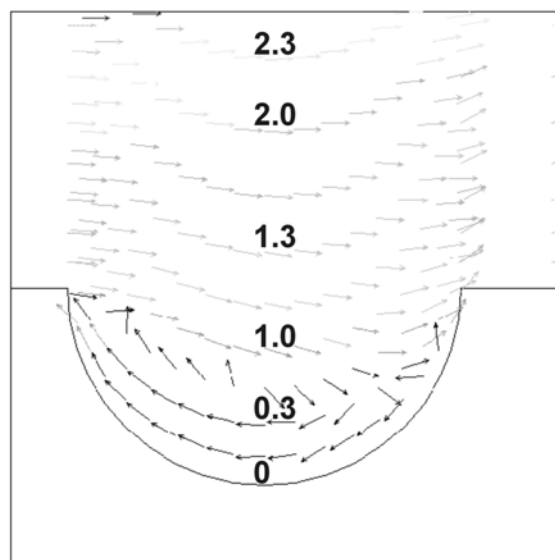


Fig. 3.9: Computer simulation of the electrolyte flow within and close to a trough (2D simulation using Ansys Flotran 5.6). The resulting local flow velocities are indicated by the arrows, with greyness representing the value of the velocity according to the scale given at the right side of the figure (numbers indicate „m/s“-values). A localized eddy can be observed in the centre. The total flow velocity at the bottom of the trough is much smaller than the main stream velocity. Simulation parameters: kinematic

viscosity of the fluid: $1.357 \times 10^{-6} \text{ m}^2/\text{s}$, flow velocity at the channel inlet: 7 m/s, flow velocity at the walls: 0 m/s.

Evidently, within the trough the overall flow velocity is much lower than within the mainstream, shown in the upper region of the figure. The presence of the permanent eddy in the centre of the trough should be noted: this type of turbulences is thought to be responsible for the erosion-corrosion discussed above (Fig. 3.8).

The above mechanism explains that the presence of carbide segregation lines in the steel substrate is associated with the formation of troughs upon electrochemical metal dissolution applying high electrolyte flow rates and high current densities as in applications of electrochemical machining.

3.3.4 Avoiding streak formation; microstructure modification

The above proposed mechanism for trough formation immediately suggests the remedy to avoid this effect: carbide segregation in the steel specimens should be avoided or eliminated. The heat treatment shown in Fig. 3.10 was performed, recognizing the available 100Cr6 phase diagram data [43]. The highest annealing temperature applied for diffusion annealing was 1200°C because of the danger of melting at the grain boundaries: temperatures above 1200°C belong to the liquid + γ -phase region of the 100Cr6 steel [43]. Soft annealing at 730°C was carried out in the second part of the heat treatment, thereby remaining within the α + M_3C -phase region of the steel. A very long annealing time of 180 h was chosen to assure that the carbides were of the composition M_3C with no compositional variations. The grain size of the thus heat-treated specimens was classified as 0 [i.e. $\sim 350 \mu\text{m}$ diameter] (DIN 50601). The resulting element distribution, as determined by performing an EPMA scan in a cross-section of the heat-treated specimen, is shown in Fig. 3.4b. Evidently, the initial, distinct carbon and chromium segregation, as visible in Fig. 3.4a, has been reduced significantly by the executed heat treatment.

A very coarse-grained structure can lead to large surface irregularities upon electrochemical metal dissolution due to preferred dissolution at the grain boundaries [50]. Therefore, after the heat treatment according to Fig. 3.10, recrystallization of the steel was carried out applying the heat treatment shown in Fig. 3.11. Two times the

100Cr6 specimen was annealed at 870°C for 20 min with the aim of initiating a $\alpha \rightarrow \gamma$ -phase change by annealing within the $\gamma + M_3C$ -phase region. This phase change is accompanied with the formation of new, small grains. After carrying out the recrystallization, a long soft annealing period of 180 h at 730°C was chosen again to obtain the same specimen condition as before and as described in Section 3.2.1 (soft annealed, globular M_3C carbides). The resulting microstructure after the heat treatments is shown in Figs. 3.12a and b. Clearly a homogeneous microstructure has been achieved. The grain size of the thus recrystallized and soft annealed specimens was determined as 6 [i.e. $\sim 45 \mu\text{m}$ diameter] (DIN 50601).

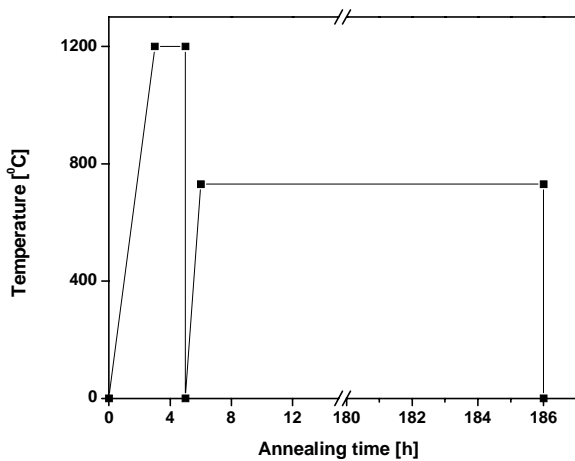


Fig. 3.10: Heat treatment applied to 100Cr6 to eliminate carbide segregation lines: diffusion annealing at 1200°C (2 h) followed by a soft annealing at 730°C (180 h).

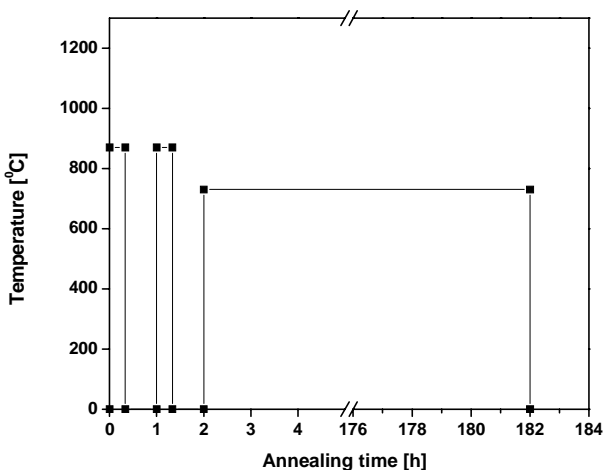


Fig. 3.11: Recrystallization heat treatment applied to 100Cr6. Two times recrystallization annealing for 20 min at 870°C, followed by 180 h of soft annealing at 730°C.

The surface morphology after the electrochemical treatment applied to the heat-treated specimens is shown in Figs. 3.13a and b. A flat surface has resulted; no formation of troughs has occurred. The globular carbides (M_3C) at the treated surface can be observed in Fig. 3.13b; they appear to have been not dissolving in the electrochemical dissolution process.

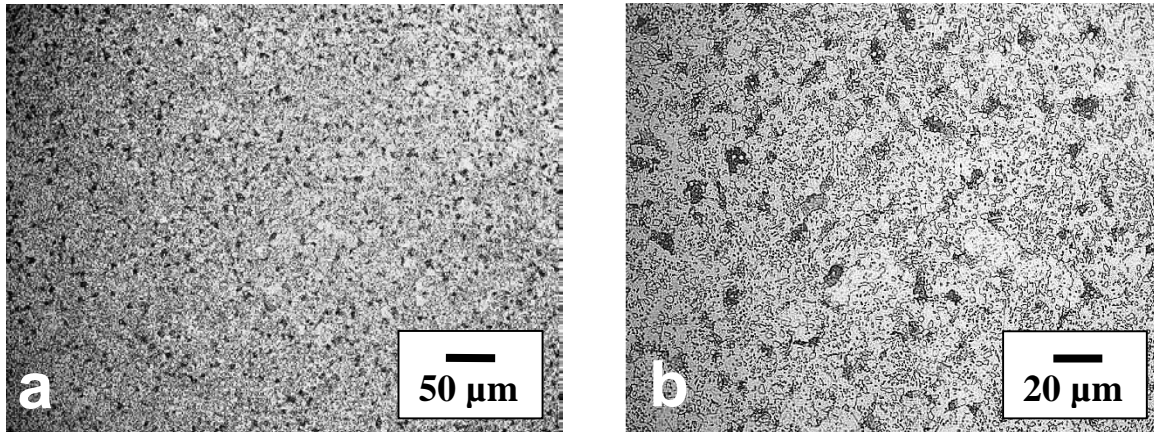


Fig. 3.12: Optical micrographs (bright field) of cross-sections (nital etched) of steel 100Cr6 after the heat treatments indicated in Figs. 3.10 and 3.11.

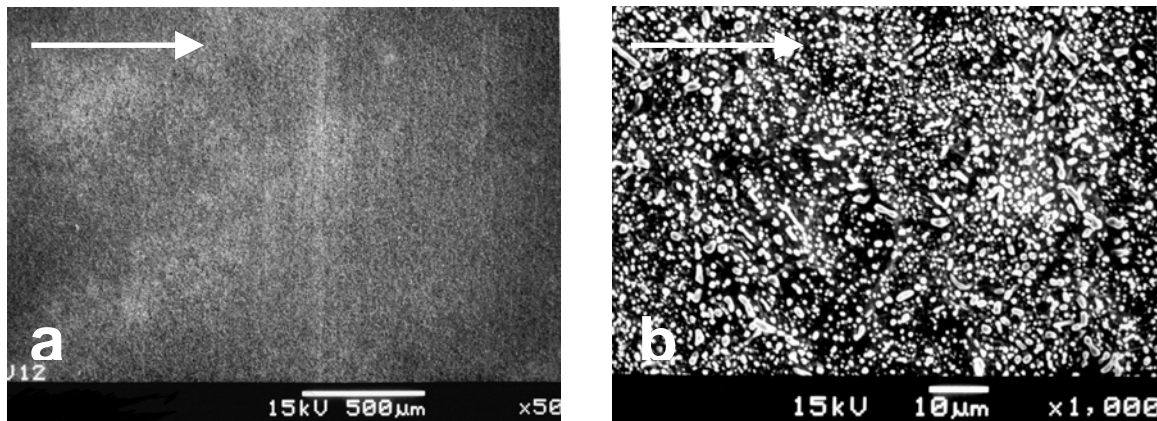


Fig. 3.13: Scanning electron micrographs of steel 100Cr6 (after executing the heat treatments indicated in Figs. 3.10 and 3.11) after electrochemical metal dissolution. The arrow in the upper left corner indicates the electrolyte flow direction. The bright spots in (b) are due to the globular carbide particles (M_3C) in the steel matrix.

3.4 Conclusions

1. Carbide segregation in a steel matrix leads to large, macroscopical metal surface irregularities (formation of troughs) upon electrochemical metal dissolution applying high electrolyte flow rates and high current densities, as in electrochemical machining applications.
2. An „erosion-corrosion“ mechanism could be responsible for macroscopic trough formation in the metal surface: at the regions in the metal surface

relatively poor in carbide, break-through of the correspondingly very thin carbide film, developing upon electrochemical metal dissolution, is relatively easily realizable and subsequently carbide particles in the liquid can „hammer“ the solid film due to enhancement of turbulence in the liquid at the locations of trough development.

3. A dedicated heat treatment can remove all macroscopic carbide segregations, and subsequently establish a fine-grained microstructure.
4. The homogeneous microstructure leads to light microscopically flat steel substrate surfaces upon electrochemical metal dissolution applying high electrolyte flow rates and high current densities.

Chapter

4

Electrochemical Machining of the steel 100Cr6 in aqueous NaCl and NaNO₃ solutions: Microstructure of surface films formed by carbides

Thomas Haisch, Eric Jan Mittemeijer and Joachim Walter Schultze

Abstract

Application of Electrochemical Machining (ECM) in microsystem technologies has to take into account the role of microscopic heterogeneities of the steel, e.g. of carbides. Therefore, the anodic metal dissolution of the alloyed carbon steel 100Cr6 was investigated in NaCl- and NaNO₃-electrolytes. In flow channel experiments, high current densities up to 70 A/cm² and turbulent electrolyte flow velocities were applied. Insoluble carbide particles cause an apparent current efficiency >100% in NaCl and >67% in NaNO₃. These particles are enriched at the surface in NaCl solution and detected by *ex situ* scanning electron microscopy (SEM) and energy dispersive X-ray (EDX)-experiments. Auger electron spectroscopy, in combination with sputter depth profiling, was used to determine the film composition resulting from the NaNO₃-process. This proves the enrichment of carbide particles not yet separated from the surrounding steel. Qualitative metal dissolution models on the basis of the experimental results were proposed for the metal dissolution processes in the NaCl- and NaNO₃-electrolytes.

4.1 Introduction

High rate metal dissolution under current densities up to 70 A/cm^2 and high electrolyte flow rates, also known as Electrochemical Machining (ECM), has been investigated by many authors [20, 21, 51-55]. In microsystem technologies, it plays an important role for two reasons. At first, it allows microstructuring of hard metals like Fe and Ti in the μm range if correspondent microelectrodes are available [55]. Second, it is a technology without mechanical surface damage as it appears during mechanical polishing, spark erosion or other techniques [52]. Now it is widely applied e.g. for preparation of miniaturized nozzles for motor injection devices, for deburring, for razor head production and other systems [52].

It is well known, that the choice of electrolyte strongly influences the result of this technologically important surface finishing process. Especially aqueous solutions of NaCl, NaNO_3 and NaClO_3 have been studied with respect to their influence on the anodic polarization, the substrate surface morphology and the overall metal removal rate [56-59]. Most of the reported anodic dissolution experiments have been carried out using pure metals, like iron and nickel, as substrates. For these systems quantitative dissolution models have been proposed mainly on the basis of a mass transport controlled ECM-process [60]. The diffusion layer in the liquid forming on the substrate surface upon Electrochemical Machining and the formation of a very thin salt layer directly on the substrate surface have been studied by many workers [61, 62]. However, not much is known about the complex dissolution behaviour of technical carbon steels because of their heterogeneous microstructure based on the steel matrix including metal carbides and non-metallic inclusion compounds like oxides and sulfides.

The present study was initiated to better define the metal removal mechanisms in the high rate electrochemical dissolution of the steel 100Cr6 using the passivating electrolyte NaNO_3 and the non-passivating, more corrosive NaCl-electrolyte. The influence of microscopic heterogeneities was of special interest. It will be shown that insoluble particles cause the formation of different surface films.

4.2 Experimental

4.2.1 Specimen preparation

100Cr6 steel rods were commercially acquired (in cold rolled and soft annealed condition, C wt.%: ≈ 1 , diameter: 4 cm); for composition, see Table 4.1. The carbide particles have a diameter of about 0.5 μm (see Section 4.3.4). For the electrochemical dissolution experiments, specimens of dimensions 2 cm x 1 cm x 1.5 cm were cut out of the centre of the rod. The surfaces of the specimens were ground using SiC-papers with, successively, the grain sizes 46, 35, 18, 15 μm . Thereafter the specimen surfaces were polished mechanically using SOMMER diamond-pastes with, successively, 6, 3 and 1 μm grain size.

Table 4.1: Chemical composition of 100Cr6 specimen (wt.%).

Element	C	Cr	Si	Mn	Ni	P	S	Fe
wt.%	0.97	1.43	0.28	0.28	0.11	0.006	0.002	96.92

4.2.2 Flow channel

The electrochemical dissolution experiments were carried out in a rectangular flow channel, often called parallel plate reactor. The average electrolyte flow velocity was set at 7 m/s, implying turbulent flow conditions within the reactor. Platinized copper / tungsten alloy was used as cathode material. The 100Cr6-specimens served as anode. The distance between cathode and anode (often called working gap) was set at 2 mm at the start of the experiment. Aqueous solutions of NaCl (20 wt.%) and NaNO_3 (40 wt.%) at $40^\circ\text{C} \pm 1^\circ\text{C}$ served as electrolytes. All experiments were done under galvanostatic conditions with current densities up to 70 A/cm^2 . Direct current was selected using a rectifier with 40 V maximum voltage. After each ECM-experiment the specimens were removed quickly from the reactor and washed with distilled water. The time between the electrochemical dissolution and the washing procedure was about 20 seconds.

4.2.3 Rotating cylinder electrode (RCE)

The measurement of anodic polarization curves was carried out using a rotating cylinder (1.2 cm diameter) with a 100Cr6-working electrode, a platinum net as counter electrode and a commercially obtained Ag/AgCl/KCl-reference electrode. In this paper, all potentials are referred to the standard hydrogen electrode (NHE). The distance between the working and counter electrode was set to 1 cm. All polarization measurements were performed potentiodynamically and the electrolyte temperature was maintained at $25 \pm 1^\circ\text{C}$. The scan rate for all polarization experiments was set to 40 mV/s.

4.2.4 Weight loss measurements

The determination of the weight loss of the 100Cr6 specimens was carried out using gravimetric measurements. To determine the specimens weight loss after the ECM-experiment the removable parts of the developed black solid surface film were washed away with distilled water.

4.2.5 SEM, EDX, AES

Scanning electron microscopy (SEM) and energy dispersive X-ray microanalysis (EDX) were carried out using a RJ Lee Instruments Ltd. PSMART 75 B/AFA with a Premium Si (Li) detector and an acceleration voltage of 20 kV.

AES spectra were recorded with a PHI 600 Scanning Auger Microprobe equipped with a single pass cylindrical mirror analyser with an energy resolution of 0.6 %. Survey spectra were recorded using a 10 keV primary electron beam with a current of 1 μA . The rastered area for the survey was $50 \times 50 \mu\text{m}^2$. A sputter-depth profile was recorded over an area of $1 \times 1 \text{ mm}^2$ at an incidence angle of 60° with respect to the surface. As a measure for the peak intensities the peak-to-peak height of the differentiated spectra was used. The sputter rate of a Ta_2O_5 -reference was determined as 16 nm/min.

4.3 Results

4.3.1 Current efficiency

The current efficiency for the 100Cr6 dissolution was determined by weight loss measurements assuming divalent metal ion formation according to:



Metal carbides and inclusion compounds in the steel matrix were assumed to be inert, i. e. not dissolving electrochemically. For the calculation of the current efficiency the experimental weight loss, ΔW_{ex} , was compared with the theoretical value, ΔW_{theo} , obtained from the following equation:

$$\Delta W_{\text{theo}} = \frac{MIt}{nF} \quad (4.2)$$

Here M is the atomic weight of the dissolving atoms type, I is the applied current, t the dissolution time and F is the Faraday constant. The valence of dissolution, n , was taken as 2. Then, the current efficiency η can be defined as follows:

$$\eta = \frac{\Delta W_{\text{ex}}}{\Delta W_{\text{theo}}} \quad (4.3)$$

Fig. 4.1 shows the current efficiencies for the NaCl- and the NaNO₃-electrolytes obtained by experiments with the flow channel. The values of Armco-Iron show the 100% for NaCl expected for divalent iron dissolution. The current efficiencies for 100Cr6 exceed this standard value up to 10 %. This can be explained by the erosion of inert particles (for example metal carbides and oxides) which are not electrochemically dissolved in the ECM-process but are detected by the weight loss measurement of the specimen. The dependence on the current density is small: even at low current densities of 1 A/cm² and below metal dissolution is observed with a current efficiency of 95%.

The current efficiencies obtained for NaNO₃-electrolyte (40 wt.%) differ strongly. Up to 9 A/cm² no or only a very small metal removal can be observed, associated with a current efficiency of 0%. Between 9 and 11 A/cm² a „breaking-through“ current density region is detected: a steep increase of current efficiency occurs for Armco-iron up to 67 % [54] corresponding to a trivalent iron dissolution mechanism. For 100Cr6 again an excess efficiency is observed due to the removal of insoluble species.

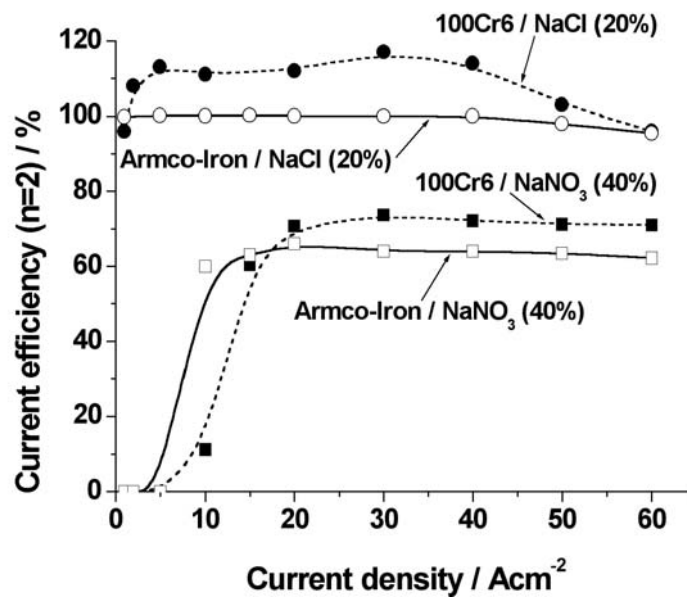


Fig. 4.1: Current efficiencies of the soft annealed steel 100Cr6 obtained by galvanostatic flow channel experiments with NaCl (20%) and NaNO₃ (40%). The corresponding values for Armco-Iron are given for comparison. Average electrolyte flow velocity: 7m/s.

4.3.2 Anodic polarization curves

The current density as a function of the applied anodic potential has been investigated for both the NaCl-electrolyte and the NaNO₃-electrolyte using the rotating cylinder electrode at various rotation speeds (Fig. 4.2). The calculation of the Reynolds-numbers was carried out using equation (4.4):

$$Re = \frac{\omega r^2}{\nu} \quad (4.4)$$

where ω is the angular velocity, r the radius of the working electrode and ν the kinematic viscosity of the electrolyte. Reynolds-numbers corresponding to applied rotation speeds are given in Table 4.2. $Re > 200$ indicates turbulent conditions [63].

In NaCl-solution, active metal dissolution starts at -0.1 V (vs. NHE) (see Fig. 4.2a). Up to +0.5 V, the current density i does not depend on the rotation speed. The polarization resistance is low, $R_p = 0.4 \Omega \text{ cm}^2 = R_{el} + R_{film} \approx R_{el}$. This is mainly due to the ohmic resistance of the electrolyte. In the potential region from +0.6 to +0.75 V (vs. NHE) a decrease of i can be found for increasing potential for the lower rotation speeds applied, indicating the formation of any surface film which hinders the

dissolution, but does not cause a larger potential drop as passive films do. This region can be minimized by increasing the electrode rotation speed (Fig. 4.2a). The overall current efficiency for the given anodic potential range was determined as 105% (for $n = 2$).

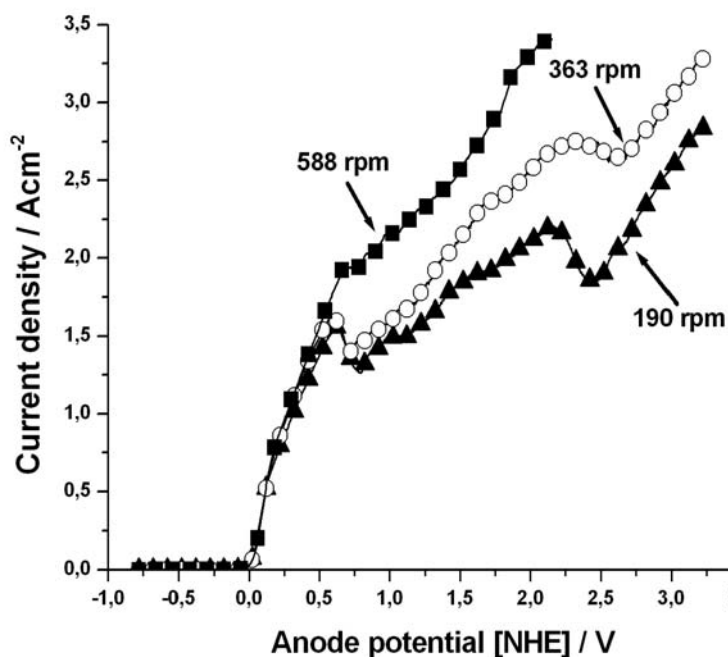


Fig. 4.2a: Anodic polarization curves of soft annealed steel 100Cr6 obtained by potentiodynamic experiments with rotating cylinder electrode at different rotation speeds. Electrolyte: NaCl (20%), scan rate 40 mV/s.

As discussed with Fig. 4.1, active metal dissolution does not occur in the NaNO_3 -system for the values of i given in Fig. 4.2b. Up to 1.8 V no current flow is observed due to the passivation of the surface. The approximately linear increase for anode potentials above +1.8 V is based on the onset of oxygen evolution on the specimen surface. This is in accordance with overall current efficiencies $\eta < 5\%$ (for $n=2$), as determined for this potential range. An increase of the electrode rotation speed does not lead to higher values of i . The value $R_p = 0.6 \Omega \text{ cm}^2$ exceeds that of NaCl, which indicates an appreciable contribution of the film resistance R_{film} . The relation $R_p (\text{NaCl}) / R_p (\text{NaNO}_3)$ is determined as 0.666. Comparison with the conductivities of the examined electrolytes ($\kappa_{\text{NaCl}} = 0.23 \text{ S/cm}$ and $\kappa_{\text{NaNO}_3} = 0.19 \text{ S/cm}$) shows, that

the relation $R_{el}(\text{NaCl}) / R_{el}(\text{NaNO}_3)$ with no contribution of the film resistance should be 0.826. Thus, the film resistance may be estimated as $R_{film} > 0.1 \Omega \text{ cm}^2$.

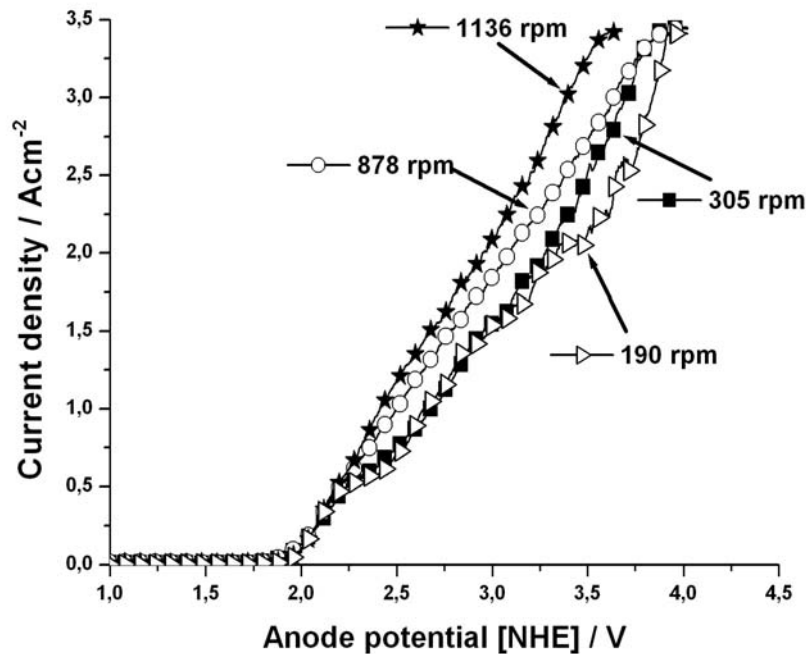


Fig. 4.2b: Anodic polarization curves of soft annealed steel 100Cr6 obtained by potentiodynamic experiments with rotating cylinder electrode at different rotation speeds. Electrolyte: NaNO_3 (40%), scan rate 40 mV/s.

Table 4.2: Calculated Reynolds-numbers for different anode rotation speeds.

Rotation speed / rpm	190	305	363	588	878	1136
Reynolds-number / Re	528	847	1006	1634	2439	3156

4.3.3 Surface-film formation

A black solid surface film forms on the 100Cr6 substrate surface during the high rate anodic dissolution in the flow channel. This film can be isolated and subsequently investigated *ex situ*. The adhesion of this surface film depends on the type of the ECM-electrolyte. The use of concentrated NaCl-electrolyte leads to a surface film constituted of loosely bound particles which can easily be removed from the specimen surface. In contrast to that, the anodic surface film formed in NaNO_3 -

electrolytes is strongly attached to the steel substrate, since it can not be removed from the specimen. To determine the chemical composition of the surface films formed in both systems two ways of specimen preparation were chosen.

The loosely bound particles formed on the 100Cr6 substrate using NaCl were picked up from the ECM-treated specimen surface by a Nylon-filter, washed with distilled water and investigated by SEM and EDX. A typical result is shown in Fig. 4.3.

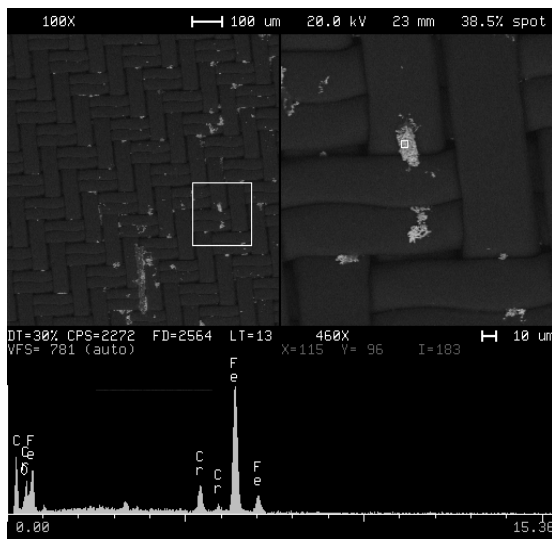


Fig. 4.3: Scanning electron micrographs of loosely bound particles of 100Cr6 surface film formed during galvanostatic flow channel experiment. EDX of single particle is given below. Dark pattern in the background is nylon filter. NaCl (20%), $i = 20 \text{ A/cm}^2$, 40 sec, 7 m/s, 40°C.

The strongly attached, not removable surface film on the 100Cr6 substrate obtained in NaNO_3 -electrolytes was washed intensively with distilled water and investigated *ex situ* by Auger electron spectroscopy in combination with sputter depth profiling. A typical depth profile is shown in Fig. 4.4.

Clearly, for both studied electrolyte-systems carbon-rich surface films develop during the electrochemical metal dissolution (Figs. 4.3 and 4.4). The particles formed in NaCl are mainly constituted of Fe, Cr and C which suggests that they originate from the carbides in the steel matrix (oxygen is found as well, but it is not clear if this is due to the washing procedure after the ECM-experiment). The depth profile of the surface film formed in NaNO_3 -electrolyte shows a similar result but the atomic concentration of Cr is very low. After removal of surface contamination during the first

minutes, the C-content of 30 atom % is very high indicating an enrichment of carbide particles at the surface by an preferential dissolution of Fe. Then, the C-content decreases from 30 to below 10 atom % after removal of about 2 μm film (100min sputtering) and approaches the theoretical bulk value of 4.5 atom %. It seems that the carbide is preferentially sputtered due to the smaller atomic weight of C.

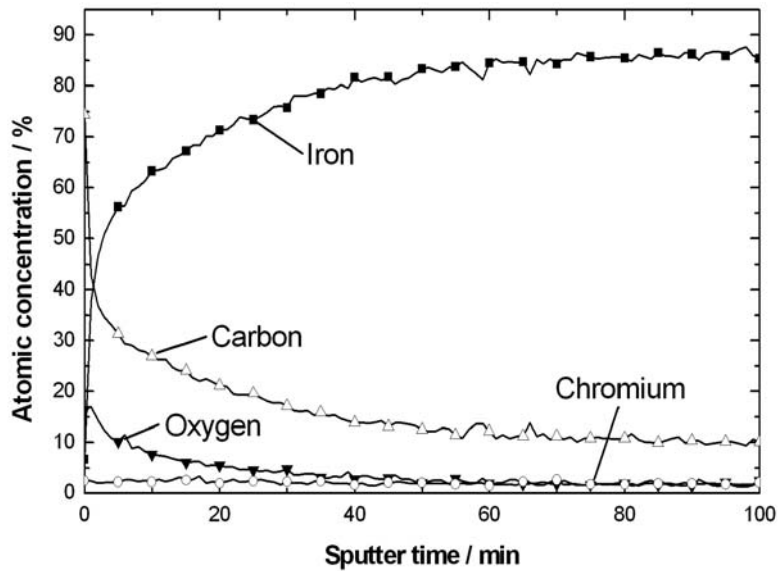


Fig. 4.4: Depth profile (Auger electron spectroscopy) of 100Cr6 surface film obtained by galvanostatic flow channel experiments. NaNO_3 (20%), current density: 20 A/cm^2 , average flow velocity: 7 m/s . Sputter rate of Ta_2O_5 -reference: 16 nm/min .

4.3.4 Substrate surface morphologies

Using NaCl -electrolyte, a blank metal surface is obtained after electrochemical metal dissolution, showing not dissolved globular carbides embedded by the steel matrix (note that the black surface film on the 100Cr6 specimen was removed by the washing procedure). Fig. 4.5a shows the scanning electron micrograph of a 100Cr6 surface after the ECM-treatment with NaCl (20 wt.%). Obviously, the ferrite has been electrochemically dissolved during the ECM-process while the metal carbides have been inert (small spheres of $0.5 \mu\text{m}$). Similar observations have been reported as the result of pulse polishing experiments with selected steel specimens [64]. Segregations within the 100Cr6 steel substrate can cause large scale irregularities,

such as troughs, upon the electrochemical metal dissolution with aqueous NaCl-solutions (see Fig. 4.5b). This effect is discussed elsewhere [65].

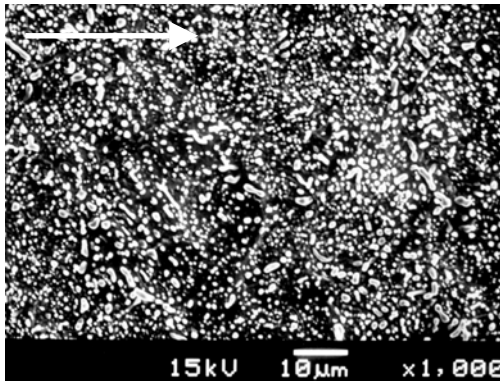


Fig. 4.5a: Scanning electron micrograph of 100Cr6 surface after ECM in flow channel. Current density: 20 A/cm², 40 s, average flow velocity: 7m/s, NaCl (20%). Flow direction is given upper left.

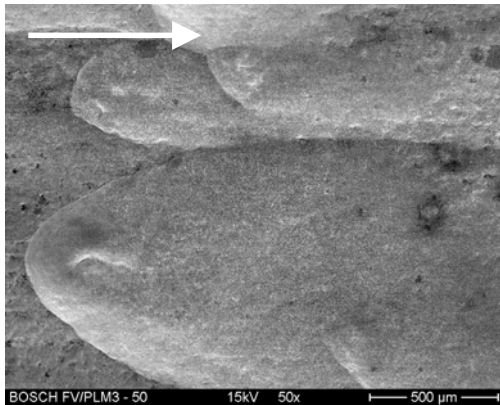


Fig. 4.5b: Scanning electron micrograph of a heterogeneous 100Cr6 specimen surface after ECM in flow channel. Current density: 20 A/cm², 40 s, average flow velocity: 7 m/s, NaCl (20%). Trough formations on the substrate surface are visible.

The 100Cr6 surface morphology resulting from the metal dissolution process in NaNO₃-electrolytes indicates the development of a highly heterogeneous film which is still attached to the specimen surface. The very porous surface film structure is shown in the scanning electron micrograph in Fig. 4.6.

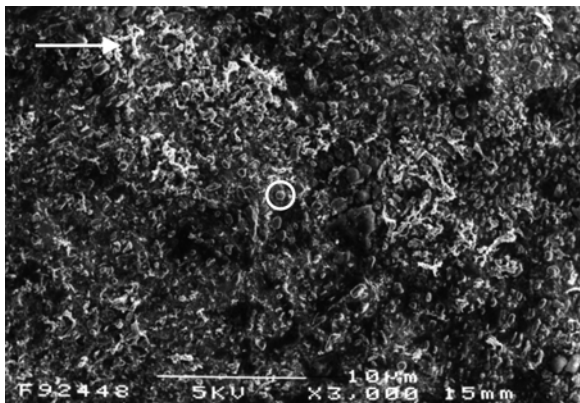


Fig. 4.6: Scanning electron micrograph of 100Cr6 surface after ECM in flow channel. Current density: 20 A/cm², 40 s, average flow velocity: 7 m/s, NaNO₃ (20%). One single globular carbide is marked with white circle. Flow direction is given upper left (white arrow).

4.4 Discussion

On the basis of the experimental data presented and discussed in Section 4.3 qualitative models for the electrochemical metal dissolution in NaCl and NaNO₃ can be proposed.

The basic principle of anodic metal dissolution using concentrated NaCl-electrolyte is given in Fig. 4.7.

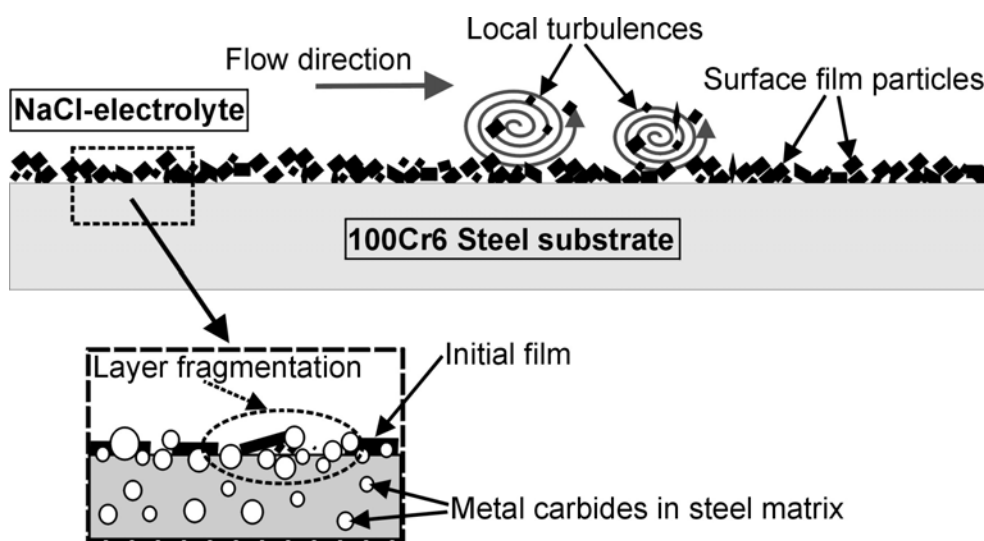


Fig. 4.7: Basic principle of anodic metal dissolution using NaCl-electrolytes. The loosely bound particles of 100Cr6 surface film (black) can be removed by local turbulences in the flowing electrolyte. M₃C-carbides from the steel matrix (white) accumulate in the film.

An air-formed, very thin and compact initial film is assumed to exist on the steel substrate before the ECM-experiment. At the beginning of current flow the initial film is quickly broken up by localized attacks of chloride-ions and does not have any further effect on the ECM-process. Local turbulences in the flowing electrolyte intensify the removal of carbides and reaction products from the specimen surface by mechanical stress. In the steady state, a solid oxy-chloride film with Fe²⁺ may be formed. This salt film can easily be dissolved, but it is strong enough to bind the carbides weakly to the surface. At a cylinder electrode without rotation, a yellow film of dissolving Fe-species slowly slips down due to its high density. The yellow colour could be caused by small amounts of Fe³⁺-species in this film. At high rotation speeds, this yellow product leaves the surface and vanishes completely. The

diffusion of Fe^{2+} -ions through the salt film must be fast, since R_{film} is small or negligible. Loosely bound, inert M_3C -particles originating from the steel matrix accumulate in the surface film on the 100Cr6 substrate, developing the carbon-rich surface layer described in Section 4.3. The permanent attack of chloride-ions on the carbon-rich 100Cr6 surface film in combination with the turbulent electrolyte flow is considered to be the main reason for the very weak film adhesion.

Nitrate-ions are passivating in the ECM-process under the conditions of Fig. 4.2b [54]. The initial, air-formed film on the 100Cr6 substrate stays compact and apparently no film destruction takes place at the beginning of the ECM-experiment. Up to current densities of 9 A/cm^2 no metal dissolution is possible assuming a compact, permanently growing oxide-film on the specimen surface. The components forming this thin oxide-film can not be removed by the turbulent electrolyte flow and as the result no Fe^{n+} -diffusion through this surface layer is possible and a current efficiency of $\sim 0 \%$ is observed (see Section 4.3). The film resistance exceeds that of the film formed in NaCl. At current densities $>10 \text{ A/cm}^2$ the morphology of this surface film changes (see Fig. 4.6). As shown in the qualitative model (Fig. 4.8) the strongly attached, solid surface layer on the 100Cr6 steel substrate gets very porous corresponding to increasing current efficiencies. Oxides still can be observed in the surface film and basically an enrichment of carbide particles is found. Metal dissolution is observed at current densities $>10 \text{ A/cm}^2$ by dissolution of Fe^{3+} . The porosity of the surface film indicates the presence of local Fe^{3+} -diffusion microchannels in the solid surface film. Special locations on the steel substrate like non-metallic inclusion compounds, metal carbides or grain boundaries may be discussed to be the origin of local break-throughs in the 100Cr6 anodic surface film because of imperfections of the initial film. The removal of solid surface film components like oxides, carbides or salt precipitations from the specimen surface is based on the transport process by local turbulences in the flowing electrolyte. Compared to the NaCl-system this transport process of solid particles in NaNO_3 is strongly hindered because the adhesion of the surface film formed in NaNO_3 is much stronger.

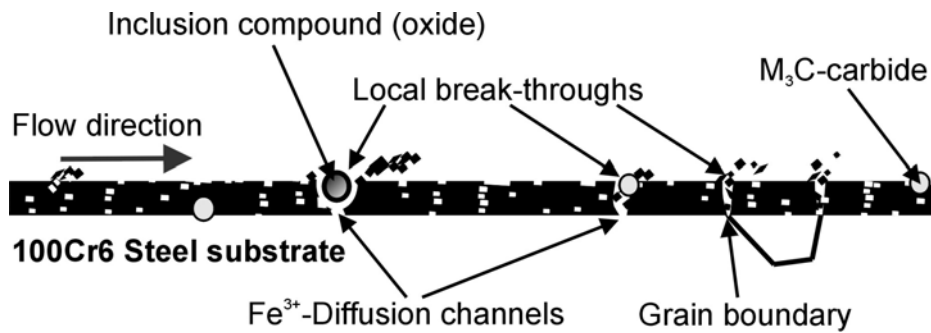


Fig. 4.8: Basic principle of anodic metal dissolution using NaNO_3 -electrolytes. The 100Cr6 anodic surface film (black) is strongly attached to the specimen. The porosity of this film is indicated by holes in the film structure (white).

To our knowledge, this is the first time that the difference between the surface film formed by loosely bound carbide particles in NaCl solution and the strongly bound, carbide-rich layer obtained by using NaNO_3 electrolyte was detected. In NaCl , a preferential etching at boundaries between Fe and carbide grains may be speculated. On the other hand, the enrichment of carbide particles in NaNO_3 indicates that the passive film does not allow a preferential removal of carbides. It should be emphasized, that this reasonable speculation has to be proved by independent measurements.

4.5 Conclusions

1. For ECM applied in microsystem technologies, substrate heterogeneities have to be avoided. During the high rate anodic metal dissolution of steel 100Cr6, a solid carbon-rich surface film is built up. This film is loosely bound, if concentrated NaCl -solutions are used, but it is strongly attached to steel in NaNO_3 -electrolytes.
2. The choice of electrolyte (NaCl or NaNO_3) strongly influences the electrochemical behaviour regarding the current efficiency and the anodic polarization curves. Active dissolution of Fe^{2+} occurs in NaCl at potentials > 0 V, whereas transpassive dissolution of Fe^{3+} (>10 A/cm²) as well as oxygen evolution (at lower i) occurs in NaNO_3 at potentials > 1.8 V.
3. Measurements at the rotating cylinder electrode show a strong influence of rotation speed in NaCl , but no influence in NaNO_3 .

4. The polarization resistance R_p is mainly due to the electrolyte resistance in NaCl. In NaNO_3 , on the other hand, the film resistance contributes, too.
5. The surface morphology using NaCl indicates a blank specimen microstructure with strong dependence on hydrodynamic conditions when using the rotating cylinder electrode. The use of NaNO_3 -electrolytes leads to a rough microstructure.
6. The metal dissolution process in NaCl may be controlled by a relatively easy diffusion of Fe^{2+} -ions through a loosely bound, solid surface film directly at the specimen surface to the flowing electrolyte. This film consists of two parts: an inner film of undissolved carbide particles originating from the steel matrix and an outer film formed by salt precipitation from the electrolyte. Most particles of the surface film are removed in solid state by the turbulent flow. In NaNO_3 -electrolytes a strongly attached surface film formed by carbides and oxides hinders the Fe^{n+} -diffusion. A Fe^{3+} -dissolution mechanism is only possible when the surface film gets a very porous microstructure ($>10 \text{ A/cm}^2$). The removal of surface film particles is carried out basically in the solid state.

Chapter 5

On the influence of microstructure and carbide content of steels on the electrochemical dissolution process in aqueous NaCl-electrolytes

Thomas Haisch, Eric Jan Mittemeijer and Joachim Walter Schultze

Abstract

The electrochemical dissolution behaviour of armco-iron and of the steels C15, C45, C60 and 100Cr6 in concentrated sodium chloride media has been investigated. Anodic metal dissolution experiments have been carried out using the flow channel cell (parallel plate reactor), the rotating cylinder electrode (RCE) and the capillary cell. The microstructure of the steel has been varied through variation of carbon content and heat treatment (e.g. soft annealed with globular carbides or pearlitic). Current-efficiency values have been obtained by gravimetric measurements in the current-density range from $i = 5$ to 60 A/cm^2 . For the soft annealed steels, the divalent ferrite dissolution in combination with electroless cementite removal dominates. For the pearlitic steels, the occurrence of oxygen evolution at electronically conductive metal carbides or trivalent ferrite dissolution, depending on the current density applied, was detected. Microstructure dependent potentiostatic current transients and potentiodynamic polarization curves have been presented. Polarization resistances, R_{pol} , were measured in dependence on NaCl concentration and the applied anode potential. For pearlitic steels (with carbon contents $\geq 0.45 \%$) R_{pol} exceeds that of the analogous soft annealed steels. The topographies of the steel surfaces after anodic dissolution show microscopic structures, based on inert metal carbides, which are the result of preferential ferrite dissolution. Qualitative metal dissolution models explain the electrochemical dissolution behaviour of soft annealed and pearlitic steels on the basis of the formation of solid films at the substrate surfaces and recognizing the role of the inert metal carbides in the steel matrix. In these models, the role of a polishing layer forming between the solid particles has been taken into account.

5.1 Introduction

The electrochemical metal dissolution applying high current densities and high electrolyte flow rates is characteristic for the process of Electrochemical Machining (ECM). A large range of pure metals, like iron, nickel, copper, aluminium and chromium, is suitable for application of this very fast electrochemical metal finishing process [16, 27, 51, 58, 64, 66-70]. In addition to pure metals or alloys, a lot of different steels have been used as anode materials and their dissolution behaviour has been described extensively [16, 65, 67-69, 71-73]. However, for most of the ECM-experiments carried out with steel specimens not much was known about the microstructure of the substrate used and / or its former heat treatment. In the case of electrochemical microsystem technologies, the microstructure of the substrate plays an important role [65, 72, 74]. For well defined surface microstructuring, the dimensions of the substrate heterogeneity and surface roughness should be much smaller than the structure itself. Actual Electrochemical Micro Machining (EMM) processes for shaver head fabrication, microjet production or hole drilling require reproducibilities of 5 μm and below. Due to that, knowledge about the local current densities, electrochemical and electroless reactions and the potential distribution at the steel substrate is required.

The present research was performed to investigate the drastic effect on the electrochemical metal-dissolution mechanisms of selected steel specimens in dependence on its microstructure. Microstructures as different as „soft annealed“, with globular carbides, and „pearlitic“, with lamellar carbides, were subject of investigation. Upon the electrochemical dissolution of steels the formation of a solid surface film and local inert barriers of cementite take place at the surface of the substrate [16, 58, 72-74]. This causes a new phenomenon: the time dependence of the polishing film. The role of the surface structure in association with the effect of the microstructure of the substrate will be taken into account in the proposed metal-dissolution models for the steels investigated.

5.2 Experimental procedure

5.2.1 Specimen preparation; Metallography

Steel specimens were commercially obtained (rod material); for composition of the steels, see Table 5.1.

Table 5.1: Chemical compositions of examined ECM-substrates (in weight percent).

	C	Cr	Si	Mn	Ni	P	S	Fe
armco-iron	~ 0	~ 0	~ 0	~ 0	~ 0	~ 0	~ 0	99.99
C15	0.15	~ 0	0.31	0.45	~ 0	0.044	0.045	99.15
C45	0.45	0.11	0.31	0.61	0.15	0.042	0.041	98.28
C60	0.60	0.37	0.39	0.72	0.23	0.039	0.038	98.21
100Cr6	0.97	1.43	0.28	0.28	0.11	0.006	0.002	96.91

For the electrochemical dissolution experiments in the flow channel cell, specimens of dimensions 1 cm x 1 cm x 1.5 cm (area, subjected to the electrolyte: 1 cm²) were cut out of the centre of the rod. The surfaces of the specimens were ground and polished mechanically. For the experiments with the rotating cylinder electrode massive rings (12 mm diameter, 1 mm height and 0.38 cm² lateral electrode area) were cut out of the steel rods.

Microsections for light microscopic investigation were prepared by mechanical grinding and polishing. Thereafter etching was performed using a 2% solution of nitric acid in amyl alcohol (nital). The duration of the etching process was 30 seconds.

For all annealing experiments performed in this work the specimens were put in capsules of silica glass containing pure argon at 50 kPa (at room temperature) as protective gas. The heat treatments of the steels were carried out in a muffle furnace.

The steels C15, C45 and C60 were soft annealed according to the heat treatment scheme (a):

(a) 690°C (170 hours) - air cooling.

Using the phase diagram data of the steel 100Cr6 [46], a somewhat higher soft annealing temperature was chosen in this case:

(b) 730°C (170 hours) - air cooling.

The pearlitic microstructures (of the steels C15, C45 and C60) were established using the following heat treatment:

(c) 900°C (2 hours) - cooling down to 600°C (cooling rate: 100°C per hour) - air cooling.

For the steel 100Cr6 a dedicated heat treatment was chosen to obtain a pearlitic microstructure (d):

(d) 1050°C (1 hour) - cooling down to 600°C (cooling rate: 100°C per hour) - air cooling.

5.2.2 Galvanostatic metal dissolution experiments; flow channel cell

The electrochemical dissolution experiments were carried out in a rectangular flow channel (often called parallel plate reactor), which has been described elsewhere [51, 65]. The average electrolyte flow velocity was set at 7 m/s implying turbulent flow conditions within the reactor. Platinized copper / tungsten alloy was used as cathode material. Armco-iron, C15, C45, C60 and 100Cr6 steel specimens with well defined microstructures served as anodes. The distance between cathode and anode (often called working gap) was set at 2 mm at the start of the experiment. An aqueous NaCl solution (20 wt. %) at 40°C ± 1°C, pH 7, served as electrolyte for electrochemical metal dissolution. All experiments were carried out under galvanostatic conditions with average current densities from 5 to 60 A/cm². Direct current was selected using a GOSSEN SSP rectifier with 3000 W output. The specimens were subjected to the electrochemical dissolution for 20 to 60 seconds. Then they were removed quickly from the reactor and washed with distilled water. The timelag between the experiment and the washing procedure was about 15 seconds because of experimental setup reasons.

5.2.3 Potentiostatic experiments; rotating cylinder electrode (RCE)

All potentiostatic current transients were measured using an EG&G 273A potentiostat. An anode potential of + 0.75 V (vs. NHE) was applied and the transferred charge, Q , was detected. The selection of the applied anode potential was based on anodic polarization curves discussed elsewhere [72]. Passivation effects can be observed at this anode potential. With a view to the determination of

current efficiencies described in Section 5.2.5, oxygen evolution at the anode surface can be excluded as side reaction at the selected anode potential. A platinum net served as counter electrode (CE), armco-iron, C15, C45, C60 and 100Cr6 steel specimens were used as working electrodes (WE) at a rotation speed of 190 rpm. A commercially obtained Ag/AgCl-electrode served as reference electrode (RE). The distance between the working electrode and the counter electrode was set at 10 mm. An aqueous NaCl solution (20 wt. %) at $25^{\circ}\text{C} \pm 1^{\circ}\text{C}$, pH 7, served as electrolyte. The duration of the transient measurement was set at 360 seconds.

5.2.4 Potentiodynamic experiments; rotating cylinder electrode (RCE); capillary cell

For RCE-experiments, a potential scan rate of 40 mV/s and anode rotation speeds of 590 and 1390 rpm (turbulent conditions) were applied. 1 potential cycle („forward scan“ and „reverse scan“) has been chosen. All other experimental parameters were the same as described in Section 5.2.3.

For the experiments with the capillary cell a setup was used which has been described elsewhere [75]. The electrolyte in the capillary was not moved and the „open area“ of the capillary was $9 \times 10^{-4} \text{ cm}^2$. The cementite (Fe_3C) substrate investigated (see Section 5.3.5) was prepared from commercially obtained cementite powder by pressing and sintering (at 700°C during 1 day).

5.2.5 Current efficiencies

The current efficiencies for metal dissolution were determined by anode mass-loss measurements on the basis of divalent metal ion formation according to (standard potential of reaction (5.1a): -0.44 V):

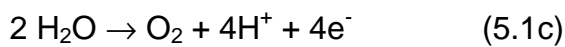


Metal carbides and inclusion compounds in the steel matrix were assumed to be inert, i.e. not dissolving electrochemically upon Electrochemical Machining.

A theoretical value for the mass loss of ferrite, ΔW_{theo} , can be obtained from [16, 51]:

$$\Delta W_{theo} = \frac{M I t}{n F} = \frac{M Q}{n F} \quad (5.2)$$

where M is the atomic mass of iron, I is the applied current, t is the dissolution time, F is the Faraday constant and Q is the transferred total charge. The valence of dissolution, n , was taken as 2 (cf. Eq. (5.1a)). If other electrochemical anodic reactions (different from Fe^{2+} formation) occur during the ECM process, the current efficiency with respect to ferrite dissolution is lower than 100 %. Such reactions can be the trivalent iron dissolution or oxygen evolution (standard potentials of reaction (5.1b): -0.04 V and reaction (5.1c): +1.23 V (at pH 0), +0.81 V (at pH 7):



Before measurement of the experimental mass loss of the specimens, ΔW_{exp} , solid particles, with enhanced occurrence at the substrate surface upon the electrochemical dissolution, were removed completely from the specimen surface by washing with distilled water. The current efficiency η was then calculated according to:

$$\eta = \frac{\Delta W_{exp}}{\Delta W_{theo}} \quad (5.3)$$

In case of reaction (5.1b), the current efficiency η will be 67% (and 0% for pure reaction (5.1c)). While a current efficiency $100\% > \eta > 67\%$ indicates an undefined contribution of reactions (5.1b,c) to (5.1a), $\eta < 67\%$ gives evidence for contributions of reaction (5.1c) to an undefined combination of reactions (5.1a,b).

Due to the additional mass loss by the removal of inert carbides, ΔW_{exp} in equation (5.3) can be expressed as follows:

$$\Delta W_{exp} = \Delta W_{ferrite} + \Delta W_{carbide} \quad (5.3a)$$

In equation (5.3a) $\Delta W_{ferrite}$ is the mass loss caused by the electrochemical ferrite dissolution and $\Delta W_{carbide}$ the mass loss due to the simple electroless erosion of not dissolving carbides. Since $\Delta W_{carbide}$ is a function of the carbide (M_3C) content of the steels, the maximal current efficiency, η_{max} , can be calculated with the help of the data presented in Table 5.1 ($\eta_{max} = 102.29\%$ (C15); 107.21% (C45); 109.85% (C60); 117.60% (100Cr6)).

5.2.6 Topographic changes

Metal removal rates under ECM-conditions can be calculated from equation (5.2): if a constant current density $i = 1 \text{ A/cm}^2$, a dissolution valence $n = 2$ and a current efficiency $\eta = 100\%$ are assumed, the removal rate of pure iron would be 0.2894 mg/s (or 0.2894 mg/C). With respect to a surface area of 1 cm^2 the thickness change Δd , of the substrate would be $0.368 \text{ }\mu\text{m/s}$ (or $0.368 \text{ }\mu\text{m/C}$).

In case of potentiodynamic or potentiostatic transient measurements (see Section 5.3.4), the transferred charge, Q , was calculated as the area under the recorded current transient curve:

$$Q = \int I dt \quad (5.4)$$

These values are important for the estimation of topographic changes. For example, for galvanostatic experiments with $i = 10 \text{ A/cm}^2$ and $t = 60 \text{ s}$, we obtain $\Delta d \approx 221 \text{ }\mu\text{m}$, i.e. the electrode distance increases by 11% (recognizing the geometry of the flow channel; see Section 5.2.1). On the other hand, for potentiostatic experiments at the RCE we obtain $\Delta d \approx 18 \text{ }\mu\text{m}$ with $i = 0.5 \text{ A/cm}^2$ and $t = 100 \text{ s}$. This means that the diffusion layer at the edge of the thin film electrode will increase, and the influence of eddies decreases.

Finally, the formation of a saturated FeCl_2 -film of $10 \text{ }\mu\text{m}$ thickness will require a charge of at least 2 C/cm^2 . The formation of protruding carbide lamellas with a length of $20 \text{ }\mu\text{m}$ will require a charge flow of at least 40 C/cm^2 . Thus, beginning from $q = 0 \text{ C/cm}^2$, the topography and the structure of the interface will change continuously.

5.3 Results and Discussion

5.3.1 Microstructure of the steel substrates

Cross-sections of the specimens which were heat treated according to the procedures given in Section 5.2.1 are shown in Figs. 5.1 - 5.5.

The microstructure of the armco-iron as received is shown in Fig. 5.1. Some typical non-metallic inclusions of MnS ($\varnothing \leq 1 \text{ }\mu\text{m}$) appear as black spots in the largely equiaxed ferrite grains shown in the cross-section. The average ferrite grain size is

about 25 μm . Microstructure modification of the armco-iron substrate was not performed: the minor amount of carbon (< 0.01 wt. %) is completely dissolved in the α -iron matrix.

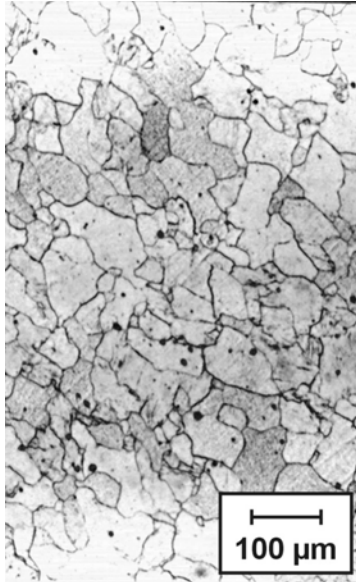


Fig. 5.1: Optical micrograph (bright field) of a cross-section (nital etched) of armco-iron. The grain boundaries (dark lines) and some MnS-inclusions (dark spots) can be observed.

The hypoferritic and pearlitic microstructures of the steels C15, C45, C60 and 100Cr6 are exhibited in Figs. 5.2a, 5.3a, 5.4a and 5.5a. The regions where lamellar carbides (cementite of the composition Fe_3C (steels C15, C45 and C60) or M_3C (steel 100Cr6)) are observed appear black after etching with nital in the light optical micrographs if the lamellar structure is very fine. Obviously, the amount of pearlite depends on the carbon content (area percentages of pearlite grains in cross-sections analysed: C15, 19%; C45, 56%; C60, 75%; 100Cr6, 100% [44]). Typical diameters of the pearlite grains are 15 μm (for C15) up to 40 μm (for 100Cr6). The geometry, orientation and the extent of the lamellar carbides in the ferrite matrix vary, of course, when considering different grains; typical values for the lateral size and thickness of a single carbide lamella are 10 - 20 μm and 0.1 - 0.3 μm (see Fig. 5.5a (thickness) and 10a (lateral size)). The distance between the lamellar carbides (which is filled with ferrite) is about 0.1 - 0.8 μm .

The soft annealed states of the steel substrates are represented by the cross-sections shown in Figs. 5.2b, 5.3b, 5.4b and 5.5b. Clearly, the soft annealing has caused partial (Fig. 5.3b) or complete (Fig. 5.5b) breaking up of the lamellar pearlite structure. The (globular) carbides of the composition Fe_3C (for the steels C15, C45 and C60) and M_3C (for the steel 100Cr6) appear dark after etching with nital in the

light optical micrographs. The M_3C globules are exclusively located in former pearlite grains. The average diameter of the observed globular carbides is smaller than $1\ \mu\text{m}$. The average ferrite grain sizes vary in the range of $10 - 30\ \mu\text{m}$.

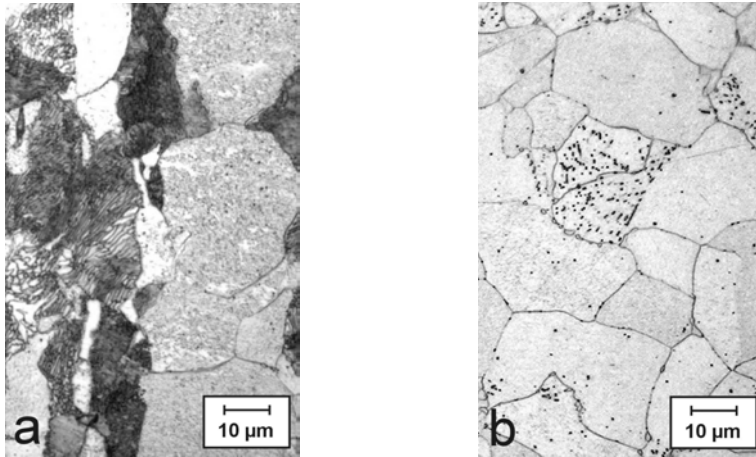


Fig. 5.2: Optical micrographs (bright field) of cross-sections (nital etched) of the steel C15 **(a)** pearlitic microstructure; colonies of cementite lamellas can be observed **(b)** soft annealed microstructure; dark spots are carbides.

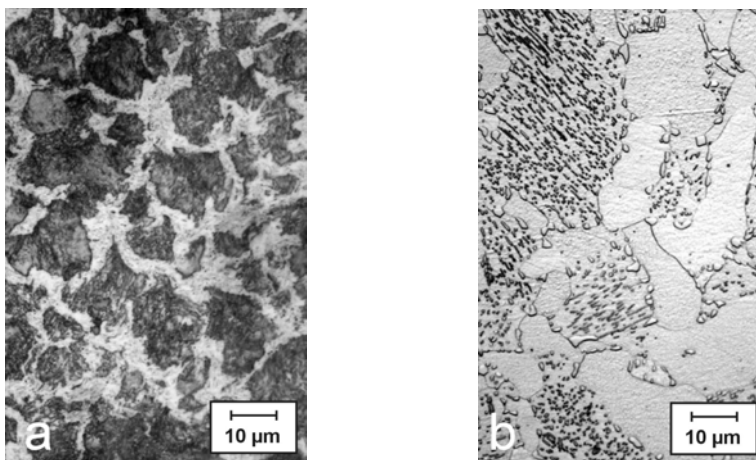


Fig. 5.3: Optical micrographs (bright field) of cross-sections (nital etched) of the steel C45 **(a)** pearlitic microstructure **(b)** soft annealed microstructure.

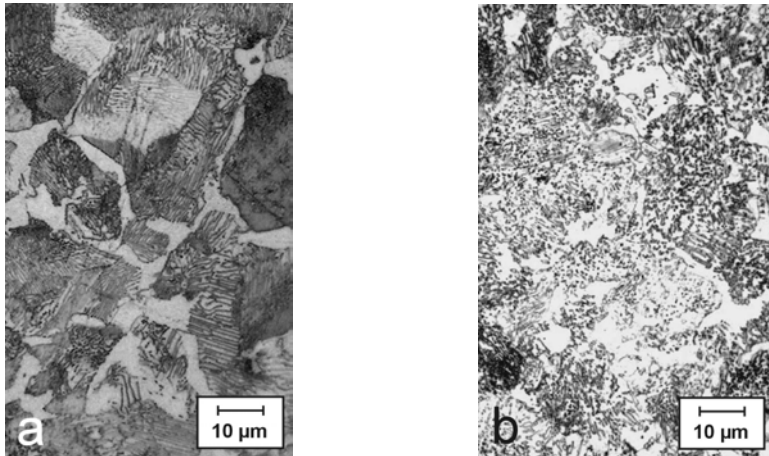


Fig. 5.4: Optical micrographs (bright field) of cross-sections (nital etched) of the steel C60 **(a)** pearlitic microstructure **(b)** soft annealed microstructure.

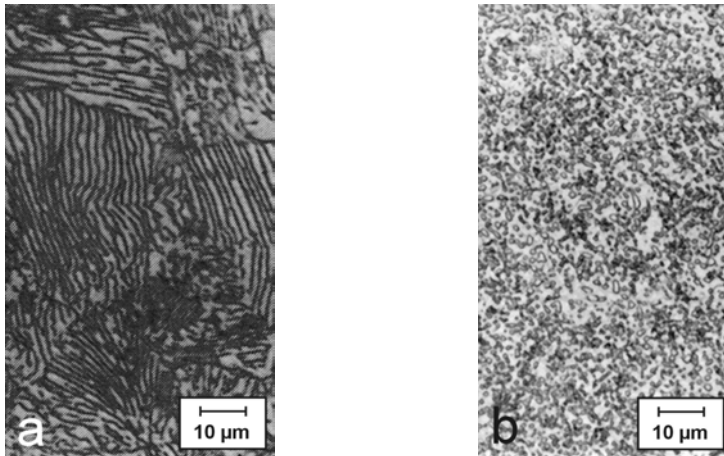


Fig. 5.5: Optical micrographs (bright field) of cross-sections (nital etched) of the steel 100Cr6 **(a)** pearlitic microstructure **(b)** soft annealed microstructure.

5.3.2 Surface film and boundary-layer formation upon Electrochemical Machining

The general formation of various (material dependent) anodic surface films upon high rate electrochemical metal dissolution has been discussed in particular in Refs. [20, 21, 59, 61, 73, 74]. Four specific types of surface films and boundary layers have to be distinguished going from the substrate surface towards the bulk of the electrolyte (see Fig. 5.11) [16, 51, 63, 76, 77]:

- B** the solid surface film (formed by metal oxides and carbides, originating from the steel matrix) [65];
- C** the very thin, solid salt layer (polishing layer) directly on the anode surface (built up by precipitation from the saturated electrolyte);
- D** the highly viscous diffusion layer of thickness δ_N (Nernst's layer);
- E** the laminar boundary layer in the flowing electrolyte of thickness δ_{Pr} (Prandtl's layer).

In the schematic presentation of this multilayer structure a soft annealed steel substrate (**A** in Fig. 5.11) containing small globular carbides is illustrated.

The anodic current density, i , for a mass transport controlled metal dissolution reaction is given by [16, 20, 51]:

$$i = nFD \frac{c_s - c_b}{\delta_N} \quad (5.5)$$

where D is the effective diffusion coefficient of the dissolving species (metal ion) in the diffusion layer, c_s is the concentration of the dissolving species directly at the specimen surface in the absence of the salt film, and c_b is the concentration in the bulk of the electrolyte ($c_b = 0$ in these experiments). The thickness of the diffusion layer, δ_N , is assumed to be constant along the anode surface (layer **D** in Fig. 5.11). When the metal ion concentration at the electrode surface reaches saturation with respect to the solubility product of the salt concerned, the precipitation of a thin, solid salt film (**C** in Fig. 5.11) occurs. For this case, equation (5.5) becomes:

$$i_{lim} = nFD \frac{c_{sat}}{\delta_N} \quad (5.6)$$

where c_{sat} is the saturation concentration of the metal ion taken up in the precipitating salt at the substrate surface and i_{lim} the limiting current density which can be observed when salt precipitation takes place. The thickness of the anodic diffusion layer δ_N depends on the hydrodynamic conditions prevailing in the electrolyte and can be calculated from:

$$\delta = \frac{L}{Sh} \quad (5.7)$$

where L is a characteristic length (here: the hydraulic diameter d_h) and Sh is the Sherwood number. The Sherwood number depends on the geometry of the used experimental setup; many empirical expressions for Sh have been proposed [16]. For

the turbulent flow conditions in flow channel cells, the following expression has been given [20]:

$$Sh = 0.22 Re^{7/8} Sc^{1/4} \quad (5.8)$$

where Re is the Reynolds number and Sc is the Schmidt number. The Reynolds number Re is defined as

$$Re = \frac{d_h u}{\nu} \quad (5.9)$$

and the Schmidt number as

$$Sc = \frac{\nu}{D} \quad (5.10)$$

where d_h is the hydraulic diameter, u is the average flow velocity, ν is the kinematic viscosity of the electrolyte and D is the effective diffusion coefficient (cf. Eq. (5.5)).

For the parameters of the galvanostatic flow channel experiments presented in this paper (see Section 5.2.2) the following values can be calculated from equations (5.6 - 5.10): Reynolds number $Re = 17194$, Schmidt number $Sc = 1596$, Sherwood number $Sh = 7066$, hydraulic diameter $d_h = 3.33$ mm, average thickness of the diffusion layer $\delta_N = 472$ nm (with $\nu = 1.357$ mm²/s, $D = 8.5 \times 10^{-6}$ cm²/s, $c_{sat} = 2.46$ mole/l [78]). The expected limiting current density i_{lim} , as calculated by equation (5.6), is 85.5 A/cm². This means, that all galvanostatic experiments presented in Section 5.3.3 were carried out in a current-density range below the limiting current density. It should be mentioned that the estimation given above is based on the traditional ion transport theories for excess supporting electrolyte [16, 20, 51]. At ECM conditions, however, migration is dominant, and the diffusion coefficients of saturated solution will be smaller than for infinite dilution [79].

It was found that for steel specimens the solid surface film **B** plays a dominant role for the resulting surface finish upon ECM [60, 65, 72, 80]. On all steel substrates investigated in this work black solid surface films developed which were not strongly attached to the specimen surfaces when using NaCl-electrolytes [65]. In particular, in the case of the soft annealed substrates a very easy removal of surface film (particles) was possible, by applying a simple washing procedure with distilled water. After the washing procedure, the substrate surface appeared bright, macroscopically flat and no pittings were observed. In the case of the pearlitic steel substrates the solid surface films appeared to stick better to the substrate. Surface film removal by

the washing procedure was still possible, but the surface observed after film removal was grey and local pittings occurred.

The average thickness of the solid surface film **B**, which is composed by a couple of carbide and oxide particles, can be estimated by considering the typical extent of the film constituents. Assuming that for the soft annealed condition of the steels (globular carbides with average diameter $\leq 1 \mu\text{m}$) 1 - 4 monolayers of single carbide particles (surrounded by oxides) are built up at the substrate surface, the expected thickness of the solid surface film for the *soft annealed* condition can be $3 \mu\text{m}$ (see Section 5.3.1). The carbides observed in the pearlitic steel structures have a lamellar shape with lateral extents of 10-15 μm . Due to diverse orientations of these lamellas with respect to the surface, according to the grain structure of the steel, it is assumed that all possible carbide orientations within the solid surface film occur. Due to the large lateral size of the lamellar carbides the average thickness of the solid surface film for the *pearlitic* condition may easily reach 15-20 μm .

In the metal dissolution experiments with armco-iron no macroscopically visible surface film formed on the substrate.

5.3.3 Current efficiencies for the flow channel experiments

With increasing current density (anode potential), the additional formation of Fe^{3+} or O_2 becomes possible (see Section 5.2.5). Due to microscopical heterogeneities of the steel substrate and the polishing layer (see Section 5.3.2), local shifts of the anode potential may occur. Therefore, current efficiency measurements have great importance for the detection of the electrochemical conditions at the substrate / electrolyte interface.

The measured current efficiencies obtained by applying different current densities in comparison with the calculated maxima are shown in Fig. 5.6. These results were calculated from the measured mass losses according to Section 5.2.5. For the calculated possible maxima the contribution of the inert carbides to the mass loss, $\Delta W_{\text{carbide}}$, is incorporated in the calculation of the current efficiency; cf. Eqs. (5.3) and (5.3a).

The results of the metal dissolution experiments for armco-iron and C15 (soft annealed and pearlitic) substrates are presented in Fig. 5.6a. These results indicate

that for all substrates the divalent iron dissolution mechanism dominates (cf. Eq. (5.1a)).

For armco-iron, the experimental values fit very well with the calculated ones, implying that chemical iron dissolution or simple erosion of undissolved iron grains do not take place.

The highest current efficiencies for the soft annealed C15 substrate were observed at current densities of 10-30 A/cm². Because the current efficiency in this current-density range is close to the calculated maximal value (see above), this suggests a mass loss contribution due to the erosion of inert Fe₃C carbides. The current efficiencies for the pearlitic C15 specimens are slightly smaller than for the soft annealed C15 at all current densities applied; this suggests the occurrence of electrochemical side reactions different from the divalent iron dissolution. Since gas evolution was not observed at the substrate surfaces, a small amount of trivalent iron dissolution could have occurred (see Section 5.2.5).

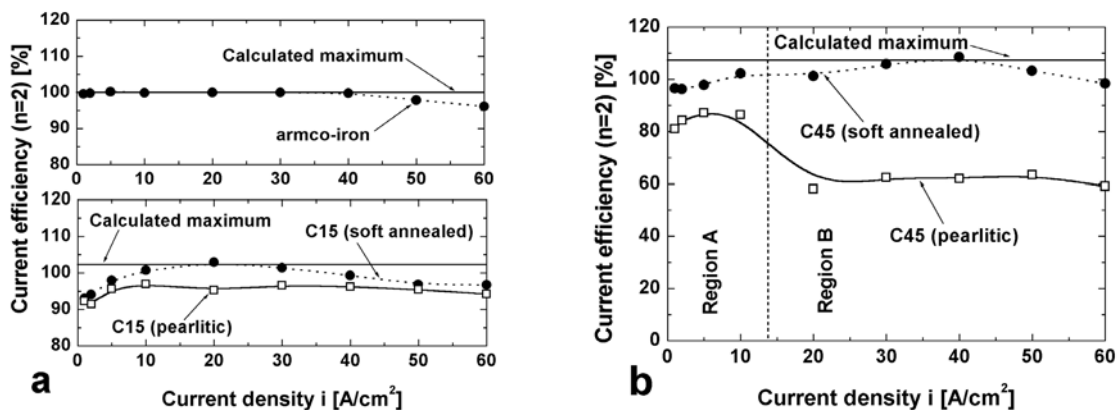
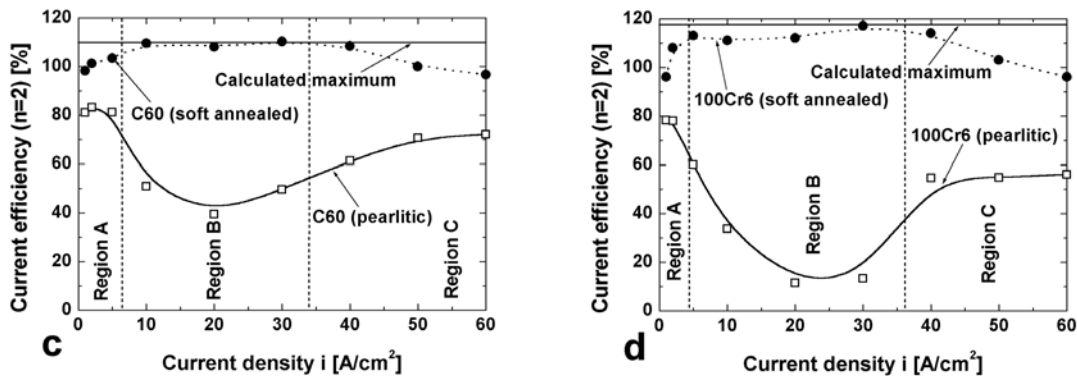


Fig. 5.6: Current efficiencies on the basis of an assumed divalent iron dissolution mechanism obtained by galvanostatic experiments in the flow channel cell. Electrolyte: NaCl (20 wt. %); average flow velocity: 7 m/s; electrolyte temperature at channel inlet: 40°C; distance between anode and cathode: 2 mm.

- (a) armco-iron and C15 (soft annealed and pearlitic)
- (b) C45 (soft annealed and pearlitic)
- (c) C60 (soft annealed and pearlitic)
- (d) 100Cr6 (soft annealed and pearlitic)



Obviously, the current efficiencies as function of the applied current density for the soft annealed steel specimens C45, C60 and 100Cr6 express a dissolution behaviour, which is in line with the results obtained for the soft annealed C15 substrate (see Figs. 5.6b-d):

- The experimental maxima of the current efficiencies in the current-density range $30 < i < 40 A/cm^2$, do not exceed but are close to the calculated values.
- At lower current densities ($i < 10 A/cm^2$) and higher current densities ($i > 50 A/cm^2$) small amounts of side reactions must occur, because the observed current efficiencies are lower than calculated. The absence of visible gas evolution suggests the formation of trivalent iron species.

It can be concluded that the influence of the carbon content of soft annealed steels on the ECM process can be largely understood recognizing that an increasing amount of carbide particles is eroded away in correspondence with increasing the carbon content of the steel. Hence, the electrochemical metal dissolution mechanism is based on the „armco-behaviour“, apart from the observed side reactions.

A clear effect of the substrate microstructure becomes apparent, upon considering the results for the pearlitic substrates (C45, C60 and 100Cr6; see Figs. 5.6b-d):

- In the entire current-density range examined, the current efficiencies are significantly lower than the theoretically calculated maximal values. Therefore, massive contributions due to non-ferrite-dissolving reactions (oxygen evolution, Fe^{3+} formation, see Section 5.2.5) occur.
- The current efficiency minimum occurs at about $20 A/cm^2$ for all substrates and becomes more pronounced with increasing carbon content. Since $\eta < 67\%$ in the minimum, oxygen evolution takes place with partial current

densities $i_{O_2} > 5 \text{ A/cm}^2$. This causes an appreciable decrease of pH to 0 or even $\text{pH} < 0$ [79]. That means, that the local potential at oxygen evolving sites will exceed 1.2 V. This can be expected on top of cementite lamellas not covered by the polishing film.

e) At low current densities ($i < 5 \text{ A/cm}^2$) a current efficiency maximum is observed. This maximum shifts to lower values of the current density when the carbon content is increased.

Based on these observations, diverse current density regions are distinguished for the pearlitic steels ($C \geq 0.45 \text{ wt. \%}$). In region A, relatively high current efficiencies are found (80-90%), indicating a dominant divalent iron dissolution and small amounts of electrochemical side reactions (see Figs. 5.6b-d). In the transition from region A to B the current efficiency decreases drastically and the local minimum is reached in region B. In the case of the pearlitic steels C60 and 100Cr6 severe gas evolution at the anode (substrate) surface was clearly visible. For all other substrates, gas evolution could not be observed because at the high electrolyte flow rates applied it was impossible to distinguish the evolution of gas bubbles from the formation of the solid, muddy reaction products „deposited“ at the substrate surface. A region C can be indicated for the pearlitic steels C60 and 100Cr6, where the current efficiency increases again. This may be interpreted as that the reaction mechanism changes from dominating O_2 evolution to trivalent iron dissolution.

The current efficiency of pearlitic steels is plotted as function of the mole fraction X_{Fe_3C} in Fig. 5.7, for the occurring maxima and minima in the current efficiency vs. current density curves. Approximately linear behaviours are observed. These results are compatible with the given discussion: iron dissolution occurs exclusively at the ferrite / electrolyte interface, electronically conductive cementite is inert and oxygen evolution is restricted to the Fe_3C / electrolyte interface.

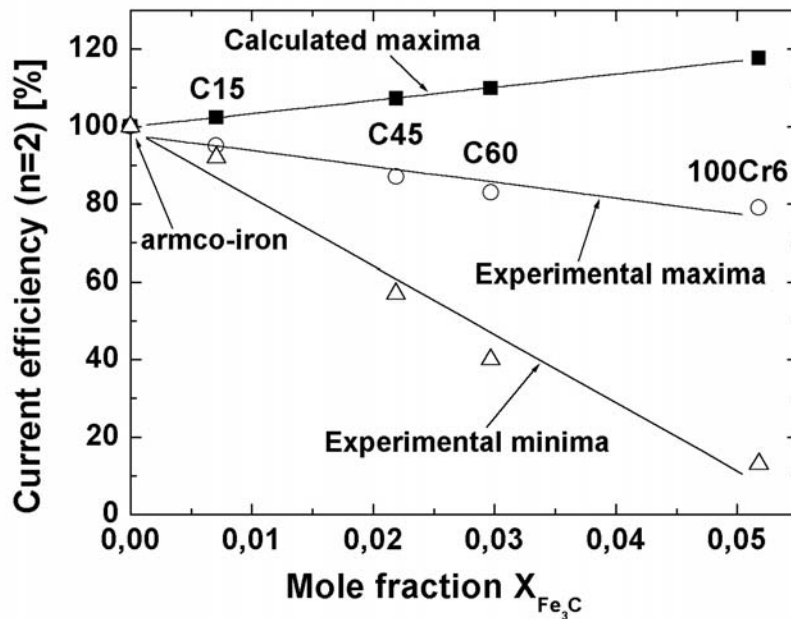


Fig. 5.7: Experimental current efficiencies of pearlitic steel substrates and armco-iron: The given experimental minima pertain to a current density $i = 20 \text{ A/cm}^2$. The experimental maxima pertain to a current density $i \leq 10 \text{ A/cm}^2$.

5.3.4 Potentiostatic current transients recorded with rotating cylinder electrode

The potentiostatic dissolution experiments were carried out using the rotating cylinder electrode with parameter values given in Section 5.2.3. The values observed for the integral current efficiency, assuming a divalent iron dissolution mechanism, and for the transferred total charge have been gathered in Table 5.2.

Typical potentiostatic current transients observed with armco-iron and pearlitic steel substrates (anode materials) are shown in Fig. 5.8a. Analogous to the galvanostatic experiments performed with the flow channel cell, the current efficiency observed for armco-iron very closely equals 100% (see Table 5.2). During the first 60 seconds the recorded current decreases from about 650 mA at the start to about 540 mA, possibly due to the quick formation of a thin salt film (polishing layer) covering the whole specimen surface. This salt film might be very incoherent and non-protective: after a short period of time the current increases suggesting salt-film rupture. Subsequently the current decreases only very slowly and approximately

linearly at a rate of $-16 \text{ mA} / 60 \text{ s}$. It is suggested that this constant rate of decrease of current is caused by the topographic change of the electrode surface with decreasing influence of turbulence (see Section 5.2.6). These results indicate that armco-iron in concentrated NaCl solution can be considered as a non-passivating system, which dissolves according to reaction (5.1a) under the influence of aggressive and activating anions (e.g. chloride). The current transients obtained for the soft annealed steels (not shown in Fig. 5.8a) fit well to the armco-iron transient and therefore it is expected that the dissolution mechanism is exactly the same. This assumption is supported by the observation that the measured corresponding current efficiencies exceed 100% (see Table 5.2).

Table 5.2: Transferred charges, Q , and current efficiencies, η , of selected anode substrates, obtained by potentiostatic experiments with the rotating cylinder electrode (RCE).

Substrate	Transferred charge Q [C]	Current efficiency η [%] ($n = 2$)
armco-iron	194.2	100.1
C15 (soft annealed)	189.3	100.4
C15 (pearlitic)	185.1	100.0
C45 (soft annealed)	185.2	104.0
C45 (pearlitic)	98.3	100.9
C60 (soft annealed)	121.5	105.2
C60 (pearlitic)	86.6	101.0
100Cr6 (soft annealed)	189.1	112.4
100Cr6 (pearlitic)	88.6	109.5

Obviously, the dissolution mechanism for the pearlitic steel substrates (C15, C45, C60 and 100Cr6) changes upon increasing the carbon content. The (negative) slope of the current transients of the pearlitic substrates becomes larger with increasing carbon content; compare in particular the measured results of C15 and C45 in Fig. 5.8a. The effect of carbon content becomes negligible, when the carbon content of C60 is reached; the current transients of pearlitic C60 and 100Cr6 differ minimally. The values for the current efficiencies observed for the pearlitic steels indicate that small amounts of trivalent iron form upon ferrite dissolution, but the dominating reaction is still the formation of divalent species (oxygen evolution is impossible, see Section 5.2.3). It is proposed, that the distinct difference in the metal dissolution behaviour of soft annealed and pearlitic steels is caused by the resistance, R_{film} , of

the solid carbide (and oxide) film on the substrate surface, which depends on the microstructure of the steel substrate (see Sections 5.3.2 and 5.3.5).

It is already remarked here, that when the current transients of the pearlitic steel substrates are plotted reciprocally as a function of reaction time, an approximately linear dependence is observed (see Fig. 5.8b); for a possible explanation, see Section 5.4.3.

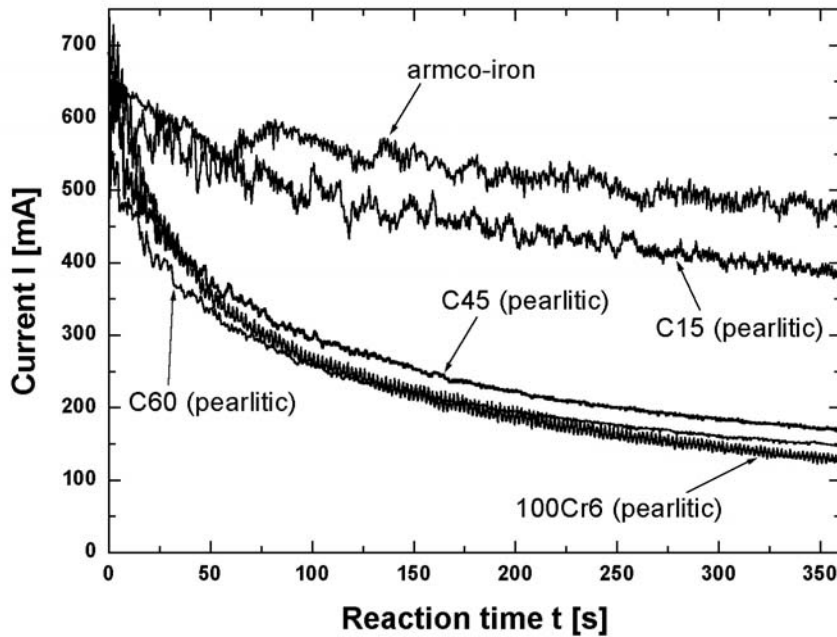


Fig. 5.8a: Current transients obtained by potentiostatic RCE-experiments with steel anodes. Electrolyte: NaCl (20 wt. %); anode potential: +0.75 V (vs. NHE); rotation speed of working electrode: 190 rpm; electrolyte temperature: 25°C; distance between working electrode and counter electrode: 10 mm; substrates: pearlitic C15, C45, C60, 100Cr6 and armco-iron.

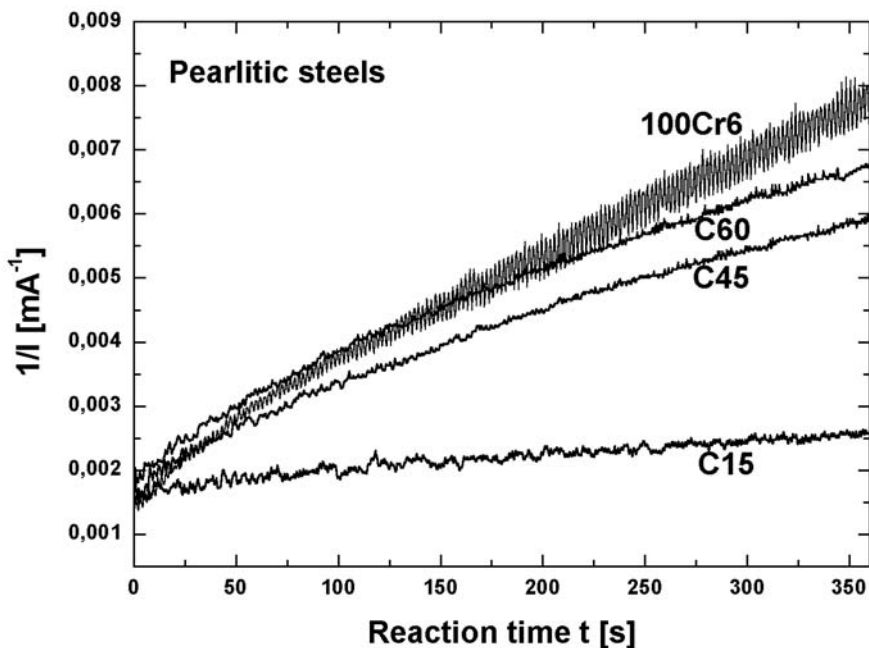


Fig. 5.8b: Reciprocal current as function of reaction time t for the pearlitic C15, C45, C60 and 100Cr6 steel substrates (see Fig. 5.8a).

5.3.5 Potentiodynamic experiments with rotating cylinder electrode

The potentiostatic experiments presented in Section 5.3.4 suggest that the formation of the solid surface film (cf. Section 5.3.2) strongly influences the polarization behaviour of steel substrates (see also Refs. [81-83]). A simple equivalent circuit can be proposed to describe the electrochemical properties of the ECM system with steel anodes (see Fig. 5.9a). The polarization resistance, $R_{pol} = dU / di$ (available from the slope of the polarization curve), is conceived as the sum of 3 single resistances:

$$R_{pol} = R_{film} + R_{polish} + R_{electrolyte} \quad (5.11)$$

with R_{pol} = polarization resistance, R_{film} = resistance of the solid carbide / oxide film, R_{polish} = resistance of the polishing layer ($Fe_xO_yCl_z$) and $R_{electrolyte}$ = resistance of the NaCl electrolyte (see Section 5.3.2).

The anodic polarization curves of the steel C45 (for both the soft annealed and pearlitic microstructures) are presented in Fig. 5.9a: for the soft annealed substrate, up to an anode potential of +1.3 V (vs. NHE) a linear polarization curve is observed ($R_{pol} \approx R_{electrolyte} = 0.31 \Omega cm^2$), then a „passive“ region (+1.3 to +1.8 V) occurs maybe

due to the formation of a thin, relatively compact polishing layer ($R_{pol} \approx R_{electrolyte} + R_{polish}$). This polishing layer possibly becomes incoherent at potentials $> +1.8V$ and the resistance of the polishing layer R_{polish} decreases (similar observations have been reported for other steels and iron-based alloys [16, 27, 72]). During the potentiodynamic measurement a solid carbide / oxide film, which gets thicker with increasing dissolution time t (increasing ferrite dissolution), may influence the polarization behaviour of the soft annealed substrate. Therefore, a small contribution of R_{film} and a slightly higher polarization resistance can be observed at the potential reverse scan ($R_{pol} \approx R_{film} + R_{electrolyte} = 0.35 \Omega\text{cm}^2$).

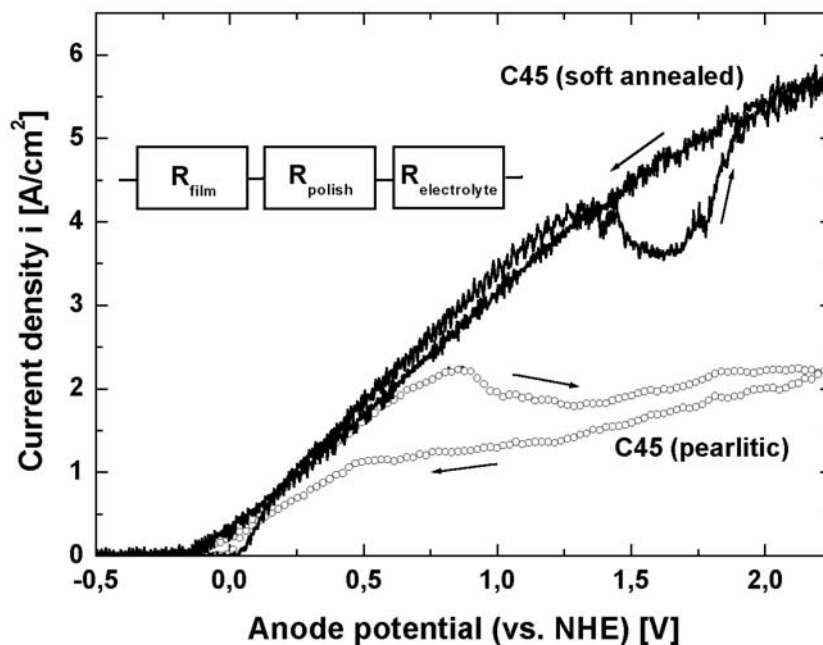


Fig. 5.9a: Potentiodynamic anodic polarization curves of the steel C45 for both the soft annealed microstructure and the pearlitic microstructure. RCE-experiments with an anode rotation speed of 1390 rpm were carried out. Scan rate: 40 mV/s; electrolyte: aqueous NaCl (20 wt. %); electrolyte temperature: 25°C; distance between working electrode and counter electrode: 10 mm. A simplified equivalent circuit for the ECM-system is given: $R_{pol} = R_{film} + R_{polish} + R_{electrolyte}$, with R_{pol} = polarization resistance, R_{film} = resistance of the carbide/oxide film, R_{polish} = resistance of the polishing layer and $R_{electrolyte}$ = resistance of the electrolyte.

For the pearlitic C45 substrate, much higher polarization resistances are observed due to the strong influence of R_{film} : from 0 V (vs. NHE) to +0.8 V an

approximately linear behaviour is observed, which should be based on the resistance of the electrolyte ($R_{pol} \approx R_{electrolyte} = 0.36 \Omega\text{cm}^2$). Then a significant limiting current region (+0.8 V to +2.3 V) follows with very strong contributions of R_{film} and R_{polish} ($R_{pol} \approx \infty$). The contributions of R_{film} and R_{polish} seem to remain very strong and at the end of the polarization experiment (in the range from +0.5 V to -0.1 V) a very high polarization resistance is observed ($R_{pol} = R_{film} + R_{polish} + R_{electrolyte} = 0.60 \Omega\text{cm}^2$; note that $R_{film} = f(t)$). With respect to the results obtained for the soft annealed condition, it must be emphasized that the value of R_{pol} has nearly doubled.

As discussed with Fig. 5.9a, the polarization resistance of steels at the beginning of ferrite dissolution depends largely on $R_{electrolyte}$. Hence, the electrolyte concentration should influence the observed polarization resistance in the lower potential range. Indeed, the anodic polarization curves of the soft annealed steel 100Cr6 given in Fig. 5.9b for various electrolyte concentrations (1-m, 3-m and 5-m NaCl) show that the activation potential, which correlates with the breaking up of the initial, air-formed oxide film on the substrate, shifts to lower values with increasing electrolyte concentration. Once the steel surface is activated by the adsorption of chloride-ions, the current density $i \approx 0 \text{ A/cm}^2$ is reached during the reverse scan at potentials which are about 200 mV lower than the original activation potentials. This is in good accordance with the theory of anodic anion activation proposed by Davydov [84-86]. The polarization resistances, R_{pol} , as determined from the slope in the linear region of the polarization curves (+0.1 V to +0.35 V), are: $R_{pol (1-m)} = 0.59 \Omega\text{cm}^2$; $R_{pol (3-m)} = 0.33 \Omega\text{cm}^2$; $R_{pol (5-m)} = 0.26 \Omega\text{cm}^2$. The comparison with the electrolyte conductivities ($\kappa_{NaCl (1-m)} = 0.096 \text{ S/cm}$; $\kappa_{NaCl (3-m)} = 0.187 \text{ S/cm}$; $\kappa_{NaCl (5-m)} = 0.235 \text{ S/cm}$) indicates the dominating contribution of $R_{electrolyte}$ (note that $\kappa_{NaCl (3-m)} / \kappa_{NaCl (1-m)} \approx R_{pol (1-m)} / R_{pol (3-m)}$ and $\kappa_{NaCl (5-m)} / \kappa_{NaCl (1-m)} \approx R_{pol (1-m)} / R_{pol (5-m)}$).

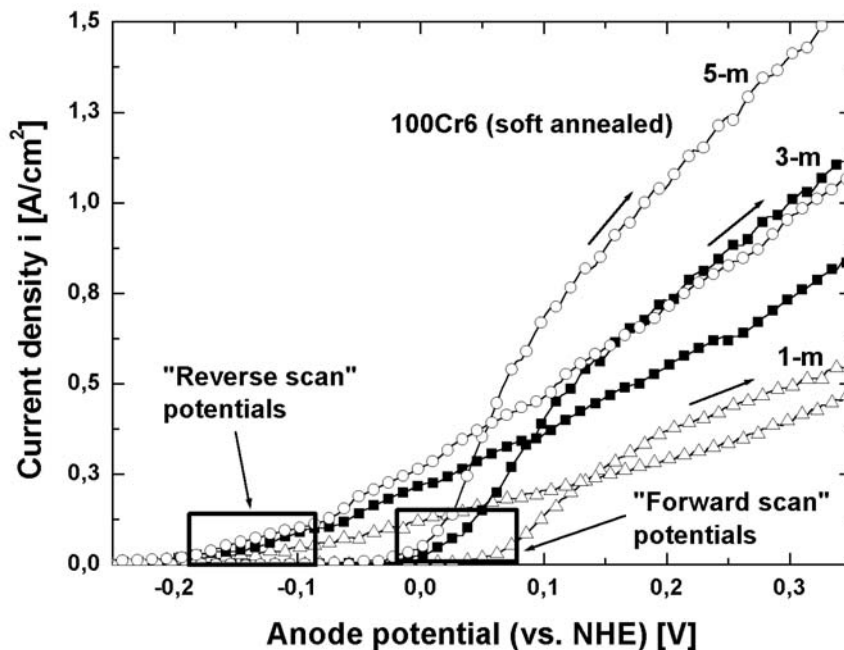


Fig. 5.9b: Effect of increasing concentrations of NaCl (1m, 3m, 5m) on potentiodynamic polarization curves of the soft annealed steel 100Cr6 (RCE-experiments with an anode rotation speed of 590 rpm). Scan rate: 40 mV/s; electrolyte temperature: 25°C; distance between working electrode and counter electrode: 10 mm. The „forward scan“ potentials (beginning of divalent Fe-dissolution) become lower with increasing electrolyte concentration. Once the surface is activated the „reverse scan“ potentials are about 200 mV lower than the „forward scan“ potentials.

5.3.6 Electrochemical behaviour of ferrite and cementite

The polarization curves shown in Fig. 5.9a represent the sum of all partial electrochemical reactions occurring at the steel surface (divalent and trivalent iron dissolution, oxygen evolution):

$$i = i_{\text{Fe}^{2+}} + i_{\text{Fe}^{3+}} + i_{\text{O}_2} \quad (5.12)$$

Therefore, detailed knowledge about the potential dependence of the separated reactions (current densities) is desired. The polarization curves obtained by experiments with the capillary cell for armco-iron dissolution and oxygen evolution at a cementite surface are presented in Fig. 5.9c. The anodic polarization curve of the armco-iron substrate is representative of exclusive Fe^{2+} formation which starts in the

active potential region. Since the carbon content of the substrate is negligible, the curve contains information about the polishing layer (layer **C** in Fig. 5.11).

Obviously, the inert cementite substrate does not dissolve, since the current densities are very small in the lower potential range ($i < 0.1 \text{ A/cm}^2$; 0 V to +0.9 V). Visual observations of the cementite surface after the anodic polarization experiment prove that no substrate was dissolved. At an anode potential of about +0.9 V (vs. NHE) the current density increases significantly due to oxygen evolution at the substrate surface, which is in good accordance with the standard potential of reaction (5.1c) (see Section 5.2.5). Therefore, the polarization curve represents the anodic electrochemical process (i_{O_2}) in the absence of any anodic surface films and the polishing layer described in Section 5.3.2. In this case, an oxygen bubble layer, which is located at the cementite substrate, contributes to the polarization resistance.

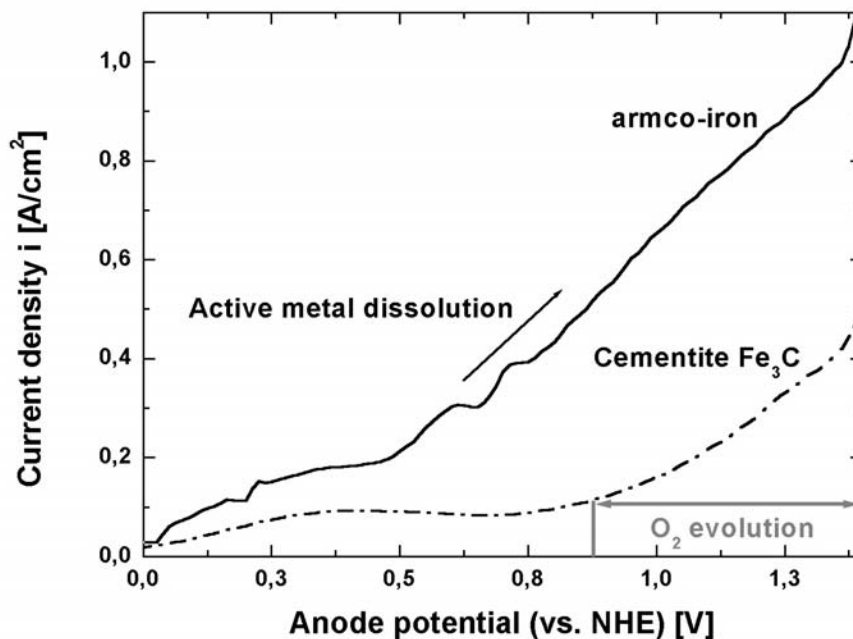


Fig. 5.9c: Anodic polarization curves of armco-iron and cementite (Fe_3C). Potentiodynamic experiments were carried out with a capillary cell. Scan rate: 50 mV/s; electrolyte: aqueous NaCl (20 wt. %); electrolyte temperature: 25°C. The polarization curve of the armco-iron substrate corresponds to divalent iron dissolution. The cementite substrate does not dissolve; oxygen evolution at the substrate / electrolyte interface occurs at potentials $> +0.9 \text{ V}$ (vs. NHE).

5.3.7 Substrate surface morphologies

Typical substrate surfaces of various specimens investigated in this work, after the electrochemical dissolution, are shown in Figs. 5.10a-d (the white arrows indicate the electrolyte flow direction). Before investigation of the substrate surfaces shown, the developed solid surface film (see Section 5.3.2) was completely removed by washing with distilled water. For comparison, an ECM-treated pearlitic C45 steel substrate is shown, from which the solid surface film was not removed (Fig. 5.10c): the very heterogeneous surface film structure built up by various particles is clearly visible.

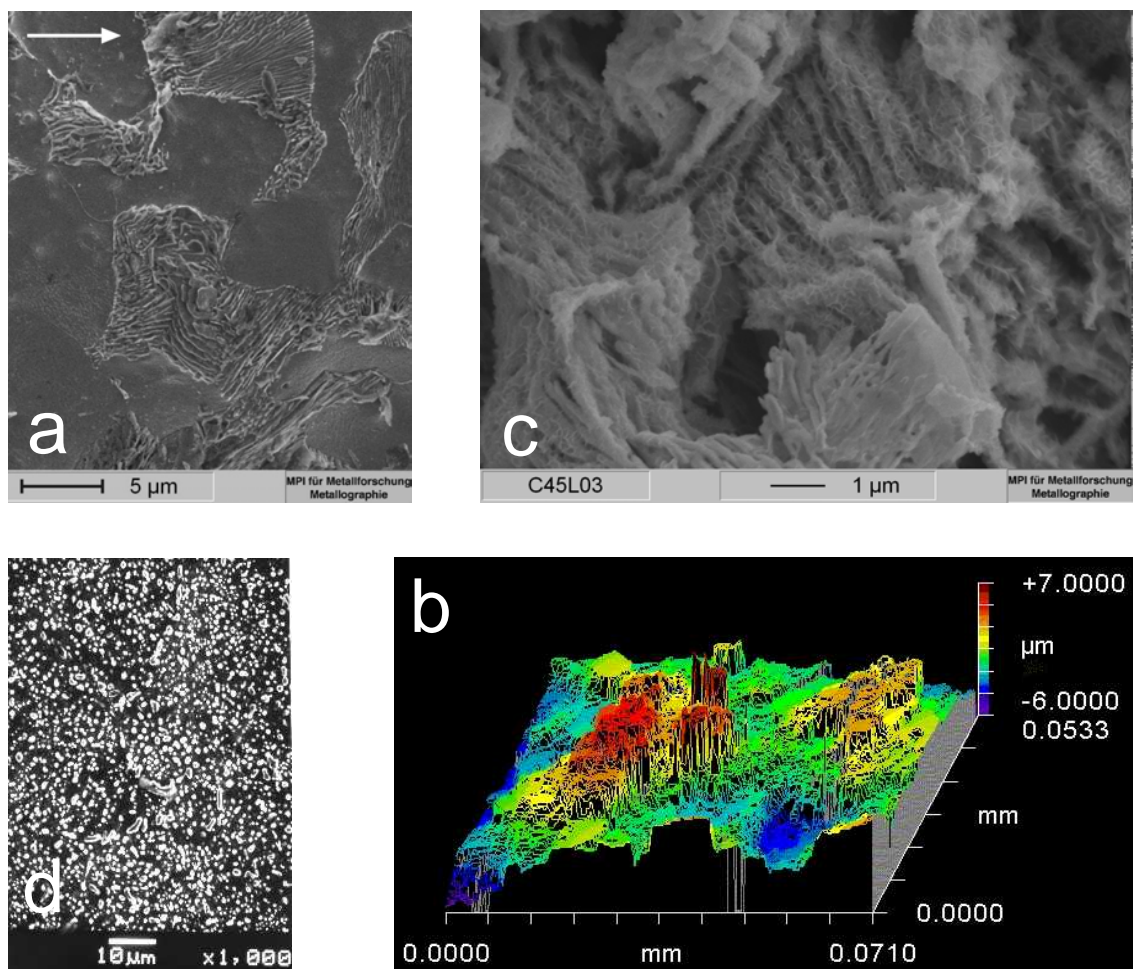


Fig. 5.10: Typical surface morphologies obtained by high rate metal dissolution experiments with the flow channel. NaCl (20 %); 40°C, 7 m/s, 20 A/cm², 40 s
(a) pearlitic C45 substrate (SEM), after washing procedure
(b) pearlitic C45 substrate (white light interferogram)
(c) pearlitic C45 substrate (SEM), the solid surface film was not removed
(d) soft annealed 100Cr6 substrate (SEM), after washing procedure

The difference in metal dissolution behaviour between ferrite regions and pearlitic areas is evident upon considering the ECM-treated surface of a pearlitic C45 steel substrate (see Fig. 5.10a). The ferrite grains have been dissolved preferentially, whereas cementite (Fe_3C) is relatively inert; as a result Fe_3C lamellas protrude from the surface in the pearlitic areas. The corresponding surface relief is presented in the white light interferogram shown in Fig. 5.10b (the interferogram was recorded using a „ZYGO NewView 5000“ interferometer). The green areas represent the ferrite regions; the protruding cementite lamellas occur in the red and orange areas.

A typical soft annealed microstructure after ECM is shown in Fig. 5.10d. It follows, that the globular carbides in the steel matrix (white spots in the scanning electron micrograph) do not dissolve upon ECM, just as observed for the cementite lamellas in the pearlitic microstructure.

5.4 Steel substrate dissolution mechanisms

5.4.1 Soft annealed steels

Evidently, the microstructure of the steel, as determined by heat treatment and carbon (and alloying element) content, strongly influences the Electrochemical Machining Process.

The results obtained in this paper for the soft annealed steels have led to the model description given in Fig. 5.11. Before the electrochemical metal dissolution the soft annealed steel specimen consists of a ferrite matrix which includes small, globular M_3C carbides (diameter $\leq 1 \mu\text{m}$, see Section 5.3.1) and, in addition, usually small amounts of non-metallic inclusion compounds. Upon electrochemical metal dissolution, iron (ferrite) dissolves (is oxidized to a divalent state at the active metal / electrolyte interface; the interface is marked by black ellipses), whereas the globular M_3C carbides are electrochemically inert and do not dissolve (see Figs. 5.9c and 5.10d). The Fe^{2+} -ions enrich in the electrolyte (aqueous NaCl solution) and form solid reaction products, such as FeCl_2 , $\text{Fe}(\text{OH})_2$, FeO and other solvated species [78]. These reaction products ($\text{Fe}_x\text{O}_y\text{Cl}_z$) are the main components of the polishing layer (solid salt film **C**). Preferential dissolution at the metal grain boundaries leads to the formation of troughs at the specimen surface. The globular carbides (M_3C), originating from the steel matrix, and the metal oxides (Fe_xO_y), formed at the metal /

electrolyte interface during the ECM process, enrich at the specimen surface (film **B**). This solid film **B** can easily be ruptured by mechanical action exerted by solid particles in the turbulent electrolyte flow and the corrosive attack of chloride ions (the corrosive influence of Cl^- ions is not shown in Fig. 5.11). The fact that the black solid surface film, formed on the soft annealed steels, is removable from the substrate by a simple washing procedure proves its „damaged“ condition; see the description of the „erosion-corrosion“ mechanism given in Ref. [65].

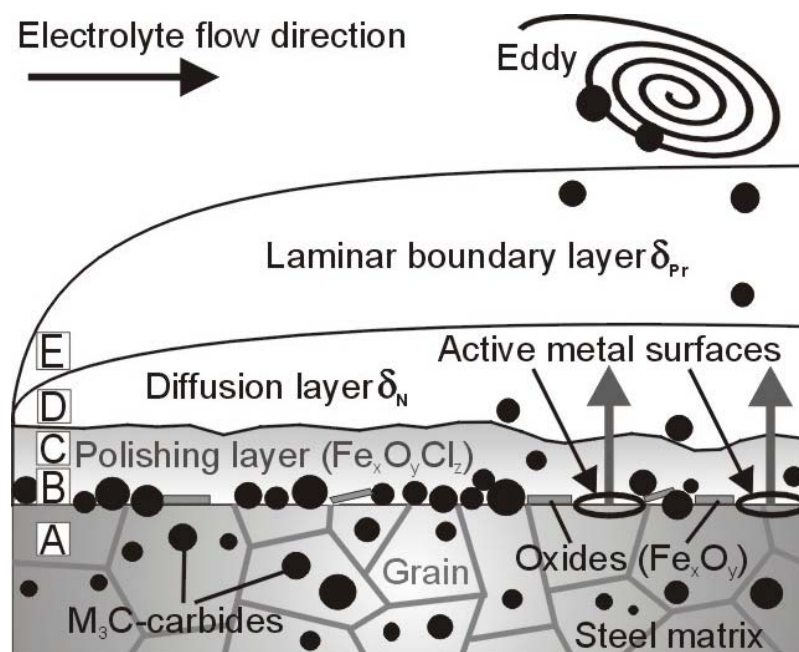


Fig. 5.11: Schematic presentation of surface films / layers developing upon the electrochemical dissolution of soft annealed steels: **A** = steel substrate, **B** = black, solid surface film formed by carbides (M_3C) and non-protective oxides (Fe_xO_y) directly on the substrate surface, **C** = thin polishing layer (salt film, $\text{Fe}_x\text{O}_y\text{Cl}_z$) developed by precipitation from the electrolyte, **D** = the diffusion layer δ_N in the flowing liquid and **E** = hydrodynamic laminar boundary layer δ_{Pr} . The solid surface films **B** and **C** cannot be clearly separated from each other. The ferrite matrix is selectively dissolved, the globular carbides (black spots) are inert. The solid components enriching at the substrate surface can be removed easily by the turbulent electrolyte flow (indicated by the localized eddy). Active areas for iron dissolution at the ferrite / electrolyte interface have been indicated by black ellipses.

5.4.2 Pearlitic steels

The metal dissolution model proposed in Section 5.4.1 for the soft annealed steels cannot hold for the electrochemical dissolution process of pearlitic steels with a high carbon weight percentage (≥ 0.45 wt. %) because the results of galvanostatic, potentiostatic and potentiodynamic experiments indicate that the prevailing reaction mechanisms depend on current density, reaction time and carbon content (see Sections 5.3.3, 5.3.4 and 5.3.5). A model for the dissolution mechanism should incorporate the role of the lamellar carbides in the pearlite. The proposed model description is illustrated in Figs. 5.12a-b. Before electrochemical metal dissolution, a flat polished steel surface with ferrite grains and pearlite colonies occurs (for simplification only two extreme different orientations of carbide lamellas are shown). The lateral size of a single carbide lamella within a pearlitic microstructure can easily be $15 \mu\text{m}$ (see Section 5.3.1).

Two electrochemically different regions have to be distinguished: the carbide-rich areas containing the inert M_3C carbides, which hinder the electrochemical dissolution of the ferrite located under and between these carbides and the regions of pure ferrite where metal dissolution is expected to take place just as for the ferrite in the soft annealed condition. At the onset of current flow the ferrite areas experience iron dissolution with high iron removal rates (indicated with grey arrows in Fig. 5.12); The polishing layer, developing between the carbides located in the pearlite grains, becomes very thick since it is protected from the turbulent flow. Hence, the ferrite located in pearlite grains dissolves at a very low overall rate.

The next stage of the dissolution process of pearlitic steels is illustrated in Fig. 5.12b. The total area, where distinct metal dissolution is possible, decreases continuously, because formerly active ferrite regions become covered with fragments of lamellas set „free“ by metal dissolution. A lot of the lamellar carbides are still strongly attached to the ferrite matrix and oxygen evolution is enhanced. Refreshment of electrolyte between the single carbide lamellas is hindered, leading to enhanced salt precipitation between the carbides. As the result, a composite solid surface film (see Section 5.3.2) develops upon increasing dissolution time which is composed of fragments of inert carbide lamellas, iron oxides formed during the ECM process and precipitated salts (as $\text{Fe}_x\text{O}_y\text{Cl}_z$) in the polishing (sub-)layer. Hence, the active metal

dissolution regions are much smaller than in case of the soft annealed condition, and thus significantly lower current efficiencies occur (see Section 5.3.3).

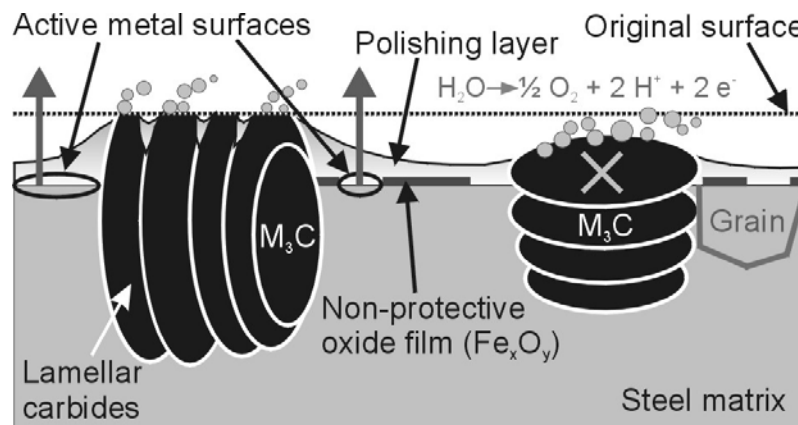


Fig. 5.12a: The electrochemical metal dissolution process of a pearlitic steel substrate after removal of some μm ferrite (the original surface was polished). The not dissolved, lamellar M_3C carbides are still embedded and „anchored“ by the steel matrix due to their large extent. Metal removal is hindered in carbide-rich regions (indicated by the grey cross), oxygen evolution at the electronically conductive carbides takes place (grey bubbles). Iron dissolution is observed in the ferrite regions between the carbides (grey arrows) and a polishing layer ($\text{Fe}_x\text{O}_y\text{Cl}_z$) is formed. The non-protective oxide layer (Fe_xO_y) does not hinder the ECM Process.

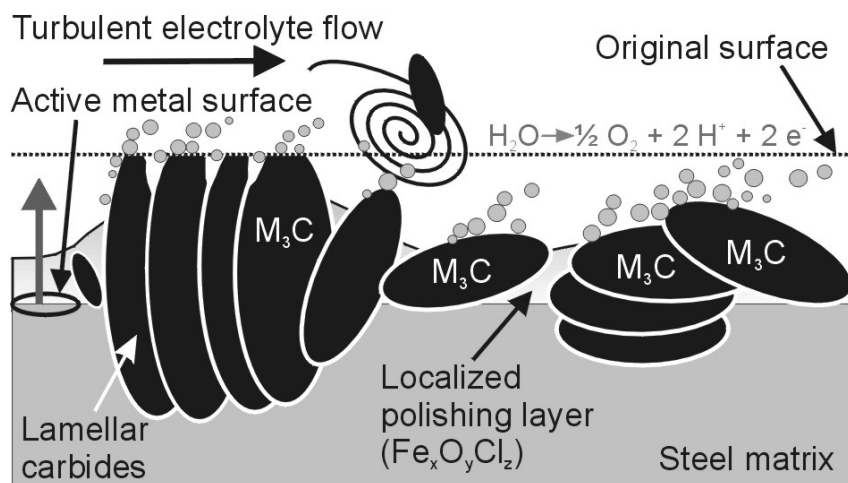


Fig. 5.12b: The electrochemical metal dissolution process of a pearlitic steel substrate after removal of more than $10\ \mu\text{m}$ ferrite. Some carbide particles have left the steel matrix and enrich in a relatively compact surface film, which hinders the metal dissolution and the diffusion of reaction products to the flowing electrolyte. The polishing layer ($\text{Fe}_x\text{O}_y\text{Cl}_z$) between the carbides gets thicker with increasing

dissolution time. The erosion of „free“ carbides cannot easily be realized as for the soft annealed condition (cf. Fig. 5.11) and therefore the overall active metal surface decreases drastically. As a consequence, oxygen evolution can become the dominating reaction.

5.4.3 Model of carbide film growth

Since experiments start with a polished surface, carbide lamellas grow slowly out of the surface. The distance from the top of a protruding single carbide lamella (here assumed to be orientated perpendicular to the surface) to the surface, d_{free} , is a linear function of the dissolution time t (see also Fig. 5.13):

$$d_{free} = k_1 t \leq 0.8 d_{max} \quad (5.13)$$

with k_1 given by the dissolution rate of ferrite. The full lateral size of a single carbide lamella is $d_{max} \approx 15 \mu m$ (see Section 5.3.1). A final value of d_{free} is reached, when the carbide particle leaves („falls out of“) the ferrite matrix during the ECM process which may happen when less than 20% of the carbide are fixed in the steel. Then, a steady state is reached, since new carbide particles reach the surface and protrude. The following equation is suggested in order to describe the time dependence of the average $d_{free,av}$:

$$d_{free,av} = \frac{k_1 t}{1 + k_2 t} \quad (5.14)$$

with k_2 as time constant dependent on d_{max} . A schematic presentation of the function $d(t)$ vs. t is given in Fig. 5.13 with the following approximations:

$$\text{for } t = 0; \quad d(t) = 0 \quad (5.15a)$$

$$k_2 t \ll 1; \quad d(t) = k_1 t \quad (\text{linear function}) \quad (5.15b)$$

$$k_2 t \gg 1; \quad d(t) \sim \frac{k_1}{k_2} \quad (\text{limiting value}) \quad (5.15c)$$

This simple model allows an interpretation of the linear relation observed in Fig. 5.8b. Due to its speculative character, it is given in Section 5.6 (appendix).

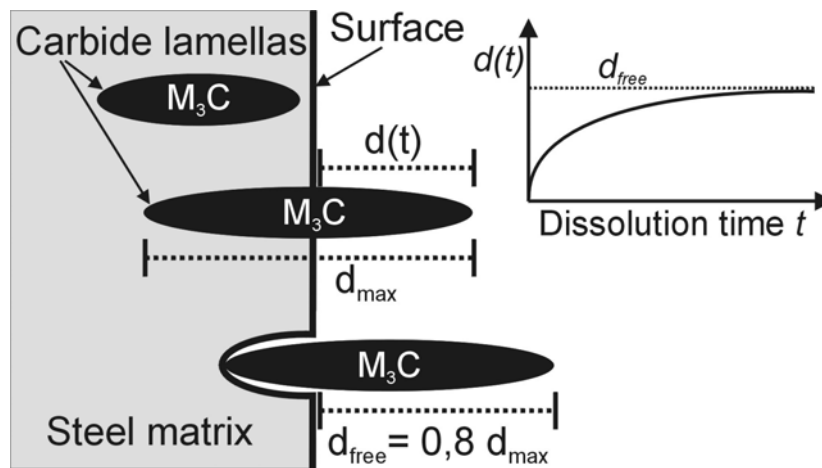


Fig. 5.13: Lamellar carbides protruding from the ECM-treated substrate surface. The carbides (M_3C , black ellipses) are assumed to have a perpendicular orientation with respect to the surface. The distance from the top of a single carbide to the surface level $d(t)$ is a function of the dissolution time. When a critical value is reached, the M_3C particle leaves („falls off“) the steel matrix.

5.4.4 Oxygen evolution and potential distribution at the interface

A very thin, ion conducting film of oxy-chloride ($Fe_xO_yCl_z$) covers the ferrite regions and a polishing layer forms on top of that layer. The polishing film will grow fast on the ferrite covering the inert cementite at first. After an incubation period, however, the cementite will penetrate the polishing film and come in direct contact with the solution. This causes an inhomogeneous potential distribution.

The Fermi level at the electronic conducting Fe_3C -surface will be the same as on the ferrite. In the electrolyte, we have the same local potential. But within the polishing film, an Ohmic potential drop, iR_{film} , exists which causes the ion transport. Therefore, the local electrode potential of the lamella top, U_{carb} (with $U_{carb} = U_{ferr} + iR_{film}$), at the interface Fe_3C / electrolyte will exceed that of the ferrite, U_{ferr} , covered by the polishing film by iR_{film} . This explains why oxygen evolution (experimentally seen as bubbles, indicated with grey bubbles in the figures) may take place at the lamella, while on the ferrite still reactions (5.1a,b) take place at lower potentials.

Due to the high potential at the carbide surface, reaction (5.1b) may be favoured at higher current densities (note that the migration of Fe^{3+} -ions in the electric field is faster than that of Fe^{2+} -ions). Then, the thickness of the polishing film

may decrease, and the formation of Fe^{3+} -ions is enhanced. Therefore, in the vicinity of carbides, the current efficiency will approach 60% as is observed in region C of Figs. 5.6c,d. That means, that due to the change of the polishing film, the oxygen evolution (5.1c) will decrease at high current densities.

5.5 Conclusions

1. The occurring microstructure of steels, as determined by heat treatment and carbon (alloying element) content, strongly influences the electrochemical dissolution behaviour. Whereas the differences between armco-iron or C15 (in either the soft annealed or pearlitic condition) are small, pronounced differences occur between the electrochemical dissolution behaviours of the soft annealed and pearlitic microstructures of the steels C45, C60 and 100Cr6.
2. Galvanostatic flow channel experiments reveal two types of dissolution mechanisms: the „armco type“ with current efficiencies closely to the calculated maximum (holds for armco-iron and soft annealed steels) and the „pearlite type“ with significantly lower current efficiencies (for pearlitic steels with carbon content ≥ 0.45 wt. %). For the „pearlite type“, oxygen evolution, increasing with increasing carbon content, takes place at the electronically conductive carbide lamellas protruding from the surface upon ferrite dissolution. The current efficiency vs. current density curves are separated in 3 regions. In region A, η_{max} is observed, in region B the local minimum occurs in combination with severe O_2 evolution and in region C at least two simultaneous processes take place (Fe^{n+} dissolution and O_2 evolution).
3. Potentiostatic current transient measurements with the rotating cylinder electrode indicate an approximately linear current-time dependence for armco-iron and the soft annealed steels. The (negative) slope of the transients has been measured as $-16 \text{ mA} / 60 \text{ s}$. For the pearlitic steels, a reciprocal correlation $1/I$ vs. t , with the slope dependent on the carbon content, has been observed. For a simple model see appendix.
4. Potentiodynamic measurements with the rotating cylinder electrode show very small contributions of R_{film} to the polarization resistance R_{pol} of a soft annealed C45 substrate ($R_{pol} \approx 0.31 \text{ } \Omega\text{cm}^2$). In contrast to that, a very strong influence

of R_{film} is observed for pearlitic C45 substrates since the value of R_{pol} is nearly doubled ($R_{pol} \approx 0.60 \Omega\text{cm}^2$), i.e. $R_{film} \approx 0.3 \Omega\text{cm}^2$.

5. Potentiodynamic measurements with the capillary cell demonstrate the exclusive divalent iron dissolution of armco-iron at anode potentials ≥ 0 V (vs. NHE). The corresponding polarization curve represents the potential dependence of $i_{Fe^{2+}}$. In contrast to that, dominating oxygen evolution at the cementite (Fe_3C) surface takes place exclusively at potentials $\geq +0.9$ V (vs. NHE). The cementite substrate is electronically conductive and doesn't dissolve during anodic polarization.
6. For soft annealed steels, the ECM process is mainly based on divalent iron dissolution. Inert, globular carbides (M_3C) and iron oxides (Fe_xO_y) enrich at the substrate surface and are removed by local turbulences according to an „erosion-corrosion“ mechanism. Iron dissolution is not significantly hindered since the solid surface film is non-protective, incoherent and loosely bound. A polishing layer, surrounding the solid carbide / oxide particles, is formed by reaction products (salts as $\text{Fe}_x\text{O}_y\text{Cl}_z$).
7. Solid carbide / oxide films formed on pearlitic steels ($\text{C} \geq 0.45$ wt. %) are connected stronger to the steel matrix due to the large extent (lateral size) of the carbide lamellas. The relatively thick and compact solid surface film hinders iron dissolution from ferrite. The large carbide areas protruding from the surface give rise to severe oxygen evolution. The areas, where iron dissolution occurs become smaller during the ECM process because they are covered increasingly with fragments of carbide lamellas. The polarization resistance, R_{pol} , of the pearlite system increases significantly with increasing dissolution time, which is ascribed with the formation and growth of a polishing layer located between the carbides.
8. In summary, the shift of dissolution reaction (5.1a) at armco-iron to (5.1b) and (5.1c) on carbide rich pearlitic steels is due to the inert electronic conducting cementite which causes topographic changes and an increasing local potential at very high current densities.

5.6 Appendix

As shown in Fig. 5.8b, the reciprocal current of pearlitic steels depends approximately linearly on reaction time. This may be understood recognizing the geometry of the lamellar carbides protruding from the surface upon metal dissolution (see Fig. 5.13). The average thickness of the polishing layer d_{polish} is a function of d_{free} :

$$d_{polish} = k_3 d_{free} \quad (5.16)$$

To explain the linearity of $1 / I_{Fe^{2+}} = f(t)$ shown in Fig. 5.8b, the model of Section 5.4.3 may be extended. For the current I due to divalent iron dissolution $I_{Fe^{2+}}$ and the thickness of the polishing layer d_{polish} the relationship (5.17) is suggested:

$$1 / I_{Fe^{2+}} \sim d_{polish} \quad (5.17)$$

With equations (5.15) and (5.16) the following expression for $1 / I_{Fe^{2+}}$ is obtained:

$$1 / I_{Fe^{2+}} = k_3 d_{free} = \frac{k_1 t}{1 + k_2 t} k_3 \quad (5.18)$$

For the case of equation (5.15b) it follows, that $1 / I_{Fe^{2+}} = k_1 k_3 t$.

As the result, a proportional behaviour $1 / I_{Fe^{2+}} \sim t$ is found.

Chapter 6

High rate anodic dissolution of steel 100Cr6 in aqueous NaNO₃ solution

Thomas Haisch, Eric Jan Mittemeijer and Joachim Walter Schultze

Abstract

The high rate anodic dissolution of the steel 100Cr6 in NaNO₃ electrolytes of various concentrations and at different temperatures was investigated. Galvanostatic flow channel experiments were used to examine the current efficiency of the steel substrate. Below 10 A/cm², oxygen evolution dominates, while at higher current densities iron dissolution prevails. Rotating cylinder measurements served for polarization studies at lower current densities in the region of dominating O₂-evolution. Scanning electron micrographs revealed the correlation between the current efficiency and the coverage of the substrate surface with an electronically conductive film at current densities of 2, 9 and 20 A/cm². The microstructure of the black, solid surface film developing upon the high rate anodic dissolution of the steel was found to be heterogeneous and very porous. The main film components, as determined by X-ray diffraction and Auger electron spectroscopical measurements, were amorphous iron oxides, Fe_xO_y, and inert carbides, M₃C, originating from the steel matrix. Potentiodynamic polarization studies indicated a complete substrate surface passivation up to +1.8 V (vs. NHE), and periodic fluctuations of the current density at higher anode potentials (> +1.8 V) due to severe oxygen evolution. An activation-repassivation-process was proposed, that can be responsible for the development of the complex multilayer (multiphase) structure observed at the steel substrate surface in association with the occurrence of diverse anodic reactions, which compete with each other.

6.1 Introduction

The high rate electrochemical dissolution of iron and steels, as pertaining to Electrochemical Machining (ECM), in sodium nitrate electrolytes has been the subject of a number of studies [16-19, 32, 51, 87-89]. The results obtained from anodic polarization curves, current-efficiency measurements and analysis of the resulting substrate-surface morphologies show that NaNO_3 electrolytes have a passivating effect on iron-based substrates. It was found, that at low current densities ($i \leq 4 \text{ A/cm}^2$) no metal is dissolved (current efficiency $\eta = 0$). On this basis exact dimensional control can be achieved in Electrochemical Machining processes without mask techniques, such as holds for the fabrication of turbine-engine parts, automotive components and electrochemical hole drilling [16, 17, 21, 32, 51, 82].

It is well known, that the passivation of the substrate (anode) surface under conditions typical of ECM is due to complex anodic surface films developing at the substrate / electrolyte interface [31, 65, 72, 82, 87-91]. Several models for the development of these anodic surface film structures have been proposed. Usually a dual film structure is supposed: a hydrated oxide compound ($\text{Fe}_2\text{O}_3 \cdot x \text{H}_2\text{O}$, FeOOH) film and a salt film precipitated from the NaNO_3 solution [21, 31, 32]. Due to the heterogeneous structure of a steel substrate, metal carbides influence the composition of the anodic surface film and thereby the polarization behaviour of the substrate [65, 72]. Further, oxygen evolution at the anode surface has been observed as a competing reaction to metal dissolution [21, 24, 28, 54, 72, 91-94].

The purpose of this work is to investigate the mechanisms of metal dissolution, gas evolution and the solid surface film formation on the substrate of steel 100Cr6 in particular with a view to the intrinsic heterogeneity of the steel substrate.

6.2 Experimental

Commercially obtained 100Cr6 steel specimens were used for the ECM experiments (rod material in soft annealed condition). The composition of the steel is as follows (in wt.%): C: 0.97; Cr: 1.43; Si: 0.28; Mn: 0.28; Ni: 0.11; P: 0.006; S: 0.002; Fe: 96.92.

For the electrochemical dissolution experiments in the flow channel cell, a quadratic electrode surface of 1 cm^2 was subjected to the flowing electrolyte. The

surface of the 100Cr6 specimen that served as anode was ground and polished mechanically. Platinized copper / tungsten alloy was used as cathode material. The setup of the rectangular flow channel (parallel plate reactor) has been described elsewhere [65]. The average electrolyte flow velocity, u , was set at 7 m/s implying turbulent flow conditions within the flow reactor. The distance between cathode and anode (working gap) was set at 2 mm (smaller working gaps could cause sparking effects upon severe gas evolution). An aqueous NaNO₃ solution (40 wt.%) at 40°C ± 1°C, pH 7, served as electrolyte for electrochemical metal dissolution. All experiments in the flow channel cell were performed *galvanostatically* with average current densities, i , of 5 to 60 A/cm² (direct current). The specimens were subjected to the electrochemical dissolution for 20 to 80 seconds. Then they were removed quickly from the reactor and washed with distilled water.

All polarization measurements were carried out using an EG&G 273A potentiostat with simultaneous detection of the transferred charge, Q . 100Cr6 steel specimens (rings of 12 mm diameter, 0.5 mm height, with a lateral area of 0.19 cm²) were applied as rotating cylinder electrodes (working electrodes, WE). A platinum net served as counter electrode (CE). A commercially obtained Ag/AgCl-electrode was used as reference electrode (RE). The distance between the working electrode and the counter electrode was set at 10 mm. Aqueous NaNO₃ solutions, at pH 7, of various concentrations and at different temperatures served as electrolytes. For the *potentiostatic* measurements, an anode potential of +2.5 V (vs. NHE) was applied. *Potentiodynamic* curves were measured at 25°C with a potential scan rate of 40 mV/s and anode rotation speeds of 590 and 1136 rpm (corresponding to Reynolds-numbers $Re = \omega r^2 / \nu = 1316$ and 2534, with $r^2 = 0.36$ cm² and $\nu_{25^\circ\text{C}} = 0.0169$ cm²/s; i.e. turbulent flow conditions). A single measurement implied one potential cycle („forward scan“ and „reverse scan“).

For the ex situ scanning electron microscopy (SEM), X-ray diffraction and Auger-electron spectroscopical (AES) investigations (see sections 6.4.2 and 6.4.3), the ECM-treated substrate was removed quickly from the reactor (flow channel cell or rotating cylinder electrode) and washed with distilled water. By this procedure, remainders of the NaNO₃ electrolyte were removed completely from the black surface film that was attached strongly to the steel specimen. Finally, the steel substrate was dried in a stream of nitrogen.

AES spectra were recorded with a PHI 600 Scanning Auger Microprobe. A sputter-depth profile (using Ar⁺ ions of 3 keV for sputtering) was recorded over an area of 1 x 1 mm² at an incidence angle of 60° with respect to the surface. As a measure for the peak intensities the peak-to-peak height of the differentiated spectra was used. The sputter rate of 16 nm/min was calibrated using a Ta₂O₅-specimen as reference.

The X-ray diffraction analysis was performed with a Philips X'Pert diffractometer equipped with a Cu tube and a graphite monochromator in the diffracted beam to select CuK α radiation. The diffracted intensity was recorded in the range of 20° to 130° 2 θ with a step size of 0.05° 2 θ . All diffraction data required for interpretation of the X-ray diffraction patterns were taken from the JCPDS-International Centre for Diffraction data (PCPDFWIN database, version 2.01).

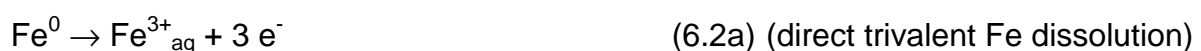
The current efficiencies of the galvanostatic flow channel experiments (see section 6.4.1) and the integral current efficiencies of the potentiodynamic measurements (see section 6.4.4) were calculated according to the procedure described in Ref. [72].

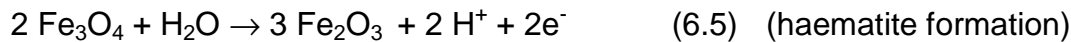
6.3 Electrode reactions

In order to discuss the electrochemical reactions and metal dissolution mechanisms involved in ECM with NaNO₃ electrolytes, a brief summary of possible reactions occurring at anode and cathode is given below.

6.3.1 Anodic electrode reactions

The principal, desired ECM process is the simple divalent iron dissolution at the iron (-based) substrate / electrolyte interface (reaction 6.1; see below). If additional, competing anodic reactions occur at the substrate surface (reactions 6.2-6.5), current efficiencies $\eta < 100\%$ are observed.





Generally the main reactions are (6.1-6.3) [16, 17, 51]. Current efficiencies of 66.6 % indicate exclusive occurrence of reaction (6.2a) and high current efficiencies ($\eta \approx 100\%$) imply dominance of reaction (6.1). Current efficiencies of about 100% have been observed for the case of NaCl electrolyte but not for NaNO₃ electrolyte [72]. If no metal dissolution occurs, oxygen evolution according to (6.3) dominates (see section 6.4.1). Occurrence of the reactions (6.4) and (6.5) is irrelevant for the current efficiency but can influence strongly the microstructure of the solid film developing at the surface of steel substrates (see section 6.5.1) [32, 72, 87].

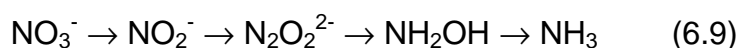
6.3.2 Cathodic electrode reactions

Reductions, which are possible at the counter electrode surface are given by the reactions (6.6-6.8):



Since cathodic gas evolution has not been observed in the present experiments (see section 6.4.4) it is proposed, that reaction (6.6) is the main reaction at the counter electrode upon ECM with NaNO₃ electrolyte. At the very high flow rates applied in ECM, the diffusion and migration of Fe³⁺ from the anode surface to the cathode surface is not fast enough to give rise significantly to reaction (6.7).

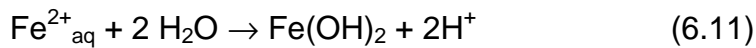
Since continued cathodic reduction of nitrite has been reported, the following intermediates may occur in the electrolyte as well [19]:



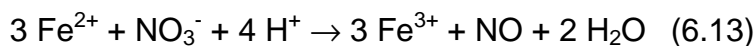
with the corresponding nitrogen valence levels: $+5 \rightarrow +3 \rightarrow +1 \rightarrow -1 \rightarrow -3$

6.3.3 Electroless chemical reactions

The electrochemical reactions given in sections 6.3.1 and 6.3.2 are associated with a charge flow at the electrode / electrolyte interface. Electroless reactions are possible as well, in particular with reference to the anodic processes. Anodic oxygen evolution has been observed frequently in NaNO_3 systems [16, 17, 19, 32, 51, 89]. Then the following, electroless chemical oxidation of iron directly on the steel substrate surface can occur (see section 6.5):



An electroless reaction occurring *within* the anodic diffusion layer has been proposed too [21]:



Since this reaction occurs in the flowing liquid, it will not influence directly the formation, microstructure and composition of the solid surface film on a steel substrate (see section 6.5.1).

6.3.4 pH-shifts at the electrodes

Clearly, reactions (6.3) and (6.8) depend on the pH. Since the alkalization at the cathode will not influence the anodic processes, only the reactions occurring at the steel substrate (anode) will be considered here. If oxygen evolution according to reaction (6.3) occurs, a pH-shift within the anodic boundary layer from 7 downward to 0 or below should be observed. According to the Pourbaix-diagram for the system iron-water [95], given in Fig. 6.1, a solid Fe_2O_3 -film that had developed on the steel substrate would dissolve and release solvated Fe^{3+} -species at potentials above +0.77 V if the pH value decreases to 0 and below. Hence, severe oxygen evolution at the anode promotes dissolution of a solid Fe_2O_3 film present on the substrate, with

occurrence of trivalent Fe species in the electrolyte at potentials higher than +0.77 V. It should be recognized that the data presented in a Pourbaix-diagram pertain to electrochemical equilibria, whereas in ECM processes usually non-equilibrium states occur which restricts the applicability of a Pourbaix-diagram to ECM.

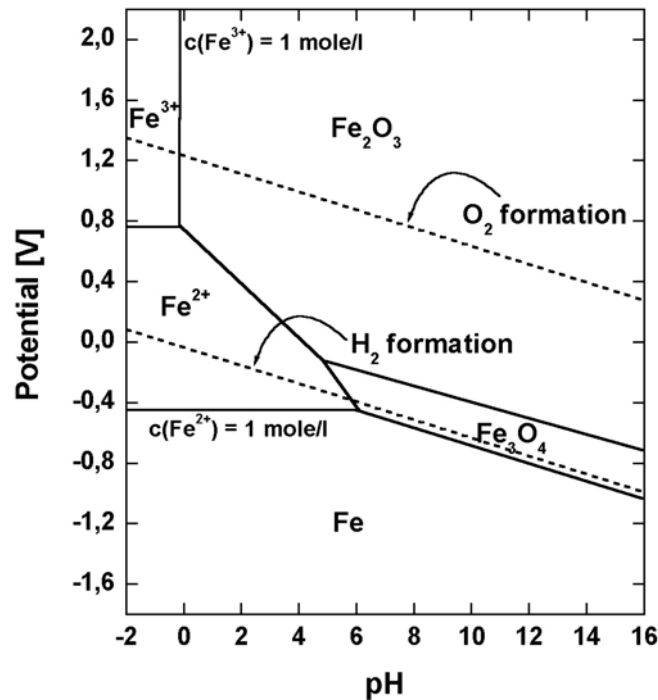


Fig. 6.1: Potential-pH equilibrium diagram for the system iron-water at 25°C according to Pourbaix [95]. In this illustration, only the solid components Fe, Fe₃O₄ and Fe₂O₃ are considered. Oxygen and hydrogen formation have been indicated by dotted lines.

6.4 Results and interpretation

6.4.1 Current efficiency

The current efficiency, η , for the dissolution of the steel 100Cr6 in NaNO₃ (40 wt.%) as a function of the current density is shown in Fig. 6.2. A typical roughly S-shaped curve can be observed (see also Refs. [16, 24, 32, 51, 72]). Three different zones can be distinguished:

In zone A ($i \leq 6 \text{ A/cm}^2$) an evidently completely passivated substrate surface occurs: no metal dissolution takes place ($\eta = 0$). At this stage oxygen gas evolution is

observed (reaction (6.3)). Consequently, the solution at the surface is acidified. The black solid surface film which develops during the ECM process is strongly attached to the steel substrate and is apparently very well electronically conductive, in view of the severe evolution of oxygen bubbles.

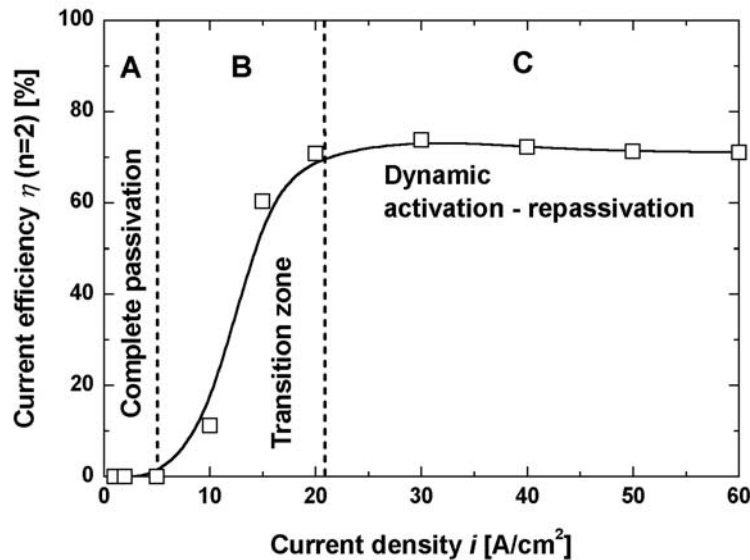


Fig. 6.2: Current efficiency η of the steel 100Cr6 (soft annealed) as observed in galvanostatic flow channel experiments (NaNO_3 (40 wt.%), 7 m/s, 40°C). Three zones can be distinguished: in zone A ($i \leq 6 \text{ A/cm}^2$) no metal dissolution occurs due to a completely passivated substrate surface (presence of black iron oxide and carbide film on the surface); the transition zone B ($6 \text{ A/cm}^2 < i < 21 \text{ A/cm}^2$) is characterized by a steeply increasing current efficiency (increasing film detachment); zone C ($i \geq 21 \text{ A/cm}^2$) is characterized by a plateau level for the current efficiency (dynamic, steady state of activation and passivation; see section 6.5.1).

The transition zone B ($6 \text{ A/cm}^2 < i < 21 \text{ A/cm}^2$) is characterized by a steeply increasing current efficiency. Obviously, the reaction mechanism changes from one involving exclusive oxygen evolution to one that incorporates at least two competing anodic reactions, such as O_2 evolution and Fe^{3+} formation at the same time (note that the current efficiency has been calculated with respect to iron dissolution as Fe^{2+} (reaction (6.1))). The divalent iron dissolution according to reaction (6.1) in combination with O_2 evolution is also possible but no direct evidence for that is available.

Measurements in NaNO_3 solutions in the pH-range 3 to 8 at current densities below 10 A/cm^2 proved the absence of a visible pH-effect. This is understandable on the basis of the acidification caused by reaction (6.3).

The highest current efficiencies ($\eta \approx 70 \%$) occur in zone C ($i \geq 21 \text{ A/cm}^2$). The observed value of η , equal to about 70%, might suggest dominant Fe^{3+} formation. However, at this stage part of the surface is still covered with a surface film (see section 6.4.2). Hence, Fe^{3+} formation, if it occurs, cannot be the only reaction at the anode. In an earlier study on ECM with steel, oxygen gas evolution was still observed at a current density of 47 A/cm^2 [19]. The solid surface film obviously gets ruptured at high current densities (see evidence for film rupturing in section 6.4.2). Partial film breakdown changes the nature of the solid surface film from compact and protective to porous and non-protective (see section 6.4.2).

6.4.2 Anodic surface film structures; film breakdown

SEM micrographs of solid surface films formed on soft annealed 100Cr6 substrates during the Electrochemical Machining process are shown in Figs. 6.3a-c. The surface films were obtained from galvanostatic flow channel experiments with aqueous NaNO_3 (40 wt.%), at 7 m/s, 60s, 40°C .

The steel substrate surface morphology as observed in zone A ($i = 2 \text{ A/cm}^2$) is shown in Fig. 6.3a. The black, solid surface film is strongly attached to the steel substrate and covers the whole surface. It appears to be completely compact and only a few pores ($\varnothing < 1 \mu\text{m}$) are observed (note that at the locations of non-metallic inclusions, dark spots appear in the surface film). Obviously, local or global film breakdown does not occur at the low current densities of zone A.

In the transition zone B ($i = 9 \text{ A/cm}^2$), two types of surface film structures coexist (see Fig. 6.3b): „compact“ regions, where the surface film is not ruptured (very similar to the surface film structure of zone A), and regions exhibiting massive formations of pores within the surface film. Regions on the substrate, where the complete anodic film structure has been detached, cannot be observed; the solid surface film is still strongly attached to the 100Cr6 steel specimen. It may be suggested that all of the electrochemically dissolved ferrite has been transported through electrolyte-filled pores.

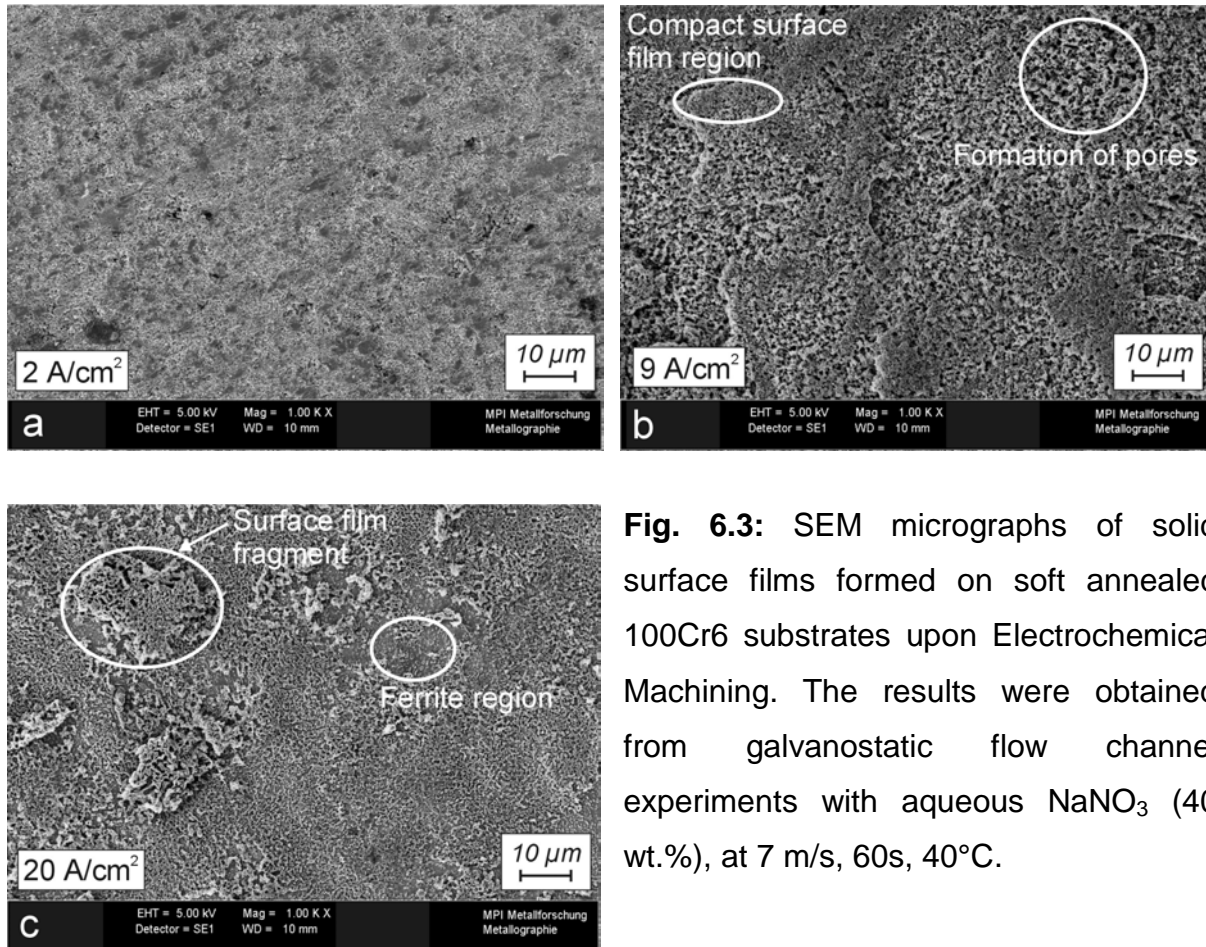


Fig. 6.3: SEM micrographs of solid surface films formed on soft annealed 100Cr6 substrates upon Electrochemical Machining. The results were obtained from galvanostatic flow channel experiments with aqueous NaNO_3 (40 wt.%), at 7 m/s, 60s, 40°C.

- (a) Substrate surface morphology as observed in zone A ($i = 2 \text{ A/cm}^2$): the solid, black surface film covers the whole substrate surface and appears to be completely compact. Only a few pores ($\varnothing < 1 \mu\text{m}$) are observed. Most of the contrast effects observed are due to height differences in the film.
- (b) Two types of surface film structures occur in the transition zone B ($i = 9 \text{ A/cm}^2$): „compact“ regions, where the surface film is not ruptured, and locations with massive formations of pores in the surface film.
- (c) In zone C ($i = 20 \text{ A/cm}^2$), fragments of the surface film have remained on the steel substrate. Most solid components of the initial, black film have been detached from the surface and large regions of bare and then repassivated ferrite occur (see section 5.1).

In zone C ($i = 20 \text{ A/cm}^2$), only a few single fragments of the surface film have remained on the steel substrate (Fig. 6.3c). Most solid components of the film have been detached completely from the steel surface and large regions of the base

substrate; i.e. without surface film coverage, occur. Within the ferrite matrix of the substrate, undissolved carbides of the composition M_3C ($M = Fe, Cr$) can be observed [72].

On the basis of the results presented in Figs. 6.2-6.3, it is concluded, that compact surface films suppress the active ferrite dissolution and promote oxygen evolution at the film / electrolyte interface (note that oxygen evolution is only possible at electronically conductive surface films).

A typical cross-section of a solid anodic surface film developed on a 100Cr6 substrate during the ECM process is shown in Fig. 6.4 (zone B; parameters: flow channel cell, aqueous $NaNO_3$ (40 wt.%), $10 A/cm^2$, 60s, 7 m/s, $40^\circ C$). The surface film itself appears black, the steel matrix is grey in light microscopic investigation. For better contrast, the surface film was covered with a 500 nm silver layer, which appears white in Fig. 6.4. The thickness of the heterogeneous surface film varies extensively (0 - 3 μm) on a local scale and regions of complete film detachment in combination with pitting occur.

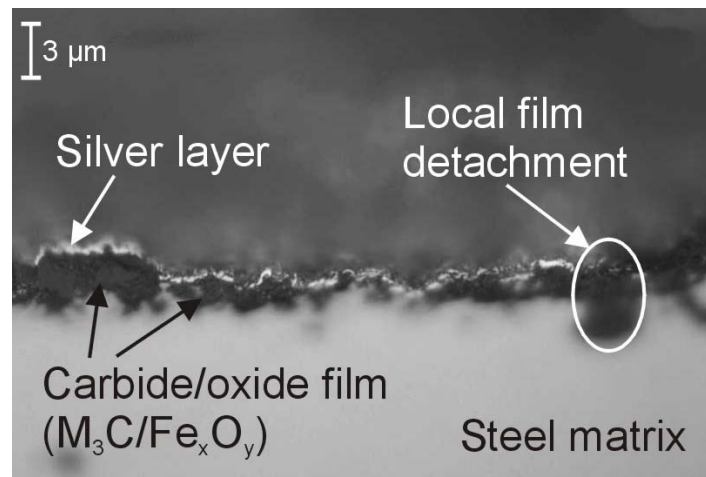


Fig. 6.4: Cross-sectional light optical micrograph (bright field) of a typical solid surface film formed on a 100Cr6 substrate during the ECM process (appears black in light microscopic investigation). Parameters: aqueous $NaNO_3$ (40 wt.%), $10 A/cm^2$, 60s, 7 m/s, $40^\circ C$. The surface of the specimen was covered with a 500 nm silver layer (appears white) before preparation of the cross section, to improve the visibility of the surface film. The local thickness of the heterogeneous surface film varies extensively; local film detachment can be observed.

6.4.3 Surface film composition

As mentioned in section 6.4.2, anodic surface films on iron and steels, developed in NaNO_3 ECM processes, are anchored completely or partially at the substrate, dependent on the current density applied. The surface films that remain on the substrates after ECM can be examined by ex situ investigations like AES.

An AES sputter-depth profile of such a surface film, formed on the steel 100Cr6 in NaNO_3 (transition zone B, see section 6.4.2), is presented in Fig. 6.5. After the removal of surface contamination during the first minutes of sputtering, large values for the C-content of the film were observed (~ 30 atom %), indicating an enrichment of carbide particles at the substrate surface by the preferential dissolution of ferrite (Fe dissolution, see Fig. 6.2). After removal of $\sim 1.6 \mu\text{m}$ film (100 min sputtering) the C-content had decreased from 30 to below 10 atom % and approached the theoretical bulk value of 4.5 atom %. AES-measurements of 100Cr6 steel substrates subjected to the ECM process in NaNO_3 for different reaction times (20s to 50s) revealed the tendency of surface film thickening with increasing reaction time.

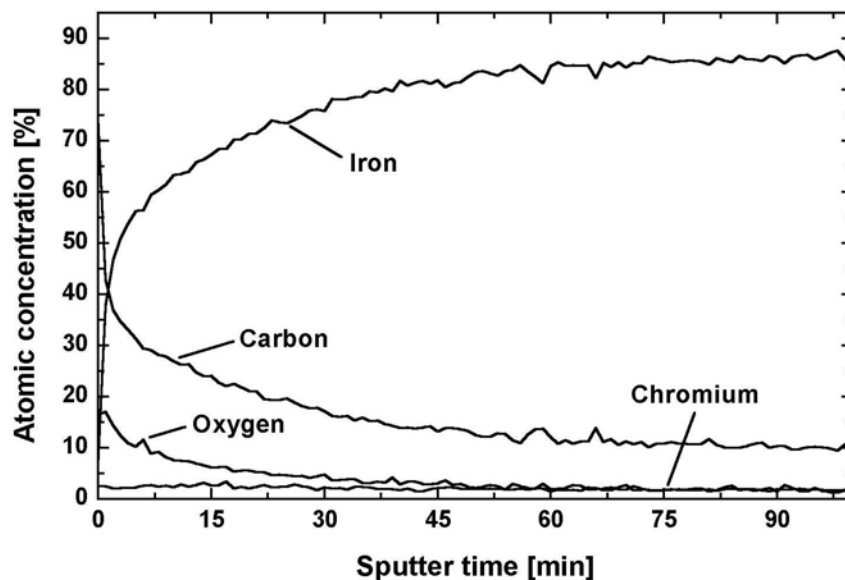


Fig. 6.5: Depth profile (Auger electron spectroscopy) of the solid surface film on a 100Cr6 substrate obtained from galvanostatic flow channel experiments. Parameters: aqueous NaNO_3 (20 wt.%), 20 A/cm^2 , 60 s, 7 m/s. The sputter rate, as indicated by sputtering a Ta_2O_5 -reference specimen, is 16 nm/min.

A substantial value for the atomic concentration of oxygen occurs within the anodic surface film, which is compatible with the presence of oxides as basic film components.

X-ray diffraction patterns of a polished 100Cr6 reference specimen and of a 100Cr6 substrate after the ECM process with NaNO_3 are shown in Fig. 6.6.

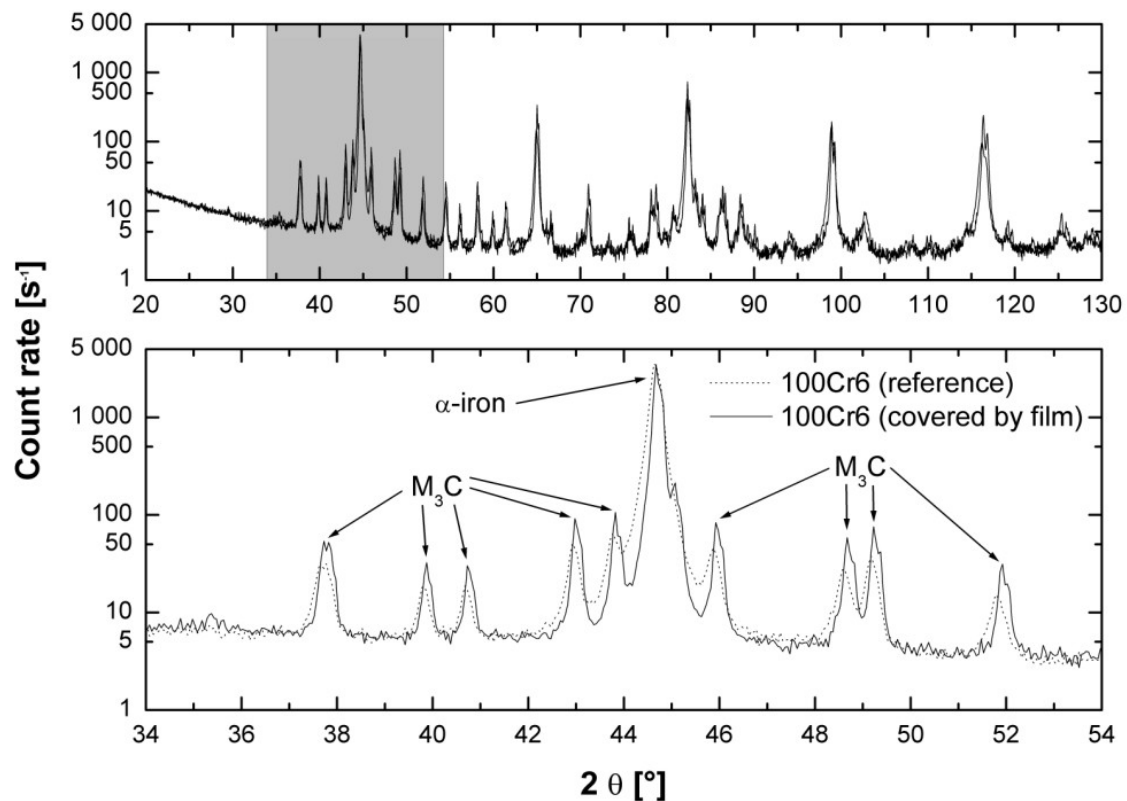


Fig. 6.6: X-ray analysis of a polished 100Cr6 reference in comparison with an ECM-treated substrate (NaNO_3). The detected components of the 100Cr6 reference are the α -iron matrix and carbides of the composition M_3C (cementite type). The same components are observed in the surface film, but the relative concentration of M_3C carbides is higher (note the increased intensities of the M_3C peaks). The diffraction data were normalized to the most intense α -iron peak occurring at $2\theta = 44.7^\circ$.

The identified (and expected) components of the 100Cr6 reference (dotted line in Fig. 6.6) are the α -iron matrix and carbides of the composition M_3C (cementite type, see the enlarged parts of the diffraction patterns in Fig. 6.6). The same components are observed for the substrate covered with the surface film, but the relative concentration of M_3C carbides appears larger (note the intensities of the M_3C peaks; the diffractive intensities were normalized with respect to the most intense α -iron

peak occurring at $2\theta = 44.7^\circ$). Diffraction peaks from iron oxides (Fe_xO_y) could not be clearly identified (it may be speculated that the peaks at $35^\circ < 2\theta < 36^\circ$ belong to iron oxides, but the measured intensities are too weak for unambiguous identification). This may suggest that the iron oxide(s) present in the surface film is (are) amorphous (note that oxygen was detected by AES).

6.4.4 Polarization studies

The potentiodynamic anodic polarization curves observed with 100Cr6 specimens applying the rotating cylinder electrode (RCE) indicate, that active ferrite dissolution at low anode potentials does not occur in NaNO_3 electrolyte (see Fig. 6.7a). In contrast to typical activating ECM systems (which contain halide ions in the electrolyte [16, 65, 84]), up to +1.8 V (vs. NHE) no current flow is observed due to the complete passivation of the steel surface (see also results discussed in section 6.4.2). It is important to note that the existence of the passive region was found not to depend on the concentration of the NaNO_3 electrolyte (Fig. 6.7a). Obviously, nitrate ions in aqueous solutions are not able to activate the substrate surface at low potential (see the anodic anion (halide) activation theory proposed by Davydov [24, 84, 85]). The approximately linear behaviour of the polarization curves for anode potentials above +1.8 V is due to the onset of oxygen evolution, which is the main electrode reaction at low potential (see section 6.3.1). This is in accordance with integral current efficiencies $\eta < 25\%$ (calculated for Fe^{2+} dissolution), as determined for this potential range (note that the current efficiency values of the RCE experiments cannot be directly compared to those of the flow-channel-cell experiments: the current density during the RCE experiment varies, whereas the current density during the flow-channel-cell experiments is constant). The polarization resistances, R_p , as determined from the slope, dU / di , of the linear parts of the polarization curves, are $0.54 \text{ } \Omega\text{cm}^2$ (2-m- NaNO_3), $0.36 \text{ } \Omega\text{cm}^2$ (4-m- NaNO_3) and $0.29 \text{ } \Omega\text{cm}^2$ (6-m- NaNO_3) (see also the equivalent circuit presented in section 6.5.2). The relation of these polarization resistances to the corresponding separately measured conductivities of the NaNO_3 electrolyte (113 mS/cm (2-m), 160 mS/cm (4-m) and 176 mS/cm (6-m)) was found to be linear.

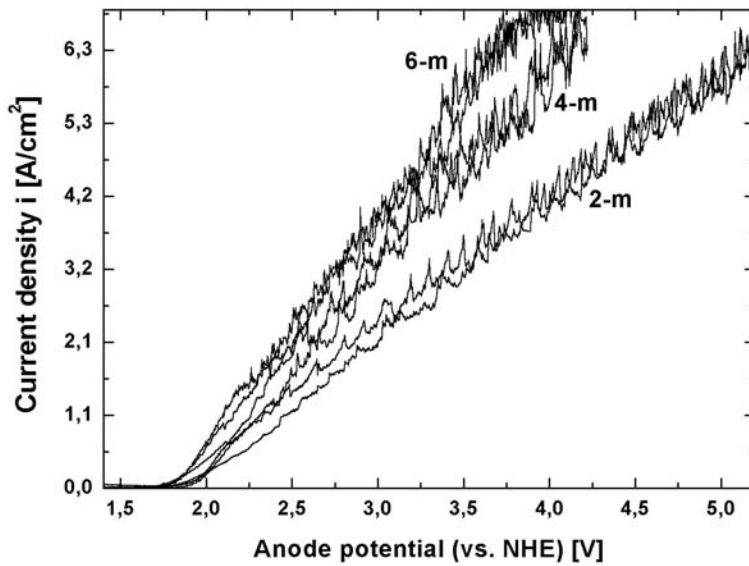


Fig. 6.7a: Anodic polarization curves of the steel 100Cr6 (soft annealed) in aqueous NaNO_3 solutions of different concentrations (2-m, 4-m and 6-m). These results were obtained by potentiodynamic RCE-experiments (scan rate: 40 mV/s, rotation speed: 590 rpm, temperature: 25°C, cycles: 1). The fluctuations of the current density are caused by severe gas evolution at the working electrode.

The O_2 bubble formation at the anode surface becomes obvious, when the periodic fluctuations superimposed on each polarization curve are recognized (see Fig. 6.7b). The enlarged part of the 2-m- NaNO_3 polarization curve (forward scan) illustrates typical fluctuations in current density due to repeated O_2 bubble growth and detachment. At the points of steep upward „jumps“ of the current density i , the detachment of an O_2 bubble collective, in association with local turbulences in the electrolyte, is observed (visual inspection of the anode surface). As a consequence, the resistance of the bubble layer, R_{gas} , drops immediately to lower values (see also section 6.5.2). The current-density fluctuations, Δi , observed are in the range of 0.2 – 0.8 A/cm^2 .

Visual appearance of oxygen evolution at the passivated 100Cr6 steel surface, is shown in Fig. 6.8. The experiment shown was carried out potentiostatically at a potential of +2.5 V (vs. NHE), where the whole substrate surface is covered by a black, solid anodic film (for the purpose of clearer illustration, in this case a cylinder electrode height of 10 mm instead of 0.5 mm was chosen; cf. section 6.2). Without rotation, small O_2 gas bubbles ($\varnothing < 200 \mu\text{m}$) develop on the anodic film. The

distribution of these small O_2 bubbles at the substrate surface is rather uniform. At the edge of the working electrode cylinder, very big gas bubbles ($\varnothing < 1.8$ mm) are formed due to the locally higher current densities or faster bubble nucleation.

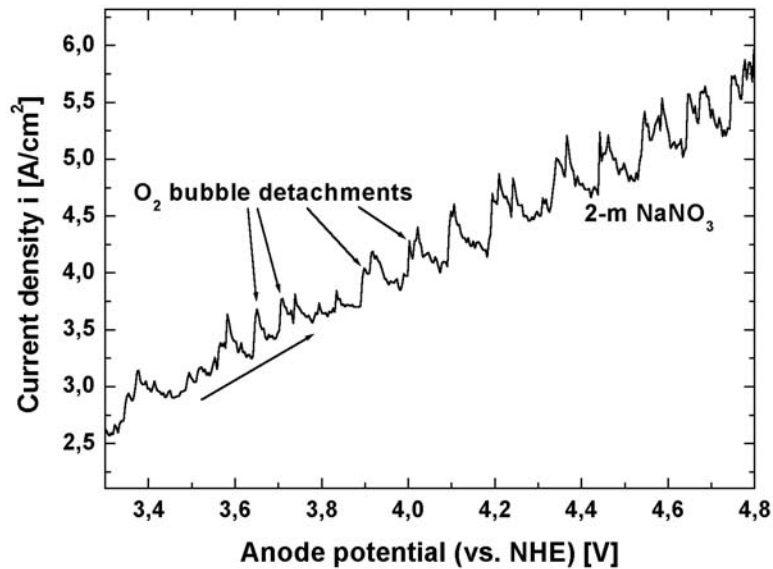


Fig. 6.7b: Enlarged part of the potentiodynamic polarization curve for a 2-m $NaNO_3$ solution (see Fig. 6.7a). At the point where large bubble collectives of oxygen leave the substrate surface a steep upward „jump“ in current density is observed.

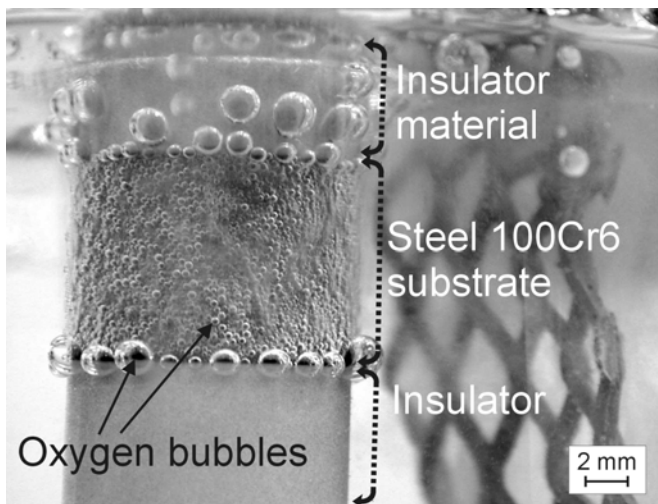


Fig. 6.8: Optical investigations of oxygen evolution on the 100Cr6 steel surface. The whole steel substrate surface is covered by a black, solid film; small gas bubbles ($\varnothing < 200$ μm) develop on this film. At the edge of the working electrode cylinder very big gas bubbles ($\varnothing < 1.8$ mm) are formed. Parameters for the potentiostatic experiment: $NaNO_3$ (40 wt.%), +2.5 V (vs. NHE), 25°C, 0 rpm.

Potentiostatic investigations, using the RCE without rotation, on the passive film development occurring at the substrate surface at potentials lower than the oxygen evolution potential (+1.8 V; see above) are presented in Fig. 6.9. The steel substrate was oxidized at four different anodic potentials (the length in time of the anodic period was chosen such that the current density had approximately reached the limiting current density of 23.6 mA/cm^2 ; see dotted line in Fig. 6.9). Since no iron dissolution or oxygen evolution occur in the potential range investigated, no electrode rotation was applied. After anodization, a fast switch to the cathodic potential of -0.5 V (vs. NHE) was carried out to demonstrate subsequently that then reduction of the passive film takes place (see stars in Fig. 6.9). The charges required for establishing complete film reduction were found to be 19 mC (at $+1.2 \text{ V}$), 23 mC ($+1.4 \text{ V}$), 37 mC ($+1.6 \text{ V}$) and 56 mC ($+1.8 \text{ V}$). Assuming that a compact Fe_2O_3 film with a density of 5.24 g/cm^3 [97] had developed on the substrate and that no charge had been carried by cathodic nitrate reduction, the thicknesses of the passive films, which had grown upon oxidation, were calculated from the values of transferred charges as 102 nm ($+1.2 \text{ V}$), 124 nm ($+1.4 \text{ V}$), 203 nm ($+1.6 \text{ V}$) and 309 nm ($+1.8 \text{ V}$). These thickness values are significantly higher than those reported for armco-iron substrates [54], which can be understood because the anodic charges transferred in the present experiments are many times larger.

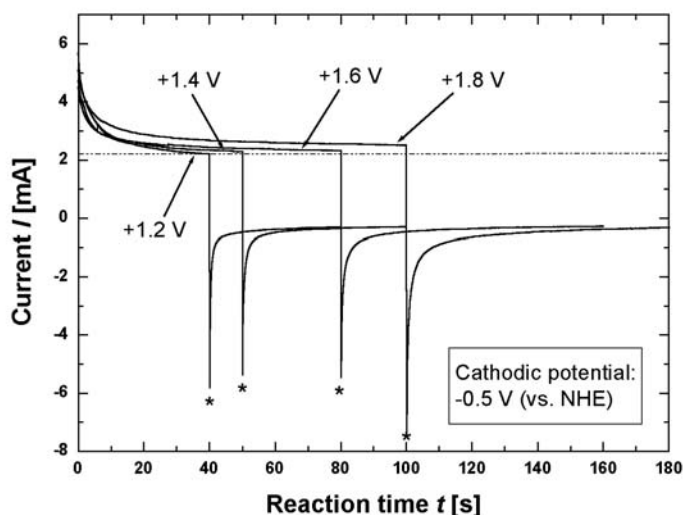


Fig. 6.9: Potentiostatic measurements of anodic passive film growth and cathodic film reduction (anode surface: 0.094 cm^2). The potentials for anodic polarization are given in the Figure, the cathodic reduction potential for all single measurements was -0.5 V (vs. NHE). The points of the

anodic / cathodic potential switches are indicated by stars in the Figure. Substrate: steel 100Cr6, electrolyte: NaNO_3 (40 wt.%), 25°C , no electrode rotation or electrolyte flow.

Investigations on the temperature dependence of the anodic polarization curves of the steel 100Cr6 in NaNO_3 (40 wt.%) show that the passivation region (0 to +1.8 V) exists at all temperatures investigated ($10^\circ - 70^\circ\text{C}$). No clear tendency for the temperature dependence of the anodic polarization curves could be found for the potential region above +1.8 V; the shapes of the curves are similar to those presented in Fig. 6.7a. The polarization curves are the outcome of competing iron dissolution and oxygen evolution. A possible variation in relative contributions of these reactions during the potentiodynamic measurement complicates the interpretation of the polarization curves. Mass loss measurements were carried out to demonstrate the temperature dependence of the integral current efficiency (calculated for a dissolution valence $n = 2$, see Fig. 6.10a).

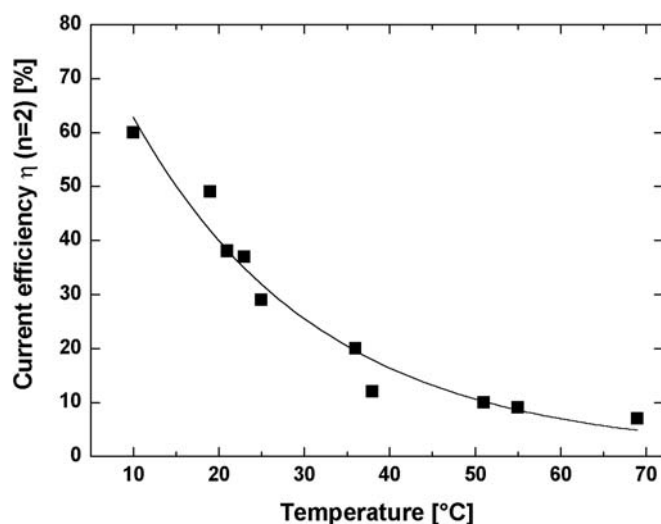


Fig. 6.10a: Temperature dependence of the integral current efficiency for divalent iron dissolution, obtained by potentiodynamic RCE-experiments (substrate: 100Cr6, electrolyte: NaNO_3 (40 wt.%), scan rate: 40 mV/s, rotation speed: 1136 rpm, potential scan range: +0.22 V to +4.22 V (vs. NHE), cycles: 1). With increasing electrolyte temperature oxygen evolution at the substrate surface is enhanced, leading to lower metal dissolution rates.

The result reveals, that with increasing electrolyte temperature, oxygen evolution at the substrate surface is significantly enhanced and iron dissolution is suppressed. This temperature effect in NaNO_3 electrolytes may be explained as follows. The partial current densities of iron dissolution, $i_{\text{Fe}^{2+}}$, and oxygen evolution, i_{O_2} , are shown schematically as function of the anode potential in Fig. 6.10b for two temperatures, T_1

and T_2 (for simplification the curves are assumed to be linear). The process of iron dissolution is not influenced significantly by a temperature increase because it has a relatively low activation energy [51]. On the other hand the temperature dependence of oxygen evolution is relatively large [51]. As a result, oxygen evolution dominates the ECM process at high temperature.

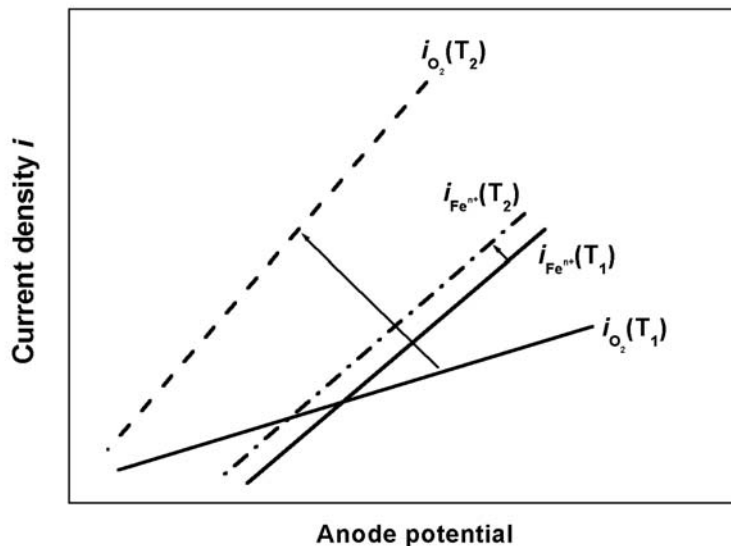


Fig. 6.10b: Schematic explanation for the dependence of the current efficiency on temperature in NaNO_3 electrolyte as presented in Fig. 6.10a. The partial current densities of iron dissolution, $i_{Fe^{n+}}$, and oxygen evolution, i_{O_2} , as function of the anode potential are presented at two temperatures, T_1 and T_2 ($T_2 > T_1$; for simplification the curves are assumed to be linear). Whereas iron dissolution is not significantly influenced by a temperature increase, the partial polarization curve of oxygen evolution shifts to much higher current density values. As a result, oxygen evolution dominates the ECM process at high temperatures.

The results presented in Figs. 6.7a, 6.8 and 6.10a and discussed above are consistent with polarization measurements at varying electrode-rotation speeds, which showed a very small dependence on the hydrodynamic conditions in the ECM system in the region of dominating oxygen evolution [72]: since ferrite dissolution is only a side reaction in NaNO_3 electrolytes at low anode potentials, the ECM process is not rate controlled by the Fe^{n+} -diffusion away from the electrode surface, and therefore no limiting current density, i_{lim} , depending on the electrode-rotation speed, occurs in the polarization curves (see Fig. 6.7a). The situation changes at high

current densities with increasing iron dissolution: an oversaturated honey-like film may be formed and the transport by diffusion and migration of Fe^{n+} will be dominant.

6.5 General discussion

6.5.1 A model description for ECM with NaNO_3 electrolytes

In general, solid surface films develop during the high rate electrochemical dissolution process of iron and steels when passivating electrolytes like NaNO_3 , Na_2SO_4 and Na_3PO_4 are applied for the ECM process [65, 72, 85, 87-89, 91-93]. For the case of steel substrates in passivating electrolytes, very heterogeneous and irregular anodic surface film structures develop, in dependence on the current density, the electrolyte composition, the temperature and the substrate microstructure [72]. For this reason, several different reaction mechanisms of surface film growth and breakdown have been proposed [31, 84]. It is usually suggested that the breakdown of the anodic film is caused by the penetration of anions into the developing film (dominantly composed of Fe_xO_y). Anions in the film at weak spots (e.g. at dislocations or at the interface with inclusions originating from the steel matrix) initiate film rupture. The number of incorporated anions will increase with increasing potential (current density) [31, 84].

If the ability of the anion to penetrate the protective surface film is not strong enough (as in the case of NaNO_3 electrolytes), the above picture is too simple. A possible model for the ECM process in NaNO_3 electrolytes is presented in Fig. 6.11. A soft annealed steel substrate containing globular carbides M_3C (black spots) within the ferrite matrix (α -iron, grey) is subjected to the high rate electrochemical metal dissolution (ECM) applying aqueous NaNO_3 electrolyte. Initially, a very thin iron-oxide layer develops on ferrite regions according to the reactions (6.1, 6.11-6.12). This initial FeO-film grows vertically and laterally [31]. The initial FeO-film is not stable at the high anode potentials applied in ECM [95, 96] and fast further oxidation according to reactions (6.4-6.5) occurs. Carbide particles in the steel matrix are inert and consequently are incorporated in the developing film. As a result, a highly heterogeneous film structure is formed by diverse oxide components and inert carbide particles. As both the solid oxidation products Fe_3O_4 , Fe_2O_3 (dark grey, see Fig. 6.11) and the insoluble carbides M_3C are electronically conductive (see section

6.4.2), oxygen evolution at the film / electrolyte interface (reaction (6.3)) occurs if the anode potential exceeds +1.8 V (see section 6.4.4; oxygen evolution is impossible at isolating components).

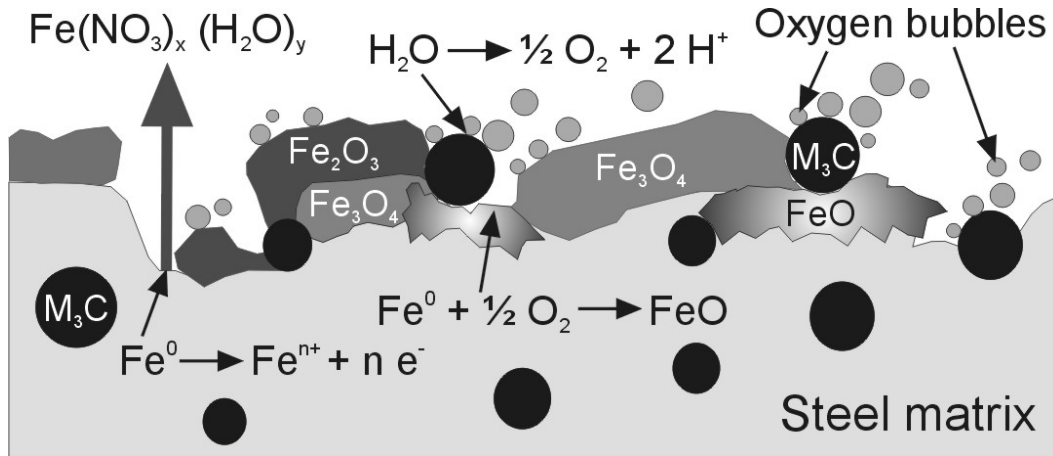


Fig. 6.11: Model description of the ECM process of the soft annealed steel 100Cr6 in $NaNO_3$ solution. The steel matrix contains globular carbides (M_3C , black) surrounded by ferrite (grey). Due to the passivating effect of nitrate, a thin iron oxide film (FeO) develops initially according to reactions (6.3) and (6.10) on the ferrite. This initial film is transformed by fast further oxidation to Fe_3O_4 and Fe_2O_3 . The inert, electron conducting carbides are enclosed in this solid oxide film. Since the diffusion of Fe^{n+} ions through solid components in the surface film is extremely slow, oxygen evolution at the film surface dominates. Upon rupture / detachment of the surface film, the thus activated bare metal areas can become repassivated by the reaction of oxygen gas, developing at the remaining part of the surface film, with the bare metal surface leading to the electroless formation of FeO according to reaction (6.10).

Since the diffusion of Fe^{n+} -ions through solid components is extremely slow, oxygen evolution increases with increasing substrate surface coverage (oxygen evolution occurs exclusively at the film surface, not at the bare metal surface). As direct consequences of oxygen evolution in particular within pores in the heterogeneous film structure, the mechanical stress within the surface film increases leading to local film rupture at the location of single pores. Progress of film rupture leads to areas where large scale film detachment has occurred: this then is a (metal dissolution) activating process. Copious oxygen bubble formation may allow a subsequent repassivation of the thus activated metal surface regions according to reaction (6.10).

Thus, the highly heterogeneous surface film structure observed as function of current density (anode potential) in the experiments presented in this paper, is the result of a dynamic process of activation and repassivation. If turbulent flow conditions are applied (typical for ECM), it is possible that, in addition to the metal removal by a diffusion / migration process, a considerable amount of metal removal is realized by mechanical erosion of solid components (such as iron oxides and carbides) from the anode surface (see discussion in Ref. [65]). Since the mechanical erosion process requires the presence of solid particles in the flowing liquid which „hammer” on the surface film [65], it can be suggested, that once the surface film gets locally damaged (see above), the mechanical erosion process becomes increasingly severe. Hence, the average thickness of the developing solid surface film is determined by the competing processes of electrochemical surface film growth (iron-oxide formation in combination with metal carbide inclusion) and electroless mechanical erosion of solid reaction products (Fe_xO_y , $\text{Fe}(\text{OH})_x$, $\text{FeO}(\text{OH})$) and inert metal carbides originating from the steel matrix.

6.5.2 Multilayer model; equivalent circuit

On the basis of the discussion in section 6.5.1 a highly simplified multilayer model for the steel / liquid interfacial region can be given (see Fig. 6.12):

a) *Solid part*: the steel substrate (M_3C carbides within an α -iron-matrix) is covered by a thin, solid FeO / M_3C film. The oxide layer adjacent to the liquid is constituted of Fe_3O_4 or Fe_2O_3 and M_3C (inert M_3C carbides enrich in this film).

b) *Gaseous / liquid part*: the layer, adjacent to the solid part, is a two-phase mixture of O_2 bubbles and an aqueous solution of ferrite dissolution products (it must be noted, that due to severe gas evolution at electronically conductive particles, local turbulences in the liquid develop and therefore the formation of a well defined diffusion layer is not expected).

Accordingly, an equivalent circuit (= electronic model circuit), composed of three single resistances in series, may be proposed to describe the current-potential characteristics of the ECM system. Hence, the polarization resistance, R_p , of the

complete NaNO_3 -ECM system can be given as (note that no bubble layer at the cathode influences the conductivity of the NaNO_3 electrolyte; see main reaction (6.6)):

$$R_p = R_{film} + R_{gas} + R_{electrolyte} \quad (6.14)$$

Values for the overall polarization resistance, R_p , and the resistance of the electrolyte, $R_{electrolyte}$, can be derived from the experimental data given in section 6.4.4 (note: resistance of electrolyte $\sim 1 / \text{conductivity of electrolyte}$).

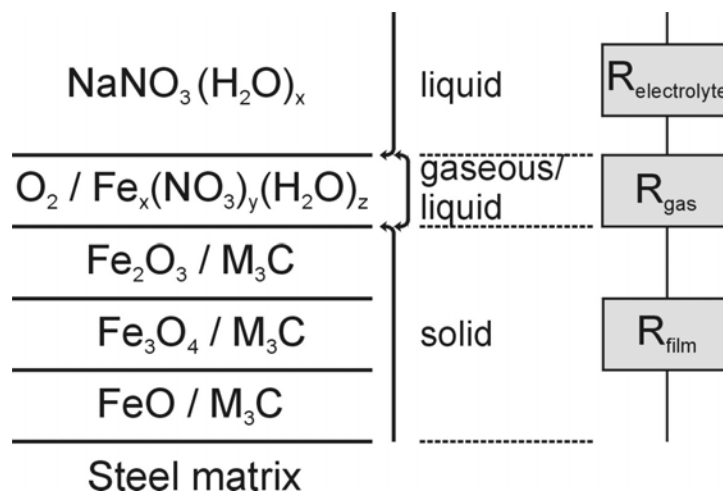


Fig. 6.12: Multilayer model as basis for an equivalent (= electronic model) circuit for ECM in NaNO_3 . The steel matrix is covered by a thin, solid $\text{FeO} / \text{M}_3\text{C}$ film. The outer oxide layers are composed of Fe_3O_4 and Fe_2O_3 (also including inert M_3C carbides). The layer adjacent to the solid part is a two-phase mixture of O_2 bubbles and an aqueous solution of iron dissolution products. The pure NaNO_3 electrolyte borders on the bubble layer. R_{film} is an effective resistance for the solid layer at the steel surface (containing FeO , Fe_3O_4 , Fe_2O_3 and M_3C), R_{gas} is the resistance of the two-phase O_2 -bubble layer and $R_{electrolyte}$ is the resistance of the NaNO_3 electrolyte.

For simplification, the overall resistance of the solid components at the substrate surface (Fe_xO_y and M_3C) are represented by one effective resistance, R_{film} , since it is impossible to incorporate the contributions of the single components separately due to the highly complex microstructure of the film (see Fig. 6.12). If a more detailed description of R_{film} is desired yet, it should be recognized that, in first order approximation, the resistances of the iron oxides can be taken in series (oxide

arrangement in the film is conceived to be in order of ion valence) and that the resistance of the metal carbide can be taken in parallel with the average resistance of the iron oxides. Thus:

$$\frac{1}{R_{film}} = \frac{1}{R_{FeO} + R_{Fe_3O_4} + R_{Fe_2O_3}} + \frac{1}{R_{M_3C}} \quad (6.15)$$

The resistance of the two-phase (gaseous / liquid) O₂-bubble layer, R_{gas} , depends on the number density and the average diameter of the O₂ gas bubbles and the conductivity of the liquid between the gas bubbles. Unfortunately, R_{gas} is unknown. Thereby a further analysis of R_{film} is abstracted.

6.5.3 Surface Coverage

The current density, i , as measured with the rotating cylinder electrode, is the sum of the contributions of all electrochemical reactions occurring simultaneously at the steel substrate. The main anodic reactions contributing to i are the divalent or trivalent iron dissolution at the active bare metal surface and O₂ evolution at the film particles surface (reactions (6.1-6.3); see section 6.3.1). The corresponding partial current densities are $i_{Fe^{2+}}$, $i_{Fe^{3+}}$ and i_{O_2} (where $i_{Fe^{2+}}$, $i_{Fe^{3+}}$ and i_{O_2} are calculated / defined with respect to the same total substrate / anode surface area as i):

$$i = i_{Fe^{2+}} + i_{Fe^{3+}} + i_{O_2} \quad (6.16)$$

An important parameter in this context is the (partial) coverage of the electrode with an electronically conductive surface film ($0 \leq \theta \leq 1$, with θ = fraction of surface covered). The diffusion and migration of Feⁿ⁺-species solvated at the substrate surface is only realizable through pores within the surface film in open contact with the aqueous electrolyte. Thus „pores” represent „active” ferrite areas. Oxygen evolution is located exclusively at electronically conductive surface film material (such as Fe₃O₄ or M₃C). Therefore, one can write:

$$i_{O_2} = i_{(O_2)} \theta \quad (6.17)$$

$$i_{Fe^{2+}} + i_{Fe^{3+}} = i_{(Fe^{n+})} (1-\theta) \quad (6.18)$$

Considering equations (6.17) and (6.18) a direct relation of the surface coverage, θ , with the current efficiency, η ($0 \leq \eta \leq 1$; calculated for divalent iron dissolution), is obvious:

$$\eta = k (1-\theta) \quad (6.19)$$

Here, the constant k represents the influence of the ferrite dissolution valence (for exclusive divalent ferrite dissolution: $k = 1$; exclusive trivalent: $k = 0.666$). The $i_{Fe^{2+}} / i_{Fe^{3+}}$ -ratio must be constant. With the experimental current efficiency data presented in section 6.4.1 in combination with equation (6.19), the calculation of the surface coverage, θ , becomes possible.

If the divalent iron dissolution prevails ($k = 1$), the following values for the surface coverage, θ , occur for the three zones presented in Fig. 6.2: in zone A with $\eta = 0$ (see section 6.4.1) a surface coverage $\theta = 1$ is expected. In the transition zone B the values are $1 > \theta > 0.3$ according to current efficiencies in the range $0 < \eta < 0.7$. For the zone C an approximately constant surface coverage $\theta \approx 0.3$ occurs.

6.6 Conclusions

1. Description of the electrochemical metal dissolution in $NaNO_3$ ECM-systems requires recognition of at least three competing anodic reactions, which may occur simultaneously: Fe^{2+} -, Fe^{3+} -formation and O_2 -evolution.
2. Complete passivation of the steel (100Cr6) substrate surface corresponding to the presence of a black surface film is established for anode potentials up to +1.8 V (vs. NHE).

3. At low current densities, above the threshold potential of +1.8 V (vs. NHE), exclusive oxygen evolution is observed (the electronically conductive black surface film still covers the entire substrate surface at this stage), which increases with increasing electrolyte temperature. Periodic overall current density fluctuations observed in the polarization measurements in this state of oxygen evolution indicate the formation-detachment-process of oxygen bubble groups at the anode surface.
4. With increasing current density (anode potential) and decreasing electrolyte temperature the formation of Fe^{n+} species (as determined by weight loss measurements) is enhanced, while oxygen evolution diminishes.
5. The electrochemical Fe^{n+} dissolution becomes the dominating ECM-reaction, if pronounced detachment of the surface film occurs and a direct ferrite / electrolyte interface is created. This situation prevails at high current densities ($i > 20 \text{ A/cm}^2$; $\theta \approx 0.3$).
6. The black, solid surface film which develops on a 100Cr6 substrate upon ECM (see conclusions 2 and 3) is constituted of amorphous Fe_xO_y components formed from dissolved iron and inert M_3C carbides, originating from the steel matrix, which have become embedded by the heterogeneous oxide matrix.
7. The ECM process of 100Cr6 steel in NaNO_3 can be conceived as an activation-repassivation-process. The initial, compact anodic surface film on the steel substrate gets locally ruptured at high current densities due to the development of oxygen gas in pores of the surface film. As a result bare metal (steel) substrate surface occurs: activation. This film rupturing is promoted by mechanical surface film erosion due to solid particles (iron-oxide and carbide particles) in the turbulent electrolyte flow „hammering” on the surface film. The copious oxygen evolution at remaining parts of the black surface film can cause oxidation of the, by film detachment established, bare metal areas: repassivation.

Chapter

7

***Kurzfassung der Dissertation in
deutscher Sprache***

7.1 Einleitung

Die elektrochemische Metallbearbeitung von Metallen, vor allem von Stählen, spielt eine wichtige Rolle in vielen industriell relevanten Mikrosystemtechnologien [20, 21, 24, 51-54]. Hierzu gehören beispielsweise das Elektropolieren zur Verbesserung des Glanzes von Metalloberflächen, des elektrochemische „Jet Machining“ zur gezielten Mikrostrukturierung mit Hilfe einer Elektrolyt-Düsenströmung, sowie das „Electrochemical Machining (ECM)“, bei dem mit Hilfe von extrem hohen Stromdichten eine gezielte anodische Metallauflösung herbeigeführt wird.

Die vorliegende Arbeit befasst sich vor diesem technologischen Hintergrund mit Untersuchungen zur anodischen Auflösung von technisch wichtigen Stählen (C-Gehalt: 0.15 bis 1 wt.%) bei hohen Stromdichten und hohen Strömungsgeschwindigkeiten in wässrigen NaCl- und NaNO₃-Elektrolyten (ECM-Prozess). Die prinzipielle Versuchsführung des Electrochemical Machining wurde mit Hilfe des Strömungskanals umgesetzt, mit dessen Hilfe die benötigten hohen Stromdichten und turbulenten Elektrolytströmungsgeschwindigkeiten erreicht werden können. Das elektrochemische Polarisationsverhalten der verwendeten Stahlsubstrate wurde mit der rotierenden Zylinderelektrode (RZE) untersucht, mit der eine besonders gute Kontrolle der hydrodynamischen Parameter durch die Einstellung der Umdrehungsgeschwindigkeit der Anode möglich ist.

Wenn passende Mikroelektroden zur Verfügung stehen, ermöglicht der ECM-Prozess die gezielte Mikrostrukturierung von reinen Metallen wie Eisen, Nickel, Chrom, Aluminium oder auch Titan [55]. Im Gegensatz zum mechanischen Polieren und zur Funkenerosion erlaubt die ECM-Technologie dabei eine Metallbearbeitung, die keinen mechanischen Schaden auf der Substratoberfläche verursacht. Bemerkenswert ist hierbei, dass die mechanische Härte des zu bearbeitenden Substrats keine Rolle im ECM-Prozess spielt. Aus diesem Grund wird das ECM-Verfahren häufig zur Produktion von Druckköpfen für Tintenstrahldrucker, zur Herstellung von Scherköpfen von Rasierapparaten, zur Produktion von Turbinen oder zur Formgebung von Bauteilen für die Automobilindustrie herangezogen [16, 51, 52].

Die Elektrolytauswahl beeinflusst das Ergebnis des elektrochemischen Abtrags sehr stark. Besonders intensiv sind deshalb wässrige Lösungen von NaCl [20, 24, 52-54, 56-65], NaNO₃ [16-19, 21, 36, 87-91] und NaClO₃ [17, 21, 36] in bezug auf ihren Einfluß auf die anodische Polarisation, die entstehende

Substratoberflächenmorphologie und die allgemeine Abtragungsgeschwindigkeit untersucht worden. Die meisten in der Literatur beschriebenen anodischen Auflösungsexperimente wurden mit reinen Metallsubstraten durchgeführt. Für die zugrundeliegenden Metall-Elektrolyt-Systeme sind plausible, quantitative Auflösungsmodelle vorgeschlagen worden, die hauptsächlich auf der Ausbildung von anodischen Deckschichten auf der Substratoberfläche und einem Massentransportkontrollierten Modell für den ECM-Prozess basieren [17, 20, 21, 28]. Im Gegensatz zu den umfassenden ECM-Studien zu reinen Metallen wurde die Untersuchung des anodischen Auflösungsverhaltens von technisch wichtigen Kohlenstoffstählen vergleichsweise vernachlässigt. Das elektrochemische Auflösungsverhalten von Kohlenstoffstählen ist komplexer, da aufgrund ihrer heterogenen Substrat-Mikrostruktur, die normalerweise auf einer Ferritmatrix und darin enthaltenen Metallcarbidgepartikeln, sowie nicht-metallischen Einschlussverbindungen (z. B. Oxide und Sulfide) basiert, neue Effekte das (sehr gut bekannte) Auflösungsverhalten des reinen Ferrits beeinflussen. Eine zufriedenstellende Modellbeschreibung für das anodische Auflösungsverhalten von Stählen unter Einbeziehung aller gefügespezifischen Effekte konnte aus diesem Grund bislang nicht gegeben werden.

7.2 Grundprinzip des Electrochemical Machining; Strömungskanal

Das Grundprinzip des elektrochemischen Metallabtrags (ECM-Prozesses) mit Hilfe eines Strömungskanals („parallel plate reactor“) ist in der Abb. 7.1 dargestellt. Zwei Elektroden (Kathode und Anode) werden parallel zu einander positioniert. Typische Abstände zwischen den Elektroden („working gaps“) bewegen sich in der Größenordnung von 0.1 bis 2 mm. Die Elektrolytlösung wird mit durchschnittlichen Strömungsgeschwindigkeiten von 1 bis 12 m/s durch den Strömungskanal gepumpt [51]. Die im elektrochemischen Metallauflösungsprozess auftretenden Elektrodenreaktionen (siehe Abb. 7.1) hängen im wesentlichen von der Elektrolytzusammensetzung, dem ausgewählten Anodenmaterial und der Stromdichte ab. Bei der ECM-Bearbeitung von Eisen und Stählen wurden die zweiwertige oder die dreiwertige Ferritauflösung und in speziellen Fällen die Sauerstoffentwicklung als anodische Hauptreaktionen beobachtet. Typische

kathodische Reaktionen sind die Wasserstoffentwicklung in NaCl-Systemen und die Nitratreduktion in NaNO₃-Systemen [24, 51].

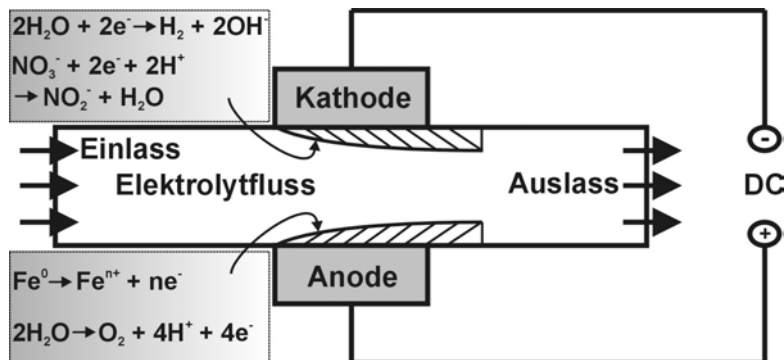


Abb. 7.1: Schematische Darstellung der anodischen Metallauflösung im Strömungskanal („parallel plate reactor“). Die elektrochemischen anodischen und kathodischen Hauptreaktionen sind auf der linken Seite dargestellt.

Für die in dieser Arbeit beschriebenen Versuche wurde (soweit nicht anders vermerkt) eine mittlere Elektrolytströmungsgeschwindigkeit von 7 m/s verwendet, welche auf Basis der berechneten Reynolds-Zahl von 25353 turbulenten Strömungsbedingungen entspricht [72]. Eine platiniierte Kupfer / Wolframlegierung wurde als Kathodenmaterial verwendet. Diverse Stähle dienten als Anoden (Zusammensetzung der Stähle: siehe Tabelle 7.1). Die Entfernung zwischen Kathode und Anode wurde auf 2 mm zu Beginn des Auflösungsversuchs eingestellt. Soweit nicht anders angegeben, wurden wässrige Lösungen von NaCl (20 wt.%) und NaNO₃ (40 wt.%) bei 40°C Elektrolyttemperatur verwendet. Alle Strömungskanalversuche wurden unter galvanostatischen Bedingungen mit Stromdichten bis zu 70 A/cm² durchgeführt.

Tabelle 7.1: Chemische Zusammensetzung der untersuchten Stahlsubstrate (in Gewichtsprozenten).

	C	Cr	Si	Mn	Ni	P	S	Fe
Armco-Eisen	~ 0	~ 0	~ 0	~ 0	~ 0	~ 0	~ 0	99.99
C15	0.15	~ 0	0.31	0.45	~ 0	0.044	0.045	99.15
C45	0.45	0.11	0.31	0.61	0.15	0.042	0.041	98.28
C60	0.60	0.37	0.39	0.72	0.23	0.039	0.038	98.21
100Cr6	0.97	1.43	0.28	0.28	0.11	0.006	0.002	96.91

7.3 Stromausbeute

Um den Gewichtsverlust der Substrate nach dem ECM-Versuch zu bestimmen, wurden zunächst die abwaschbaren Bestandteile der ausgebildeten schwarzen, festen Deckschicht mit destilliertem Wasser weggespült (soweit möglich) und dann die Proben im Stickstoffstrom getrocknet. Die Stromausbeute für den Auflösungsprozess des Stahls wurde dann auf der Berechnungsgrundlage der zweiwertigen Eisenauflösung mit Hilfe der Gravimetrie bestimmt. Die Metallcarbide und Einschlussverbindungen in der Stahlmatrix wurden als inert betrachtet, d.h. es wurde unterstellt, dass diese Komponenten sich nicht elektrochemisch auflösen. Der experimentell durch Gravimetrie bestimmte Massenverlust, ΔW_{ex} , kann mit Hilfe der folgenden Gleichung (7.1) mit dem theoretisch erwarteten Wert, ΔW_{theo} , verglichen werden [16, 17, 51, 72]:

$$\Delta W_{theo} = \frac{Mit}{nF} = \frac{MQ}{nF} \quad (7.1)$$

Hierbei ist M die Molmasse des sich auflösenden Metalls, I der während der Reaktionsdauer t geflossene Strom, F die Faraday-Konstante und n die Wertigkeit des Metalls (hier $n = 2$; siehe oben). Somit kann die Stromausbeute η wie folgt definiert werden:

$$\eta = \frac{\Delta W_{ex}}{\Delta W_{theo}} \quad (7.2)$$

Die in Strömungskanalversuchen bestimmte Stromausbeute für die anodische Auflösung des weichgeglühten Stahls 100Cr6 in NaCl- und NaNO₃-Elektrolyten wird als Funktion der Stromdichte in Abb. 7.2 dargestellt. Man kann erkennen, dass die Stromausbeute für die 100Cr6-Auflösung in NaCl-Lösung (20 wt.%) den Wert von 100% übersteigt. Es treten dabei Höchstwerte von bis zu 115% auf. Dies kann mit der stromlosen Erosion von inerten Partikeln von der Substratoberfläche (z. B. Metallcarbiden) erklärt werden, welche nicht elektrochemisch aufgelöst werden, jedoch aber zum gemessenen Massenverlust des Substrats beitragen [72]. Für den Fall des NaCl-Elektrolyten ist die Abhängigkeit der Stromausbeute von der

Stromdichte klein: sogar bei niedrigen Stromdichten von 1 A/cm^2 und darunter findet weitestgehend Metallauflösung mit einer hohen Stromausbeute von etwa 95% statt. Aus diesen Messwerten kann die zweiwertige Ferrit-Auflösung als anodische Hauptreaktion abgeleitet werden.

Die Stromausbeute für die anodische Auflösung des Stahls 100Cr6 in NaNO_3 -Lösung (40 wt.%) zeigt dagegen ein deutlich abweichendes Verhalten. Bis zu einer Stromdichte von 9 A/cm^2 findet man keinen (oder nur sehr geringen) Metallabtrag. Im Stromdichtebereich von 0 bis 9 A/cm^2 ist die Substratoberfläche völlig passiviert und anstatt der Ferritauflösung wird ausschließlich anodische Sauerstoffentwicklung an der festen Deckschicht auf dem Stahlsubstrat beobachtet. Diese Sauerstoffbildungsreaktion kann optisch in Form heftiger Gasentwicklung an der Anode nachgewiesen werden. In der Übergangszone zwischen 9 und 11 A/cm^2 wird ein steiler Anstieg der Stromausbeute bis zu einem Plateauniveau von ca. 71% beobachtet, was damit erklärt werden kann, dass in diesem Fall entweder die dreiwertige Ferritauflösung auftritt, oder dass ein simultaner Fe^{2+} -Auflösungs- und O_2 -Bildungsprozess vorherrscht. Hierbei ist zu beachten, dass die zweiwertige Metallionenbildung bei der Berechnung der Stromausbeute angenommen wurde. Bei hohen Stromdichten (im Plateaubereich) wird eine fast konstante Stromausbeute von 71% beobachtet.

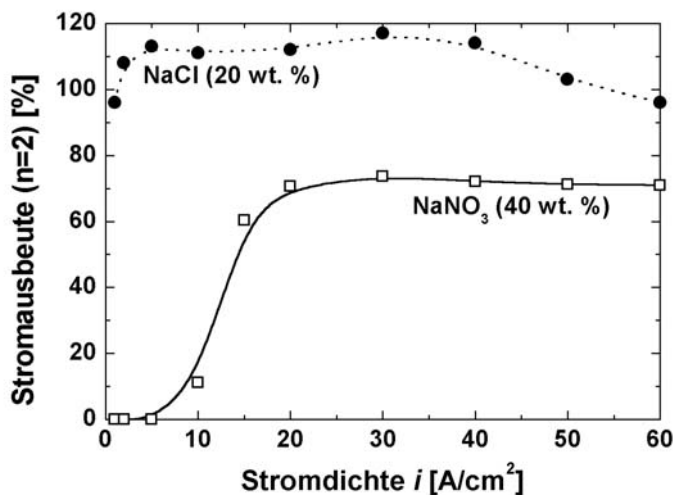


Abb. 7.2: Die in galvanostatischen Strömungskanal-Experimenten gemessene Stromausbeute als Funktion der Stromdichte für den weichgeglühten Stahl 100Cr6 in wässriger NaCl (20 wt.%) und wässriger NaNO_3 (40 wt.%). Experimentelle Parameter: 7 m/s; 40° C ; Elektrodenabstand: 2 mm.

7.4 Morphologie der Substratoberflächen

Die physikalischen Eigenschaften und die Zusammensetzung der Deckschichten, die sich während des ECM-Prozesses entwickeln, hängen vom Anodenmaterial, der Elektrolytzusammensetzung, den lokalen Strömungsfeldern an der Substratoberfläche und in speziellen Fällen von der Stromdichte ab [65, 72]. Auf der Oberfläche des Stahls 100Cr6 wurde nach dem ECM-Experiment regelmäßig eine schwarze, feste Deckschicht beobachtet, deren Haftung auf dem Substrat ganz wesentlich auf die Wahl der Anionen im Elektrolyten zurückzuführen ist. Diese Deckschicht besteht aus verschiedenen Eisenoxiden (Fe_xO_y) und inerten Metallcarbiden der Zusammensetzung M_3C ($\text{M} = \text{Fe}, \text{Cr}$) [65, 72]. Mit Hilfe von Röntgenbeugungs-Experimenten gelang es, die Carbide in der Deckschicht zweifelsfrei zu identifizieren, während die Eisenoxide offenbar amorph vorlagen. Im Falle des ECM-Prozesses mit NaCl-Lösungen ist die sich entwickelnde Deckschicht nur lose an das Stahlsubstrat gebunden und kann durch einen Waschvorgang mit Wasser vollständig entfernt werden. Im Gegensatz dazu ist bei Verwendung von NaNO_3 -Lösungen das Entfernen der Deckschicht weitestgehend unmöglich; sie ist sehr stark am Substrat verankert.

Eine typische Oberfläche des Stahls 100Cr6 mit einer sehr homogenen Verteilung von kugelförmigen Carbiden im weichgeglühten Gefüge nach der ECM-Bearbeitung mit NaCl (20 wt.%) ist in der rasterelektronenmikroskopischen Aufnahme in Abb. 7.3a dargestellt. Die Ferritmatrix des Stahls wurde offensichtlich während des ECM-Prozesses elektrochemisch aufgelöst, während die kugelförmigen Carbide M_3C sich völlig inert verhalten haben (kleine, weiße Kügelchen mit ca. 1 μm Durchmesser in der Abb. 7.3a). Es ist hierbei zu beachten, dass die feste schwarze Deckschicht auf dem 100Cr6-Substrat nach dem ECM-Experiment vollständig durch ein Waschverfahren mit destilliertem Wasser entfernt wurde (siehe oben).

Eine ungeeignete Wärmebehandlung des Stahls vor dem ECM-Experiment kann ausgeprägte Carbidsegregationen in „Zeilen“ innerhalb des 100Cr6-Substrats zur Folge haben [65]. In jenen Regionen, die an diese Carbidzeilen angrenzen, tritt in der Regel eine starke Verarmung an Carbiden innerhalb der Stahlmatrix auf, welche die elektrochemischen Eigenschaften lokal in die Richtung des reinen Eisens verschiebt. Bei der elektrochemischen Metallauflösung kann dies große Unregelmäßigkeiten (z. B. Muldenbildung) im Abtragsprofil der Probe verursachen,

wenn als Elektrolyt eine wässrige NaCl-Lösung verwendet wird (siehe Abb. 7.3b: die dargestellte Carbidgegationszeile ist senkrecht zur Substratoberfläche und zur Elektrolytströmungsrichtung orientiert). Das Ausmaß dieses Phänomens hängt vom Strömungsprofil an der Anodenoberfläche ab und kann mit einem Erosionskorrosionsmodell erklärt werden (siehe Kapitel 7.7) [47].

Die Oberfläche des Stahls 100Cr6, die nach elektrochemischer Auflösung in NaNO_3 -Elektrolyten beobachtet wird, ist durch die Ausbildung einer sehr heterogenen Deckschicht charakterisiert, welche in Abhängigkeit von der Stromdichte besonders stark an die Substratoberfläche gebunden ist (siehe Abb. 7.3c). Die in Abb. 7.3c erkennbare sehr poröse Deckschichtstruktur basiert auf einem „backbone“ aus amorphen Eisenoxiden (Fe_xO_y), welcher inerte, kugelförmige Carbide (M_3C) umschließt, die aus der Stahlmatrix stammen [72]. Eine lichtmikroskopische Aufnahme eines Querschliffs von dieser festen anodischen Deckschicht auf dem Stahlsubstrat ist in Abb. 7.4 dargestellt (die Deckschicht erscheint schwarz und die Stahlmatrix grau). Die lokale Dicke der dargestellten, heterogenen Deckschicht variiert beträchtlich (0-3 μm) und ein Bereich mit vollständiger Deckschichtablösung ist zu erkennen (sichtbar auf der rechten Seite in Abb. 7.4).

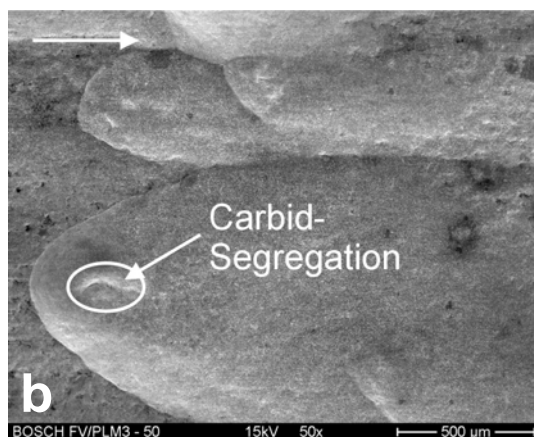
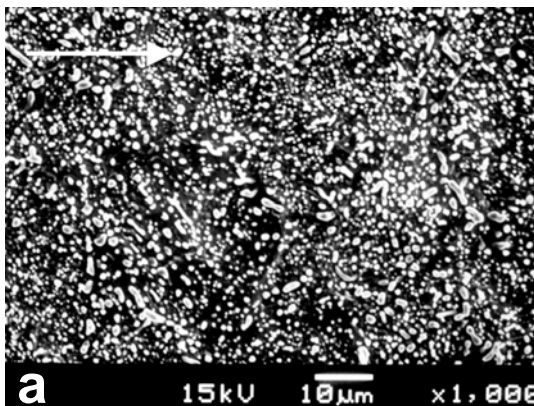


Abb. 7.3:

(a) Rasterelektronenmikroskopische Aufnahme der 100Cr6-Oberfläche nach dem ECM-Experiment (Strömungskanal-Versuch). Ein Stahlsubstrat mit sehr homogener Carbidgeverteilung in der Ferritmatrix wurde benutzt. Stromdichte: 20 A/cm^2 , 40 s, durchschnittliche Strömungsgeschwindigkeit: 7 m/s, wässrige NaCl (20 wt.%). Während des ECM-Prozesses löst sich die Ferritphase auf und die kugelförmigen M_3C Carbide (weiße Punkte) sind inert. Die Strömungsrichtung wird durch den Pfeil in der oberen linken Ecke angegeben.

(b) Rasterelektronenmikroskopische Aufnahme von einer 100Cr6-Substratoberfläche nach ECM. Das gewählte Stahlsubstrat ist durch eine stark inhomogene Metallcarbidgebietung in der Ferritmatrix (Segregationszeilen) charakterisiert. Stromdichte: 20 A/cm^2 , 40 s, mittlere Strömungsgeschwindigkeit: 7 m/s, NaCl (20 wt.%). Die Ausbildung einer Strömungsrinne auf der Substratoberfläche ist sichtbar. Die Carbidgebietungen ragen senkrecht zur Substratoberfläche und zur Strömungsrichtung aus den Zentren der Mulden heraus.

(c) Feste anodische Deckschicht auf einem 100Cr6-Substrat (Draufsicht). Stromdichte: 20 A/cm^2 , 40 s, mittlere Strömungsgeschwindigkeit: 7 m/s, NaNO_3 (20 wt.%). Einzelne kugelförmige Carbidgebietungen (ein Partikel ist mit einem weißen Kreis markiert) werden von einer sehr heterogenen Eisenoxid-Matrix eingebettet.

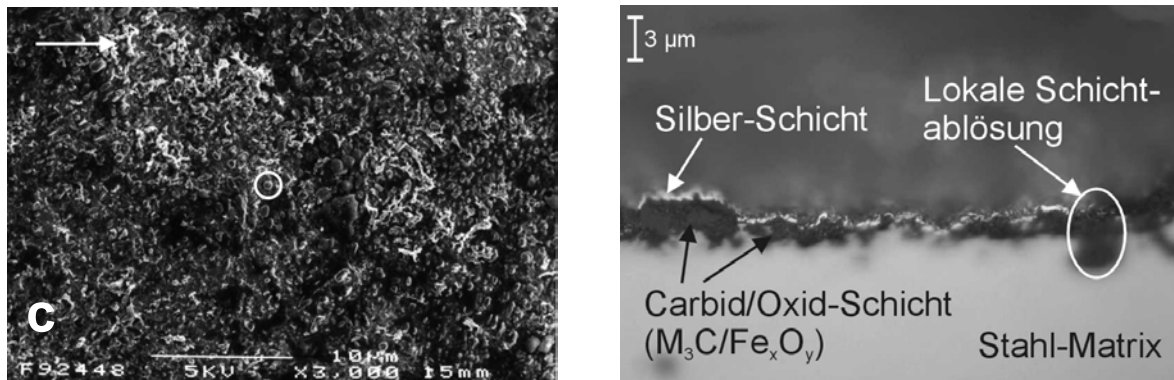


Abb. 7.4: Querschliff der festen Deckschicht (schwarz in der lichtmikroskopischen Aufnahme), die sich auf einem 100Cr6-Substrat während des ECM-Prozesses ausgebildet hat. Parameter: wässrige NaNO_3 (40 wt.%), 10 A/cm^2 , 60 s, 7 m/s, 40°C . Die Deckschicht wurde zur Verbesserung des Kontrasts mit einer 500 nm Silber-Schicht bedeckt. Die Dicke der heterogenen Deckschicht variiert sehr stark und lokale Schichtablösung wird beobachtet.

7.5 Potentiodynamische Stromdichte-Potentialkurven

Auf Basis der dargestellten Ergebnisse der Stromausbeutemessungen und den beobachteten Morphologien der Substratoberflächen nach dem ECM-Experiment ist es möglich die Abhängigkeit der Stromdichte vom Anodenpotential, welche mit Hilfe der rotierenden Zylinderelektrode (RZE) gemessen wurde, zu interpretieren. Die

Ergebnisse dieser Messungen (potentiodynamische Stromdichte-Potentialkurven) für NaCl-Elektrolyte und NaNO₃-Elektrolyte sind in Abb. 7.5 für verschiedene Umdrehungsgeschwindigkeiten der Anode dargestellt. Die Berechnung der jeweiligen Reynolds-Zahlen zeigte, dass in allen Fällen turbulente Strömungsbedingungen angenommen werden können.

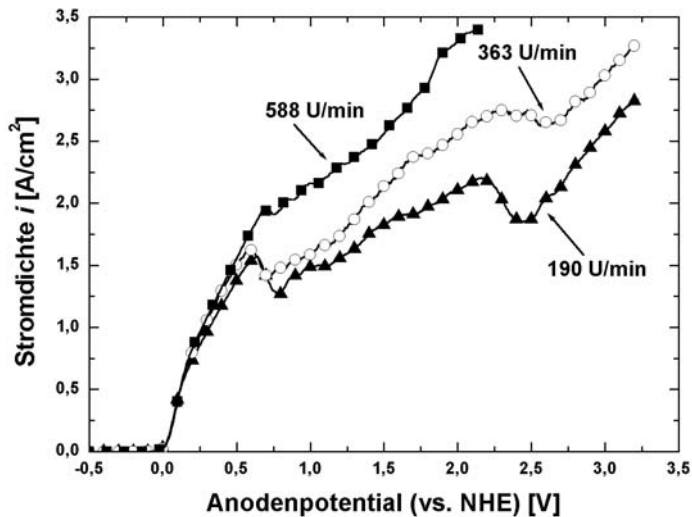


Abb. 7.5:

Anodische Polarisationskurven des weichgeglühten Stahls 100Cr6, die in potentiodynamischen Versuchen mit der rotierenden Zylinderelektrode (1.2 cm Durchmesser) bei verschiedenen Umdrehungsgeschwindigkeiten gemessen wurden. Die Polarisationskurven wurden mit einer 100Cr6-Arbeitslektrode (AE), einem Platinnetz als Gegenelektrode (GE) und einer kommerziell erworbenen Ag/AgCl/KCl Referenzelektrode (RE) ermittelt. Alle Potentiale beziehen sich auf die Normal-Wasserstoffelektrode (NHE). Abstand zwischen AE und GE: 1 cm; Scan rate: 40 mV/s; 25°C. **(a)** Elektrolyt: wässrige NaCl (20 wt.%).

Die aktive Metallauflösung in NaCl-Lösung beginnt bei -0.1 V (siehe Abb. 7.5a). Der Polarisationswiderstand $R_p = dU/di$ (mit U = Anodenpotential und i = Stromdichte) kann im allgemeinen als die Summe von R_{el} und R_{film} (R_{el} = Widerstand des Elektrolyten; R_{film} = Widerstand der festen Deckschicht, die sich auf dem Stahlsubstrat ausbildet) betrachtet werden. Bis zu einem Anodenpotential von +0.5 V hängt die Stromdichte i nicht von der Umdrehungsgeschwindigkeit ab. Der Wert von R_p ist vergleichsweise niedrig; er wird hauptsächlich durch den Ohm'schen Widerstand des Elektrolyten verursacht. In der Potentialregion von +0.6 bis +0.75 V

tritt bei niedrigen Umdrehungsgeschwindigkeiten ein signifikanter Abfall der Stromdichte i mit steigendem Anodenpotential auf, was sich mit der Ausbildung eines salzartigen Films auf dem Substrat erklären lässt, der zwar die Metallauflösung deutlich behindert, aber nicht den (deutlich größeren) Potentialabfall einer Passivschicht verursacht. Die Ausdehnung dieser Potentialregion kann durch Steigern der Elektrodenumdrehungsgeschwindigkeit minimiert werden (siehe die Kurve für 588 U/min in Abb. 7.5a), was mit der Ausdünnung des Anodenfilms aufgrund von stärkeren Turbulenzen im Elektrolyten erklärt werden kann. Die integrale Stromausbeute (berechnet für $n = 2$; siehe Kapitel 7.3) für den untersuchten anodischen Potentialbereich wurde zu 105 % bestimmt.

Aktive Metallauflösung bei niedrigen Stromdichten tritt bei Verwendung von NaNO_3 -Lösungen nicht auf (siehe Diskussion zur Abb. 7.2). In den potentiodynamischen Messungen, die in Abb. 7.5b dargestellt sind, wird bis zu +1.8 V kein (oder ein nur äußerst geringer) Stromfluss beobachtet. Statt dessen tritt die vollständige Passivierung der Substratoberfläche auf.

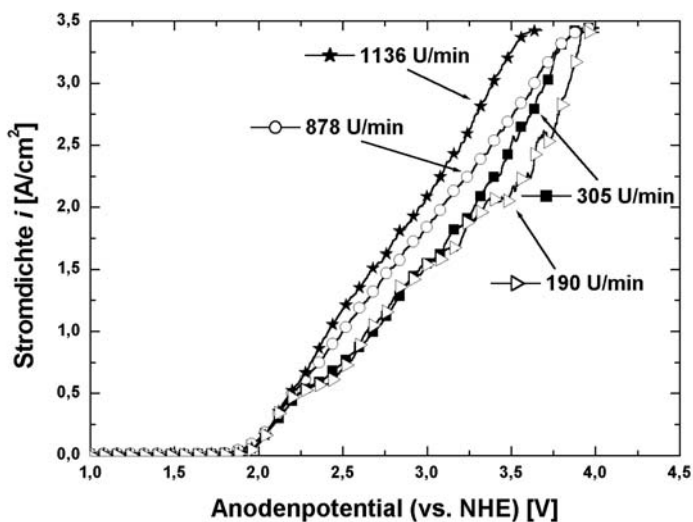


Abb. 7.5b: Elektrolyt: wässrige NaNO_3 (40 wt.%).

Der nahezu lineare Anstieg der Stromdichte-Potentialkurve für Anodenpotentiale über +1.8 V wird nicht durch einen Metallauflösungsprozess verursacht, sondern basiert auf der Entwicklung von Sauerstoff an der Oberfläche von elektronenleitenden Deckschichtpartikeln. Dies äußert sich auch in integralen Stromausbeuten, die deutlich kleiner als 5% sind (berechnet für $n = 2$). Eine Steigerung der Elektrodenumdrehungsgeschwindigkeit führt nicht zu nennenswert

höheren Stromdichten, was deutlich macht, dass die feste Deckschicht, welche sich auf dem Substrat ausgebildet hat, nicht mit einem höheren Grad der Turbulenzen im Elektrolyten ausgedünnt werden kann. In diesem Fall übersteigt der experimentell ermittelte Polarisationswiderstand, R_p , den der NaCl-Lösung, was einen beträchtlichen Beitrag des Filmwiderstands, R_{film} , zum gesamten Polarisationswiderstand aufzeigt.

7.6 Potentiostatische Stromtransientenmessungen

Potentiostatische Messungen mit der Zylinderelektrode ohne Rotation zur Untersuchung der Passivfilmentwicklung auf der Substratoberfläche bei Potentialen unterhalb des Sauerstoffbildungspotentials von +1.8 V (siehe Kapitel 7.5) sind in Abb. 7.6 dargestellt. Das 100Cr6-Stahlsubstrat wurde bei vier verschiedenen anodischen Potentialen oxidiert, wobei die Länge der anodischen Periode so ausgewählt wurde, dass die Stromdichte den experimentell beobachtbaren Grenzwert von 23.6 mA/cm^2 annähernd erreicht hatte (punktierte Linie in Abb. 7.6). Da bei den verwendeten Potentialen weder Eisenauflösung noch Sauerstoffentwicklung auftreten, wurde zur Vermeidung von Messartefakten eine ruhende Zylinderelektrode eingesetzt. Nach der anodischen Periode wurde umgehend auf ein kathodisches Potential von -0.5 V (vs. NHE) umgeschaltet, um die Reduktion des Passivfilms, der sich zuvor gebildet hatte, verfolgen zu können (der Umschaltzeitpunkt ist mit Sternen in der Abb. 7.6 dargestellt). Die Ladungsmengen, die dabei zur vollständigen Filmreduktion benötigt wurden, wurden mit 19 mC (bei +1.2 V), 23 mC (+1.4 V), 37 mC (+1.6 V) und 56 mC (+1.8 V) bestimmt. Unter der Annahme, dass auf dem Substrat ein kompakter Passivfilm der Zusammensetzung Fe_2O_3 mit einer Dichte von 5.24 g/cm^3 [54] ausgebildet wurde, und dass keine Ladung durch kathodische Nitratreduktion verbraucht wurde, können die Schichtdicken der Passivfilme, welche in der Oxidationsphase aufgebaut wurden, mit 102 nm (bei +1.2 V), 124 nm (+1.4 V), 203 nm (+1.6 V) und 309 nm (+1.8 V) bestimmt werden. Dass diese Schichtdickenwerte bedeutend größer sind als jene, die für Armco-Eisensubstrate gefunden wurden [54], kann damit erklärt werden, dass die in den hier beschriebenen Versuchen übertragenen anodischen Ladungsmengen deutlich größer sind.

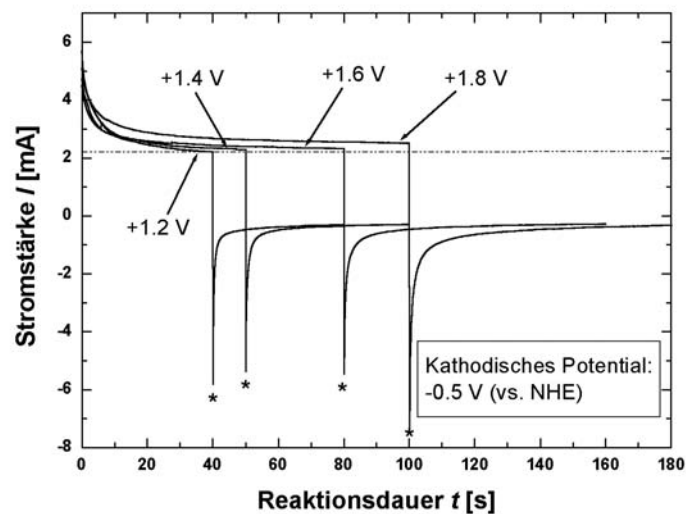


Abb. 7.6: Potentiostatische Messungen des anodischen Passivfilm-Wachstums und der kathodischen Film-Reduktion (Anodenoberfläche: 0.094 cm^2). Die Potentiale für die anodische Polarisation sind in der Abbildung angegeben, das kathodische Reduktionspotential für alle Einzel-Messungen betrug -0.5 V (vs. NHE). Die Umschaltunkte vom anodischen zum kathodischen Potential sind mit Sternen an den Stromtransienten angedeutet. Substrat: Stahl 100Cr6, Elektrolyt: NaNO_3 (40 wt.%), 25°C , keine Elektrodenrotation oder Elektrolytströmung.

7.7 Erosionskorrosionsmodell für den elektrochemischen Metallabtrag; Simulation

Zur schematischen Erklärung des in Abb. 7.3b dargestellten stark ungleichmäßigen Metallabtrags kann ein Erosionskorrosionsmechanismus für die anodische Metallauflösung von heterogenen Stahlsubstraten herangezogen werden [47, 65]. Bei diesem qualitativen Abtragsmodell wird davon ausgegangen, dass durch eine fehlerhafte Wärmebehandlung des Stahls Carbidgegregationszeilen in der Ferritmatrix des Stahls entstanden sind (siehe Abb. 7.7).

Zunächst bildet sich während des anodischen Metallabtrags eine feste Deckschicht auf der Stahloberfläche aus. Bei Verwendung von NaCl -Lösungen ist diese Deckschicht nur sehr lose am Substrat gebunden und die Deckschichtpartikel können durch das Strömungsprofil im Elektrolyten teilweise bewegt werden [65, 72]. Die Dicke und die chemische Zusammensetzung der Deckschicht können aufgrund

der gravierenden Heterogenität des Stahlsubstrats lokal sehr stark variieren. So wird beispielsweise in den Carbid-armen Regionen, welche an die Carbidsegregationszeile angrenzen (siehe Abb. 7.7), eine relativ hohe Metallauflösungsgeschwindigkeit beobachtet, die durchaus mit der des reinen Eisens vergleichbar ist. Im Gegensatz dazu sind die Abtragsraten in Bereichen mit vollständiger Deckschichtbedeckung deutlich geringer. Dementsprechend kann in Bereichen mit relativ dünner Deckschichtbedeckung ein lokaler Schichtdurchbruch auftreten und damit die Ausbildung von Mulden oder Strömungsriefen in der Substratoberfläche auftreten (siehe auch Abb. 7.3b). Die Ausbildung dieser Mulden in Verbindung mit der hohen Strömungsgeschwindigkeit des Elektrolyten kann zur Entwicklung von starken, lokalisierten Turbulenzen im Zentrum der Mulden führen. Carbidpartikel in der strömenden Flüssigkeit, die ursprünglich Teil der festen Deckschicht waren oder aus der Carbidsegregationszeile im Substrat stammen, können dann mechanisch auf die feste Deckschicht oder das blanke Stahlsubstrat „aufschlagen“: Erosionskorrosion.

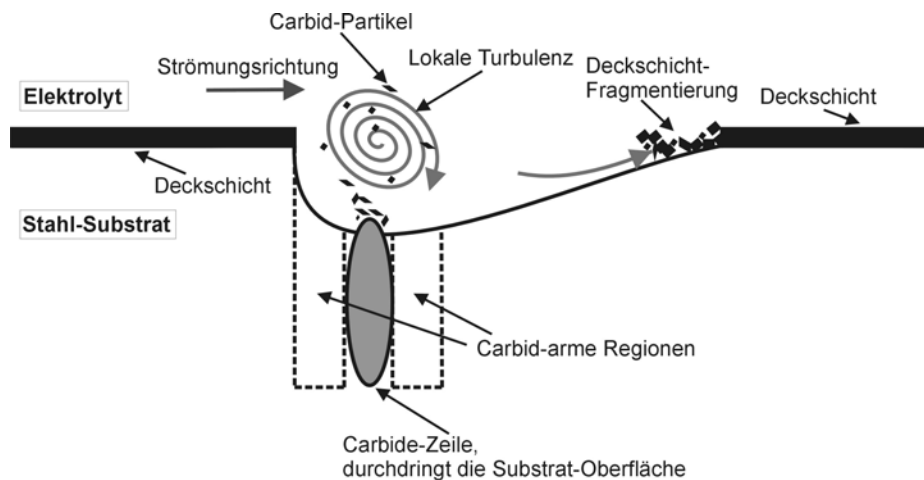


Abb. 7.7: Schematische Darstellung des lokalen Erosionskorrosionsmechanismus, der zur Ausbildung von Strömungsriefen in der Stahlsubstratoberfläche während der elektrochemischen Metallauflösung bei hohen Strömungsgeschwindigkeiten und hohen Stromdichten führt. Dieser Mechanismus tritt nur in konzentrierten NaCl-Elektrolyten auf.

Um das obengenannte Modell der Erosionskorrosion zu unterstützen, wurde eine 2D-Simulation der Strömungsgeschwindigkeitsverteilung des Elektrolyten innerhalb und in näheren Bereich der Mulde auf der Probenoberfläche durchgeführt. Ein

Standardturbulenzmodell wurde für diese Simulation übernommen, welche mit Hilfe des Programms Ansys Flotran (Version 5.6) durchgeführt wurde [48, 49]. Die physikalischen Eigenschaften der strömenden Flüssigkeit wurden als konstant angenommen: lokale Schwankungen der Dichte des Elektrolyten, der Viskosität oder der Temperatur wurden nicht zugelassen. Die Elektrolytströmungsgeschwindigkeit direkt an den Wänden des Strömungskanals wurde mit 0 m/s in die Simulation eingegeben. Die mittlere Strömungsgeschwindigkeit am Einlass des Strömungskanals wurde mit 7 m/s vorgegeben. Die Geometrie der Mulde wurde als kreisförmig mit 100 μm Kreisdurchmesser angenommen. Alle für die Berechnung verwendeten Parameter (Geometrie des Strömungskanals, mittlere Strömungsgeschwindigkeit, Viskosität und Dichte des Elektrolyten) wurden auf diejenigen Werte gesetzt, die auch in den Metallauflösungsexperimenten verwendet wurden. Das Ergebnis der 2D-Simulation ist in Abb. 7.8 dargestellt.

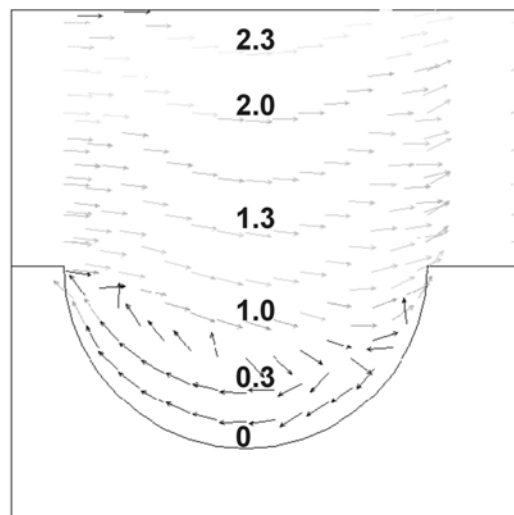


Abb. 7.8: Computersimulation des Strömungsprofils innerhalb und in der Nähe einer Mulde (2D-Simulation mit Ansys Flotran 5.6). Die lokalen Strömungsgeschwindigkeiten werden mit Pfeilen verdeutlicht. Die Zahlenwerte zeigen die absolute Strömungsgeschwindigkeit in m/s. Ein lokalisierter Wirbel kann im Zentrum der Mulde beobachtet werden. Die lokale Strömungsgeschwindigkeit innerhalb der Mulde ist deutlich kleiner als die Hauptströmungsgeschwindigkeit. Simulationsparameter: kinematische Viskosität der Flüssigkeit: $1.357 \times 10^{-6} \text{ m}^2/\text{s}$, Strömungsgeschwindigkeit am Kanaleinlass: 7 m/s, Strömungsgeschwindigkeit an den Wänden des Kanals: 0 m/s.

Gemäß dem Simulationsergebnis ist die lokale Strömungsgeschwindigkeit innerhalb der kreisförmigen Mulde deutlich geringer als in der Hauptströmung, welche im oberen Bereich der Abb. 7.8 zu erkennen ist. Als besonders charakteristisch sollte die Präsenz des permanenten Wirbels im Zentrum der Mulde angesehen werden. Es ist davon auszugehen, dass diese Art der Turbulenzbildung ein wesentlicher Bestandteil des Erosionskorrosionsmechanismus bei der anodischen Auflösung von Stählen ist (siehe auch Abb. 7.7).

7.8 Zusammenfassende Dimensionsbetrachtungen

Im Rahmen dieser Arbeit wurden einige wichtige Dimensionen für Erscheinungen ermittelt, die im direkten Zusammenhang mit den anodischen Prozessen auf der Substratoberfläche stehen. Diese sollen nun kurz zusammengefasst werden:

- Passivfilme* (in NaNO_3 -Lösung bei Potentialen unter $+1.8\text{V}$): Schichtdicken von 10 bis 400 nm.
- Schichtdicken der *viskosen Polierschicht* (in NaCl): 1 bis 10 μm
- Schichtdicken der festen schwarzen *Deckschicht* (in NaNO_3): 1 bis 4 μm
- Wirbeldurchmesser* in Mulden (Simulationsergebnis): 100 bis 300 μm
- Strömungsriefen* auf einem heterogenen Substrat: Bis zu 5 mm Länge und bis zu 300 μm Tiefe

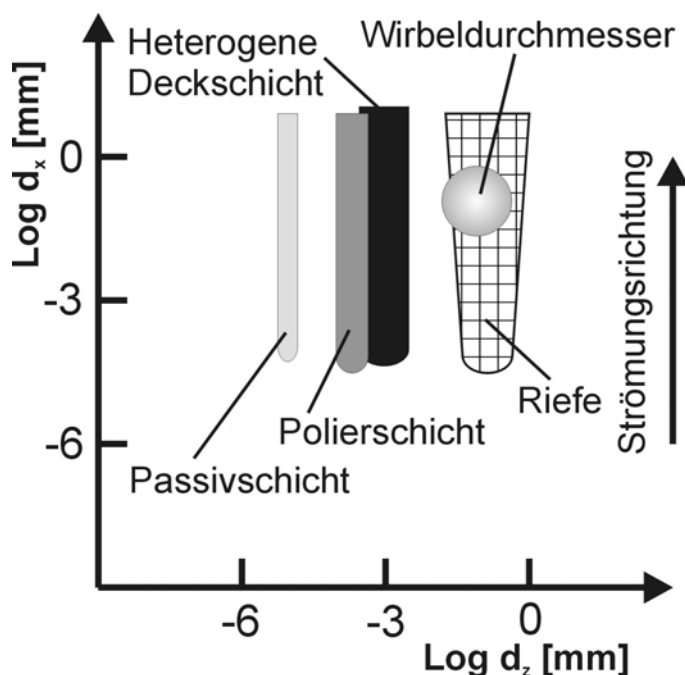


Abb. 7.9: Doppelt-logarithmische, zweidimensionale Darstellung von ECM-relevanten Längen. Die x-Richtung stellt die Strömungsrichtung dar, die z-Richtung steht senkrecht zur Substratoberfläche.

References

- [1] G. E. Miller, *J. Appl. Phys.*, **28** (1957) 149.
- [2] M. I. Ross, *Iron Age*, **193** (1964) 72.
- [3] T. W. Block, *Tool Manuf. Eng.*, **50** (1963) 87.
- [4] M. P. Fedotov, S. Y. Grilikhes, *Electropolishing, Anodizing and Electrolytic Pickling of Metals*, R. Draper Ltd., Teddington, England (1959).
- [5] O. Zmeskal, *Met. Prog.*, **47** (1945) 729.
- [6] C. Schaefer, *Met. Ind.*, **38** (1940) 22.
- [7] C. B. F. Young, W. L. Brytczuk, *Met. Finish.*, **40** (1942) 237.
- [8] H. Heinrich, H. G. Feller, *Metalloberfläche*, **38** (1984) 192.
- [9] H. Heinrich, H. G. Feller, *Metalloberfläche*, **38** (1984) 267.
- [10] A. Uhlir, *Rev. Sci. Instrum.*, **26** (1955) 965.
- [11] J. W. Tilley, R. A. Williams, *Proc. IRE*, **41** (1953) 1706.
- [12] M. H. Farmer, G. H. Glaysher, *J. Sci. Instrum.*, **30** (1953) 9.
- [13] T. E. Aaron, R. Wolosewicz, *Machine Design*, **41** (1960) 160.
- [14] S. P. Loutrel, N. H. Cook, *Trans. ASME*, **95B** (1973) 1003.
- [15] W. A. Haggerty, *SAE paper*, **680C** (1963).
- [16] M. Datta, *IBM J. Res. Develop.*, **37** (1993) 207.
- [17] M. Datta, *IBM J. Res. Develop.*, **42** (1998) 655.
- [18] K-W. Mao, *J. Electrochem. Soc.*, **118** (1971) 1870.
- [19] K-W. Mao, *J. Electrochem. Soc.*, **118** (1971) 1876.
- [20] M. Datta, D. Landolt, *Electrochim. Acta*, **25** (1980) 1255.
- [21] M. Datta, D. Landolt, *Electrochim. Acta*, **25** (1980) 1263.
- [22] M. S. Abdel-Aal, A. A. Hermas, *J. Appl. Electrochem.*, **30** (2000) 339.
- [23] W. Li, X. Wang, K. Nobe, *J. Electrochem. Soc.*, **137** (1990) 1184.
- [24] A. D. Davydov, V. D. Kaschtschejev, *Elektrokhimiya*, **9** (1974) 154.
- [25] J. P. Hoare, M. A. LaBoda, M. L. McMillan, A. J. Wallace, *J. Electrochem. Soc.*, **116** (1969) 199.
- [26] J. P. Hoare, *Nature*, **219** (1968) 1034.
- [27] E. Rosset, M. Datta, D. Landolt, *J. Appl. Electrochem.*, **20** (1990) 69.
- [28] M. Datta, D. Landolt, *J. electrochem. Soc.*, **122** (1975) 1466.
- [29] M. Datta, B. Giovanola, J. Kolub, *Prakt. Met.*, **20** (1983) 394.

- [30] J. P. Hoare, A. J. Chartrand, M. A. LaBoda, *J. Electrochem. Soc.*, **120** (1973) 1071.
- [31] T. P. Hoar, *Corros. Sci.*, **7** (1967) 341.
- [32] D-T. Chin, K-W. Mao, *J. Appl. Electrochem.*, **4** (1974) 155.
- [33] N. Sato, K. Kudo, *Electrochim. Acta*, **19** (1974) 461.
- [34] J. F. Thorpe, R. D. Zerkle, *Int. J. Mach. Tool Des. Res.*, **9** (1969) 131.
- [35] L. Bass, *Trans. Faraday Soc.*, **60** (1964) 1646.
- [36] D-T. Chin, A. J. Wallace, *J. Electrochem. Soc.*, **120** (1973) 1487.
- [37] M. Datta, L. F. Vega, L. T. Romankiw, P. Duby, *Electrochim. Acta*, **37** (1992) 2469.
- [38] K. Chikamori, S. Ito, *Denki Kagaku*, **39** (1971) 493.
- [39] M. Datta, *Interface*, **4** (1995) 32.
- [40] M. Datta, D. E. King, A. D. Knight, C. J. Sambucetti, *U.S. Patent 5.105.537*, (1992).
- [41] H. Schlichting, *Boundary-layer theory*, 7th Edition, McGraw-Hill Book Company, New York (1979).
- [42] M. Datta, D. Landolt, *J. Electrochem. Soc.*, **129** (1982) 1889.
- [43] W. Peter, H. Finkler, E. Kohlhaas, *Arch. Eisenhüttenwes.*, **41** (1970) 749.
- [44] H. Schumann, *Metallographie*, VEB-Verlag, Leipzig (1980).
- [45] J. L. Pouchou, F. Pichoir, *La Recherche Aérospatiale*, (1984) 3.
- [46] K. Bungardt, E. Kunze, E. Horn, *Arch. Eisenhüttenwes.*, **29** (1958) 193.
- [47] C. Loss, E. Heitz, *Werkst. u. Korrosion*, **24** (1973) 38.
- [48] B. E. Launder, D. B. Spalding, *Computer Methods in Appl. Mechan. Eng.*, **3** (1974) 269.
- [49] Ansys Theory Reference, *Manual for Simulation Program Ansys*, Ninth Edition, SAS IP, Canonsburg (1999) 7.
- [50] L. Kops, V. B. Quach, *J. Eng. Ind.*, **98** (1976) 360.
- [51] J. A. McGeough, *Principles of Electrochemical Machining*, Chapman and Hall (1974).
- [52] M. Datta, D. Harris, *Electrochim. Acta*, **42** (1997) 3007.
- [53] M. Datta, D. Landolt, *Electrochim. Acta*, **45** (2000) 2535.
- [54] M. Datta, H. J. Mathieu, D. Landolt, *J. electrochem. Soc.*, **131** (1984) 2484.
- [55] J. W. Schultze, V. Tsakova, *Electrochim. Acta*, **44** (1999) 3605.
- [56] D-T. Chin, *J. electrochem. Soc.*, **119** (1972) 1043.

- [57] M. Datta, H. J. Mathieu, D. Landolt, *Electrochim. Acta*, **24** (1979) 843.
- [58] A. D. Davydov, *Protection of Metals*, **35** (1999) 102.
- [59] M. A. LaBoda, A. J. Chartrand, J. P. Hoare, C. R. Wiese, Kao-Wen Mao, *J. electrochem. Soc.*, **120** (1973) 643.
- [60] D. Landolt, *Electrochim. Acta*, **32** (1987) 1.
- [61] J. K. Higgins, *J. electrochem. Soc.*, **106** (1959) 999.
- [62] Y. A. Popov, S. N. Sidorenko, A. D. Davydov, *Elektrokhimiya*, **33** (1997) 557.
- [63] D. R. Gabe, *J. Appl. Electrochem.*, **4** (1974) 91.
- [64] E. Rosset, M. Datta, D. Landolt, *Plat. & Surf. Fin.*, **71** (1985) 60.
- [65] T. Haisch, E. J. Mittemeijer, J. W. Schultze, *Z. Metallkd.*, **92** (2001) 417.
- [66] J. E. Bannard, J. R. Duncan, G. Lewis, *J. Appl. Electrochem.*, **11** (1981) 253.
- [67] M. Datta, L. T. Romankiw, *J. electrochem. Soc.*, **145** (1998) 3052.
- [68] M. S. Amalnik, J. A. McGeough, *J. Mat. Proc. Tech.*, **61** (1996) 130.
- [69] M. Datta, L. T. Romankiw, D. R. Vigliotti, R. J. von Gutfeld, *J. electrochem. Soc.*, **136** (1989) 2251.
- [70] J. A. McGeough, M. B. Barker, *Chemtech*, **9** (1991) 536.
- [71] P. A. Brook, Q. Iqbal, *J. electrochem. Soc.*, **116** (1969) 1458.
- [72] T. Haisch, E. J. Mittemeijer, J. W. Schultze, *Electrochim. Acta*, **47** (2001) 235.
- [73] M. Prazak, V. Prazak, V. L. Cihal, *Z. Elektrochem.*, **62** (1958) 739.
- [74] J. W. Schultze, A. Bressel, *Electrochim. Acta*, **47** (2001) 3.
- [75] M. M. Lohrengel, *Electrochim. Acta*, **42** (1997) 3265.
- [76] D. R. Gabe, G. D. Wilcox, *J. Appl. Electrochem.*, **28** (1998) 759.
- [77] W. Vielstich, *Z. Elektrochem.*, **57** (1953) 646.
- [78] H. C. Kuo, D. Landolt, *Electrochim. Acta*, **20** (1975) 393.
- [79] J. W. Schultze, M. M. Lohrengel, *Electrochim. Acta*, **45** (2000) 2499.
- [80] R. N. Adams, *Electrochemistry at solid electrodes*, Dekker (1969).
- [81] G. A. Prentice, C. W. Tobias, *J. electrochem. Soc.*, **129** (1982) 78.
- [82] D. Landolt, R. H. Muller, C. W. Tobias, *J. electrochem. Soc.*, **116** (1969) 1384.
- [83] P. J. Boden, J. M. Evans, *Electrochim. Acta*, **16** (1971) 1071.
- [84] A. D. Davydov, *Elektrokhimiya*, **14** (1978) 979.
- [85] A. D. Davydov, E. Y. Grodzinski, A. N. Kamkin, *Elektrokhimiya*, **9** (1973) 518.
- [86] A. D. Davydov, A. D. Romashkan, M. A. Monina, V. D. Kaschtschejev, *Elektrokhimiya*, **10** (1974) 1681.
- [87] M. Nagayama, M. Cohen, *J. electrochem. Soc.*, **109** (1962) 781.

- [88] M. Nagayama, M. Cohen, *J. electrochem. Soc.*, **110** (1963) 670.
- [89] K-W. Mao, *J. electrochem. Soc.*, **120** (1973) 1056.
- [90] J. P. Hoare, C. R. Wiese, *Corros. Sci.*, **15** (1975) 435.
- [91] K-W. Mao, M. A. LaBoda, J. P. Hoare, *J. electrochem. Soc.*, **119** (1972) 419.
- [92] M. Datta, D. Landolt, *J. electrochem. Soc.*, **124** (1977) 483.
- [93] M. Datta, D. Landolt, *J. Appl. Electrochem.*, **7** (1977) 247.
- [94] L. Franke, W. Forker, *Electrochim. Acta*, **19** (1974) 27.
- [95] M. Pourbaix, *Atlas of Electrochemical Equilibria*, 1st English Edn., Pergamon Press (1966).
- [96] B. Beverskog, I. Puigdomenech, *Corros. Sci.*, **38** (1996) 2121.
- [97] R. C. Weast, M. J. Astle, *Handbook of Chemistry and Physics*, 60th Edn., CRC Press, Inc. (1979-1980).

Curriculum Vitae

Thomas Wagner (geb. Haisch)

born on 1st November 1971 in Waiblingen

School

1978-1982 primary school, Waiblingen

1982-1991 secondary school, Staufer-Gymnasium Waiblingen, high school graduation („Abitur“)

Higher education

10/92-08/98 University of Stuttgart, Chemistry

08/98-01/99 University of Stuttgart, Institut für Physikalische Chemie
Diploma thesis: *„Festkörper-NMR-Untersuchungen zur Dynamik von n-Alkanen in Cyclophosphazen-Einschlussverbindungen“*

Since 04/99 PhD at Max Planck Institute for Metals Research, Stuttgart
PhD thesis: *„High rate electrochemical dissolution of iron-based alloys in NaCl and NaNO₃ electrolytes“*

Danksagung

Die vorliegende Arbeit wurde bei der Robert-Bosch-GmbH, Schwieberdingen, mit der Betreuung des Instituts für Metallkunde der Universität Stuttgart und des Instituts für Physikalische Chemie und Elektrochemie der Universität Düsseldorf durchgeführt.

Mein besonderer Dank gilt der Robert-Bosch-GmbH für die Finanzierung dieser Arbeit, Herrn Prof. Dr. Ir. E.J. Mittemeijer und Herrn Prof. Dr. J.W. Schultze für die inhaltliche Betreuung des weitreichenden Themas, das große Interesse am Fortgang der Arbeit und den zahlreichen wissenschaftlichen Diskussionen. Darüber hinaus danke ich Herrn Dr. Hackenberg für die teilweise recht zeitintensive Mitwirkung an meiner Arbeit.

Den Mitarbeitern des Max-Planck-Institutes für Metallforschung danke ich für die ergiebige Zusammenarbeit im Bereich der Oberflächenanalytik. Besonders danken möchte ich hierbei Herrn Gödecke für seine sehr hilfreiche, besonders detaillierte Einführung in die Metallographie.

Den Mitarbeitern des Instituts für Elektrochemie der Universität Düsseldorf danke ich für die wichtige experimentelle Unterstützung im Bereich der Elektrochemie. Dies gilt im besonderen für Andreas Möhring, Milan Pilaski, Tobias Hamelmann und Manuel Lohrengel.

Für die lustige Atmosphäre am Arbeitsplatz bedanke ich mich besonders bei allen Bosch-Doktoranden.

Widmung

Ich widme diese Arbeit meiner Mutter, die den Beginn dieser Promotion leider nicht mehr miterleben konnte.